ULTRAFAST EXCITATION ENERGY TRANSFER DYNAMICS IN PHOTOSYNTHETIC PIGMENT–PROTEIN COMPLEXES

Thomas RENGER[a], **Volkhard MAY**[b], **Oliver KÜHN**[c]

[a]*A.A. Noyes Laboratory of Chemical Physics, California Institute of Technology,*
127-72 Caltech, Pasadena, CA 91125, USA
[b]*Institut für Physik, Humboldt-Universität zu Berlin, Hausvogteiplatz 5–7,*
D-10117 Berlin, Germany
[c]*Institut für Chemie, Physikalische und Theoretische Chemie, Freie Universität Berlin,*
Takustrasse 3, D-14195 Berlin, Germany

N·H
ELSEVIER

AMSTERDAM – LONDON – NEW YORK – OXFORD – PARIS – SHANNON – TOKYO

ELSEVIER

Physics Reports 343 (2001) 137–254

PHYSICS REPORTS

www.elsevier.com/locate/physrep

Ultrafast excitation energy transfer dynamics in photosynthetic pigment–protein complexes

Thomas Renger[a], Volkhard May[b,*], Oliver Kühn[c]

[a] *A.A. Noyes Laboratory of Chemical Physics, California Institute of Technology, 127-72 Caltech, Pasadena, CA 91125, USA*
[b] *Institut für Physik, Humboldt-Universität zu Berlin, Hausvogteiplatz 5-7, D-10117 Berlin, Germany*
[c] *Institut für Chemie, Physikalische und Theoretische Chemie, Freie Universität Berlin, Takustrasse 3, D-14195 Berlin, Germany*

Received May 2000; editor: S.D. Peyerimhoff

Contents

---

* Corresponding author. Tel.: 030-203-77-406; fax: 030-238-47-63.
E-mail address: may@physik.hv-berlin.de, may@semic.ag-berlin.mpg.de (V. May).

PII: S0370-1573(00)00078-8

Abstract

Photosynthetically active membranes of certain bacteria and higher plants contain antenna systems which surround the reaction center to increase its absorption cross section for the incoming sun light. The excitation energy created in the antenna pigments is transferred via an exciton mechanism to the reaction center where charge separation takes place. Sub-picosecond laser spectroscopy makes it possible to follow the initial dynamic events of excitation energy (exciton) motion and exciton relaxation in real time. On the other hand, the success of structure resolution opened the door to the microscopic understanding of spectroscopic data and to an appreciation of the structure–function relationship realized in different systems. Here, it will be demonstrated how the combination of microscopically based theoretical models and numerical simulations pave the road from spectroscopic data to a deeper understanding of the functionality of photosynthetic antenna systems. The density matrix technique is introduced as the theoretical tool providing a unified description of the processes which follow ultrafast laser excitation. This includes in particular coherent exciton motion, vibrational coherences, exciton relaxation, and exciton localization. It can be considered as a major result of recent investigations that a theoretical model of intermediate complexity was shown to be suitable to explain a variety of experiments on different photosynthetic antenna systems. We start with introducing the structural components of antenna systems and discuss their general function. In the second part the formulation of the appropriate theoretical model as well as the simulation of optical spectra is reviewed in detail. Emphasis is put on the mapping of the complex protein structure and its hierarchy of dynamic phenomena onto models of static and dynamic disorder. In particular, it is shown that the protein spectral density plays a key role in characterizing excitation energy dissipation. The theoretical concepts are illustrated in the third part by results of numerical simulations of linear and nonlinear optical experiments for three types of antennae: the peripheral light-harvesting complex 2 of purple bacteria, the Fenna–Mathew–Olson complex of green bacteria, and the light-harvesting complex of photosystem II of green plants.

PACS: 87.15. − v; 71.35.Aa; 78.47. + p

Keywords: Dissipative Frenkel-exciton dynamics; Photosynthetic antenna systems; Density matrix theory; Ultrafast spectroscopy

1. Introduction

The storage of solar energy in energetically rich organic compounds and the accompanying evolution of oxygen represents the basis of life on earth. It is a challenging and exciting task to understand the molecular details of this process called *photosynthesis*.

Due to the progress in experimental techniques and computer power it became possible to develop a microscopic picture of the primary photosynthetic processes. Biochemical methods enable one to separate parts of the photosynthetic apparatus of photosynthetic bacteria and green plants and perform site-directed mutations. X-ray and electron diffraction studies allow to visualize the microscopic structures. Biophysical measurements applying laser spectroscopy in the frequency and time domain probe the microscopic dynamics. Finally, quantum mechanical calculations allow for a detailed interpretation of the experiments, and conclusions can be drawn on structure–function relationships.

The photochemistry of photosynthesis starts with a primary charge separation in the photosynthetic reaction center. For example, in the reaction center of photosynthetic bacteria a bacteriochlorophyll dimer (the so-called *special pair*) acts as the primary electron donor. Within 2 ps an electron is transferred from the excited special pair to a bacteriopheophytin, and from there in about 100 ps to a menaquinone. Finally, the hole at the oxidized special pair is filled by an electron from a reduced cytochrome (with a time constant of about 10 ns), leaving the special pair in its ground state. In this way the excitation energy of the special pair is used to transfer an electron through the photosynthetic membrane. The resulting transmembrane potential drives biochemical reactions leading finally to the evolution of oxygen and the fixation of carbon.

The initial excitation can be created due to the absorption of sun light by the special pair. However, at much higher probability excitation energy is supplied by light-harvesting antennae, which surround the reaction center to enlarge the cross section for the capture of sun light. The antenna system contains a number (≈ 200) of photoactive *pigment* molecules, which absorb the sun light and efficiently transfer the excitation energy to the reaction center. More than 98% of light-induced excitations (excitons) reach the reaction center to trigger the electron transfer [1]. The active pigments are different forms of chlorophyll (Chl), bacteriochlorophyll (BChl), as well as carotenoid molecules. Chlorophyll and bacteriochlorophyll molecules can be classified as modified tetrapyrols. Due to structural differences the various chlorophyll species absorb at different energies and thus the absorption cross section of the reaction center will be increased not only spatially but also spectrally.

The understanding of the details of light-harvesting requires the knowledge of the microscopic structure of antenna complexes. The first pigment–protein complex (PPC) that could structurally be resolved by X-ray crystallography was the so-called *Fenna–Matthews–Olson* (FMO) complex. It is a water soluble bacteriochlorophyll*a* protein complex from green sulphur bacteria [2]. Recently, the light-harvesting complex of photosystem II of green plants (LHC-II) [3] and the peripheral light-harvesting antenna of purple bacteria (LH2) [4] followed. The positions of the pigments are known with a resolution down to 1.8 Å, for the FMO complex. The natural environment of the pigments in these systems is given by proteins. They provide the scaffold that holds the pigments supposingly in optimal positions for exciton transfer to the photosynthetic reaction center.

There are some specific features which distinguish PPCs from other nonbiological chromophore complexes and dye aggregates. First, PPCs are characterized by a well-defined structure, i.e. the spatial arrangement of the chromophores (embedding of the Chl in the protein matrix). Structural fluctuations in a sample among different PPCs of the same type, i.e. *static disorder* is only of intermediate strength. Nonbiological system may show a much larger spatial inhomogeneity. Using site-directed mutagenesis a particular tool is available to introduce a local change in the structure of the PPC. Such precise alternation of the chromophore arrangement is impossible in most cases of nonbiological systems. Finally, one has to take notice of the outstanding aspect which is responsible for the PPC structure. This is the evolution of life which indeed optimized these molecular nanostructure in a particular way such that they can fulfill their biological function.

The knowledge of the microscopic structure of some of these photosynthetic PPC stimulated many experiments. Using femtosecond laser pulses, the excitation transfer can be visualized, for example, by means of ultrafast pump–probe spectroscopy. However, in order to extract from the experimental data the underlying microscopic dynamics, and in particular to uncover the relations between structure and function of these complexes, accompanying theoretical models and detailed simulations of the experiments are indispensable.

The description of the quantum dynamics of excitons in organic crystals and dye aggregates is well established [5–9]. Often there is no substantial overlap between the electronic wave functions of the different pigments in photosynthetic antenna systems and the theory of *Frenkel excitons* can be applied. Due to the Coulomb interaction an excited molecular state is not stationary and a partly delocalized excited state of the antenna can be formed. From this delocalization a number of collective optical properties of the aggregate result as it is well-known from the theory of J-aggregates [10].

The simulation of ultrafast nonlinear optical experiments on photosynthetic antenna systems demands for several extensions of the standard Frenkel exciton approach. This includes the incorporation of higher excited aggregate states [11,12] allowing to account for the simultaneous presence of two, three, or more excitations in a single PPC. The respective eigenstates are called *multi-exciton states* of the aggregate. Additionally, higher excited singlet states [13] of the monomeric pigments have to be introduced which are coupled to the multi-exciton states and, if combined with internal conversion processes, give rise to a microscopic description of exciton annihilation [14,15].

Another important issue concerns the role of the proteins, which are certainly more than a rigid scaffold for the pigments. The excitation transfer from the antenna pigments to the reaction center comes along with a spectral relaxation with the excess energy flowing into the protein environment. The electronic states of the pigments experience a dynamic modulation by the motion of the protein environment. Due to low-frequency vibrations of the protein and their high density of states, over a certain energetic range a quasi-continuum of vibrational states can be expected to exist. This energetic range accommodates typical energy differences between exciton states in antenna systems. Therefore if one pigment is excited, a dissipative exciton transfer results from the interaction of this pigment with the quasi-continuum of vibrational states of a neighboring pigment and its protein environment.

1.1. Aims and scope

Theoretical models and numerical simulations are at the heart of a well-funded interpretation of experimental observations. Having this in mind, it is our primary intention to give the reader an

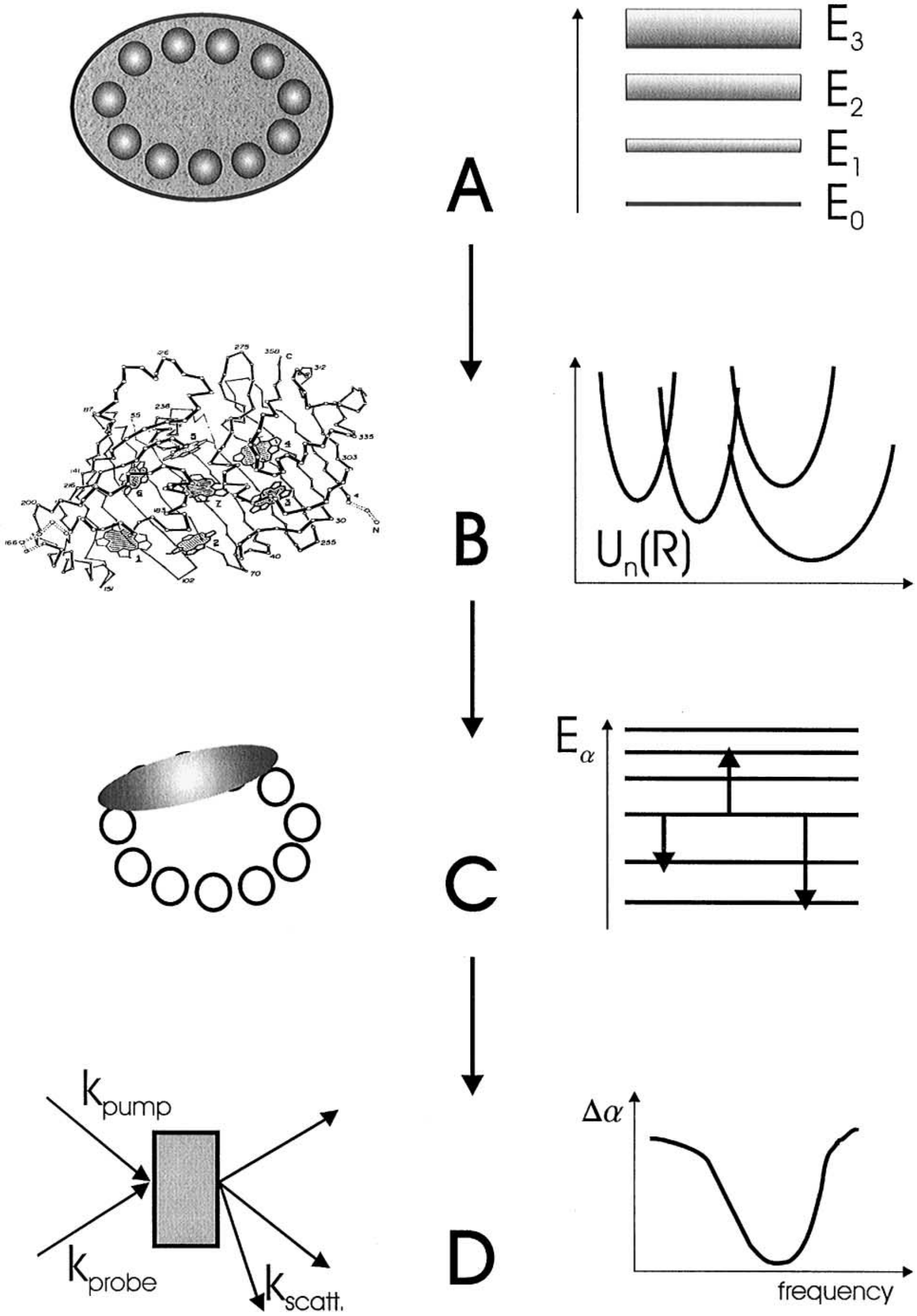
A
E3
E2
E1
E0
B
Un(R)
C
Eα
D
kpump
kprobe
kscatt.
Δα
frequency

overview of the theoretical apparatus developed to perform the simulations leading to linear and nonlinear optical spectroscopy. It goes without saying that the richness of the coupled motion of electronic and vibrational degrees of freedom (DOF) requires certain efforts and approximations before the internal PPC dynamics can be modelled.

In recent years, a number of reviews have been published on photosynthetic antenna systems covering experimental [16–19] as well as theoretical [20] aspects. Here we will focus on those concepts which are necessary to connect experimental findings and structural data to gain a deeper understanding of picosecond and sub-picosecond dynamics and its relevance for the biological function. It is important to keep in mind that all steps of the modeling have to be incorporated into numerical simulations. Quite naturally this will restrict the complexity of the model from the outset. Therefore, the main idea for simulating PPC dynamics and related optical spectra will be a combination of the derivation of microscopically correct formulas with the determination of the various parameters by comparison with experimental data.

A general overview about the steps leading from the microscopic structure to optical spectra can be found in Fig. 1. First, one has to relate the electronic properties of single Chl as well as structural data on the spatial arrangement of the Chl in the PPC to an electronic (or multi-excitonic) energy level scheme (panel (A) in Fig. 1). This level scheme including the Coulomb interaction between different molecular sites will be responsible for the main spectral features. In fact, a number of semiempirical and ab initio quantum chemical calculations exist in this respect. But due to the complexity of such calculations and the restricted computer power one usually has to stop at the description of electronic single excited PPC states. This is, however, insufficient for the simulation of nonlinear optical experiments. Furthermore, to account for static disorder one would have to repeat time-consuming quantum chemical calculations many times, a prohibitive task. Here we will prefer an approach which circumvents the calculation of the PPC electronic states but deduces as much information as possible from the comparison with optical spectra.

Panel (B) in Fig. 1 displays the next step along the road from the structure to the spectra. It concerns the vibrational modulation of the electronic structure. The theoretical description of electron–vibrational coupling (EVC) or multi-exciton–vibrational coupling is a fundamental aspect for exciton motion and relaxation. The task here is to relate intra-Chl vibrations as well as vibrations of the whole protein to *potential energy surfaces* (PES). For the electronic ground-state the PES is usually called energetic landscape. Already this type of PES is hardly obtainable, but trying to compute excited state PES of the PPC with quantum chemical methods seems to be rather hopeless. Again, it is the particular aspect of the approach reviewed here that we will

←

Fig. 1. Overview on the steps necessary when simulating PPC dynamics and related optical spectra (from above to below). Step A indicates the way from the PPC spatial structure to the related PPC electronic spectrum. The latter is given by the manifolds of multi-exciton levels. In step B, the vibrational modulation of the electronic levels has been accounted for by starting with the protein structure and its possible fluctuations and ending up with potential energy surfaces. These potential energy surfaces are the basis to describe electronic excitation energy relaxation. Step C displays dissipative exciton dynamics in the PPC and the interrelation between spatially localized or delocalized excitation energy motion and relaxation in the respective energy level scheme. To achieve a correct description of the PPC dynamics the electronic (A) and vibrational (B) states have to be modeled in a proper way. Step D shows that the excitation energy dynamics underlies the data obtained in an ultrafast optical experiment, for example in a pump–probe scheme. Here, the numerical simulation can be compared with experimental findings and probably one has to go back from D to A to redefine the theoretical models and parameters involved.

formulate general microscopic expressions for the respective coupling constants. But we will relate them to certain frequency-dependent functions, the spectral densities, which can be deduced from the experiment.

Having the electronic energy level structure of the PPC and its modulation by vibrational DOF at hand, the description of the dynamics of the electronic PPC excitations (exciton dynamics) is required. Here, spatial redistribution of optically injected excitation energy has to be confronted with relaxation processes in the multi-exciton manifolds, i.e. in the electronic PPC *eigenstates* (panel (C) of Fig. 1).

Finally, based on the model outlined so far one has to compute optical spectra measured either in the frequency-domain or in the (usually sub-picosecond) time-domain (panel (D) in Fig. 1). It is worth mentioning that the details we have to consider when going from spatial and electronic structure via dissipative exciton dynamics to, for example, femtosecond pump–probe spectra depend on the actual experimental observation. One basic conclusion resulting from this statement would be the possibility of a restriction to a certain set of electronic energy levels and excitations. Furthermore, the strength of the coupling to vibrational DOF as well the frequency resolution of the experiment decides about the level the protein motion has to be accounted for.

To summarize, what will be presented below is a microscopic theory of dissipative excitation energy transfer dynamics and its spectroscopic signatures. The appropriate theoretical tool to describe these phenomena typical for open quantum systems is given by the *density matrix theory*. It is formulated in such a manner that many microscopic parameters can be obtained by comparison with experimental findings. Thus, we provide the background for a model of intermediate complexity which nevertheless is capable to simulate a variety of linear and nonlinear optical experiments on photosynthetic PPCs.

The paper is organized as follows: In Section 2, we give an introduction into the relevant structural components of photosynthetic PPCs. Emphasis is put in Sections 3 and 4 on the derivation of appropriate model Hamiltonians which are capable of incorporating the results of spectroscopic and structural observations for different PPCs. Since we are aiming at a description of nonlinear optical spectroscopy care is taken to include monomeric double excitation as well as multi-excitation states in a unified manner. Concepts for treating exciton–vibrational interactions are reviewed in Section 4. The description of sub-picosecond excitation energy transfer dynamics including dissipation is given in Section 5. In Section 6, the relation between the observables of linear and nonlinear optical spectroscopy is established. The theoretical methods are then applied to describe exciton motion in the LH2 (Section 7), in the FMO complex (Section 8), and in the LHC-II (Section 9). Final conclusions are drawn in Section 10. Some more specific derivations are presented in the appendices.

2. The structural components of photosynthetic antennae

The discovery of antenna systems started with the pioneering work of two botanists, Emerson and Arnold [21], who used flash light measurements to estimate the efficiency for oxygen evolution of algae in 1932. From their results they concluded that only a small fraction ($<0.05\%$) of the pigments are directly involved in the photochemical reactions. In 1936 Gaffron and Wohl [22] postulated the existence of distinct functional units composed of 250–300 absorbing pigments and a photochemically active reaction center. The majority ($>99.5\%$) of chlorophylls and bacteriochlorophylls act as light absorbers, funneling the excitation energy to the reaction center where it is used to drive electron transfer reactions which in turn establishes a chemical potential gradient across the membrane. The overall quantum yield of this process exceeds 95% [23].

Whereas in antennae Chls and BChls are the primary excitation transfer pigments, in the bacterial reaction center, for instance, a BChl dimer functions as the electron donor. These multiple functionalities of the pigments are made possible by their local protein environment and their aggregation state. The protein serves several purposes, it gives the PPC its rigidity, fixes the pigments at their positions, and provides a heat sink for excess energy. In this section the relevant building blocks of photosynthetic antennae are introduced to provide a background for the theoretical models outlined subsequently.

2.1. The pigments: electronic structure

The most important photosynthetic active pigments are bacteriochlorophyll*a* (BChl*a*) and chlorophyll*a* (Chl*a*). Their structures are shown in Fig. 2. They represent the photochemically active part of the reaction centers in bacteria (BChl*a*) and in oxygen producing algae, cyano bacteria and green plants (Chl*a*). Moreover, they also form a major part of the antenna systems. However, in the latter they are accompanied by the so-called accessory pigments, i.e. phycobilines, carotenoids, Chl*b*, Chl*c*, BChl*c*, BChl*d*, BChl*e*, and BChl*g*. These accessory pigments absorb light at different wavelengths so as to energetically increase the absorption cross section of the antenna and hence of the reaction center. (Note that some species such as *Rhodopseudomonas* (*Rps.*) *viridis* have antennae composed of BChl *b* molecules [24].) In the antenna systems, which will be investigated below, besides BChl*a* and Chl*a*, Chl*b* and different carotenoids are found. In general, carotenoids add to the stability of the PPC, act as effective quencher for Chl triplet states (thus preventing formation of dangerous singlet oxygen), and participate in light harvesting [25,26]. Recently, there has also been an active discussion of the role carotenoids play in energy transfer between different parts of photosynthetic antennae (see, e.g., Ref. [19]). In addition, it has been demonstrated that ultrafast carotenoid band shifts can be used to probe the structure and dynamics of PPCs [27].

The optical properties of chlorophyll molecules are determined by extended conjugated π-electron systems (see, e.g., Ref. [28]). In the case of BChls and Chls one finds cyclic π-systems. The strong optical transitions in the blue (Soret band), in the red (Chl) or infrared (BChl) are due to $\pi \rightarrow \pi^*$ type transitions. According to the early work of Gouterman [29] these transitions arise from linear combinations of one-electron promotions between the two highest occupied (HOMO and HOMO-1) and the two lowest unoccupied (LUMO and LUMO + 1) π-type molecular orbitals (four orbital model). Usually, one denotes this set of orbitals by φ_1 to φ_4 in order of increasing energy. The resulting excited electronic states are labeled Q_y, Q_x, B_y, and B_x (see also [30]). The transitions into the Q_y and B_y state are mainly due to a transition from φ_2 to φ_3, and from φ_1 to φ_4, respectively, whereas transitions into the Q_x and B_x state are primarily caused by a transition from φ_2 to φ_4, and from φ_1 to φ_3, respectively. (For notational convenience we will also introduce a labeling like S_1, S_2, etc. for $Q_y, Q_x, \ldots$, respectively.)

The Q-bands (resulting from a subtractive promotion) are polarized in two orthogonal directions (Q_y (S_1) and Q_x (S_2)) in the red and near-infrared region, whereas an additive combination defines the transition to the high-energetic Soret band at 350–450 nm. The π-valence electron system of

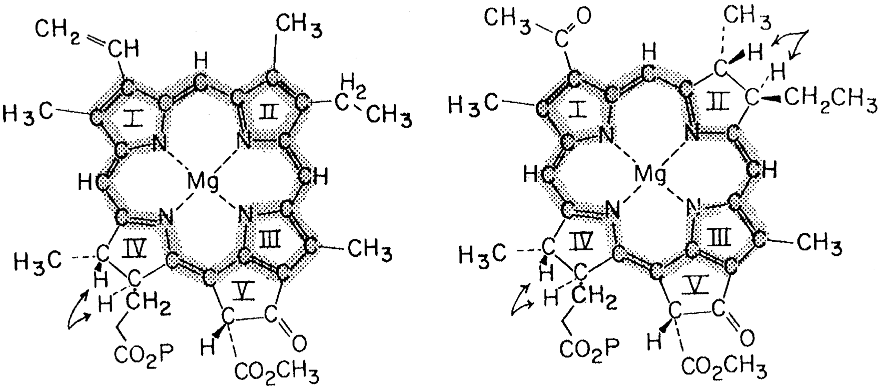

Fig. 2. Chlorophyll*a* (left) and bacteriochlorophyll*a* (right). The gray areas designate the cyclic π-electron system. The Chl*b* molecule which is present in the LHC-II besides the Chl*a* is structurally identically apart from a slight change in the pyrol ring II: the CH_3 group is replaced by $C=O\text{–}H$.

chlorophylls and bacteriochlorophylls can be understood as a disturbed ideal tetrapyrol π-system. The destabilization of the π-system arises from a successive saturation of the pyrol rings (ring IV for Chl, and rings II and IV in the case of BChls). In this way the two one-electron promotions loose their initial degeneracy. This causes a gain in oscillator strength of the subtractive combination at the expense of the high-energetic (additive) transition. In fact, the Q_y-transition of BChl is stronger than that observed in Chl. For example, in Ref. [31] the following dipole strengths of Q_y transitions in chlorophyll and bacteriochlorophyll were measured, BChl*a*: 37.6 D^2, Chl*a*: 24.65 D^2, and Chl*b*: 16.91 D^2. Moreover, the four-orbital theory of Gouterman is also capable to explain the red shift of this transition and other details such as, for example, the oxidation potentials. In Fig. 3, the relevant transitions between different electronic states of Chl*a* are shown. The energy of the first excited singlet state is solvent-dependent. For example, the Q_y-maximum of Chl*a* occurs in diethyl ether at 662 nm [32], whereas in ethanol [33] and carbon tetrachloride [31] it was measured at 665 nm. The S_2 (Q_x) and the S_3 (Soret) transitions occur around 579 and 415 nm, respectively [31]. The Q_y-transition of Chl*b* is shifted approximately 20 nm to the blue, whereas in BChl*a* this transition is red-shifted to 780 nm [31]. Careful analysis of the temperature dependence of absorption and fluorescence spectra of BChl*a* in glass-forming solvents gave evidence for inhomogeneities which become important in low-temperature environments [34]. The triplet states arise according to Gouterman from single HOMO → LUMO transitions. As it is shown for Chl*a* in Fig. 3 the energy of the first triplet state T_1 is well below the lowest excited singlet $Q_y(S_1)$ state. It should be noted that Gouterman's model has been verified by sophisticated quantum chemical calculations [28].

Information about higher excited intramolecular states is provided by nonlinear absorption techniques. In Refs. [35,36] the energetic position of the S_n-states and oscillator strengths of the related transitions of Chl*a* have been estimated. A rather broad absorption band was found indicating the presence of many S_n-states. A strong excited state absorption was also found for Chl*b* using transient holeburning [37]. Within a few picoseconds an occupation of higher excited S_n-states relaxes nonradiatively (internal conversion) to the first excited singlet S_1-state (cf. Fig. 3). Therefore independent of the excitation wavelength, fluorescence in these pigments starts from the S_1-state and takes place on a nanosecond time scale. However, about two-thirds of the S_1-state

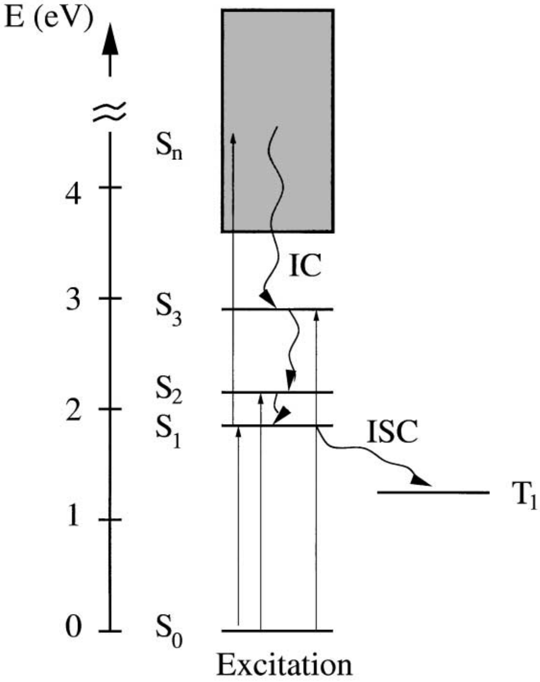

Fig. 3. Schematic view of energy levels of Chl*a* in solution and relevant electronic transitions.

population relaxes nonradiatively via spin-flip processes (intersystem crossing) to the T_1-triplet state which lives approximately 1 ms; in vivo this state is quenched by the carotenoids.

If pigments are arranged in a photosynthetic antenna complex there are two reasons why the energies of the pigments will be shifted: (i) the inter-pigment Coulomb interaction and (ii) the interaction with the protein environment. The former is responsible for the dynamics in the excited molecular state. The related energetic change is called *excitonic shift*. To distinguish the nonexcitonic shifts in pigment energies one introduces the so-called site energies. These are transition energies of the pigments in their local protein environment assuming that the mutual Coulomb interaction has been switched off. Possible nonexcitonic shifts arise from interaction of the pigments with charged or aromatic amino acid residues, from hydrogen bonding, from ligation of the central Mg-atom of the pigments to amino acid residues, from rotation of the pigments acetyl groups and from non-planarity of the pigments macrocycle (see the references given in [38]). Besides the pigment energies also the oscillator strengths of optical transitions of the pigments exhibit excitonic and nonexcitonic shifts.

2.2. *The pigments: intramolecular vibrations*

Resonance Raman spectroscopy has been used to investigate the vibrational spectra of the pigments, both in solution and in their natural environment. The observed vibrational frequencies can be related to the complex motion of the cyclic pigment skeleton, and some represent also more localized stretching modes of individual double bonds of the pigments.

An interesting feature of such spectra is their dependence on the coordination of the central magnesium atom. A comparison of the localized modes measured for isolated molecules in solution and for molecules in the protein was used to find those parts of the Chl and BChl skeleton which are modified by the interaction with the protein environment and hence play a prominent role in the intermolecular bonding. Besides the central magnesium atom, the 9-ketone and 2-acetyl carbonyl groups could be identified. For example, Lutz et al. [39] predicted the average out-of-plane angle of the acetyl groups of the BChls in a bacterial antenna system, a prediction which has been verified later by crystallographic experiments [40].

The vibrational spectrum contains many high-frequency modes ($>1000\,\mathrm{cm}^{-1}$), although there are also modes between 200 and $350\,\mathrm{cm}^{-1}$ which involve the motion of the central magnesium atom. Besides the Raman studies also high-resolution fluorescence experiments provided information about the vibrational spectrum [41,42].

2.3. Proteins

According to the complex structure of proteins their dynamics ranges from small-amplitude oscillations of single residues occurring on a subpicosecond and picosecond time scale to large-amplitude low-frequency motion of larger parts of the protein. Within the landscape theory of proteins the latter so-called conformational motion corresponds to a diffusion between the local minima of the high-dimensional energy landscape of the protein. This so-called spectral diffusion can be monitored by the change of the transition energy of a chromophore coupled to the protein. Spectral diffusion in proteins has been studied in the time domain by three-pulse photon echo [43] and in the frequency domain by hole burning experiments [44]. The obtained time scales range from nanoseconds until days, which is a manifestation of the protein's complexity.

From a theoretical point of view large-scale protein motion demands for a description beyond a harmonic approximation. In the 1980s it became possible to carry out molecular dynamics simulations focusing on deviations from the harmonic approximation for small model systems. Especially, at higher temperatures ($T > 100\,\mathrm{K}$) anharmonic behavior was found [45]. Molecular dynamics simulations also demonstrated the possibility to reduce the high-dimensional configuration space of the proteins. The concept of the important subspace has been introduced in this respect [46]. If the vibrational motion becomes anharmonic the important subspace cannot be obtained from a normal mode analysis, but a so-called principal component analysis can be applied to extract the important modes from a molecular dynamics simulation. For harmonic dynamics the principal component analysis is equivalent to a normal mode analysis of the protein motion. It is interesting to note that the numerical results obtained for small proteins indicate that the principal modes may be divided into two classes, (i) anharmonic modes characterized by large fluctuation amplitudes with multi-peaked distribution functions and (ii) harmonic modes with smaller amplitudes of fluctuations which are well approximated by a single Gaussian distribution [46]. As far as it concerns the role of proteins in photosynthetic energy transfer, a description which focuses on small-amplitude harmonic motions seems to be justified (see also [20]).

Much excitement and stimulation in the research on photosynthetic PPCs came from the discovery of coherent nuclear motion. It was first observed in the bacterial reaction center [47] at low temperatures and later even at room temperature [48]. Meanwhile it has also been discovered in the light-harvesting complexes LH1 and LH2 of purple bacteria [49,50]. The oscillation frequencies are in the range of about 100 cm^{-1}. An investigation of the pigment, i.e. BChl*a*, in solution did not show such pronounced oscillations [49]. Hence it can be assumed that the coherences have their origin in the motion of the protein. Alternatively, one could also think of a mixing of delocalized protein vibrations with low-frequency intramolecular modes of the pigments.

3. The exciton model for photosynthetic antennae

The investigation of Frenkel excitons in organic crystals and molecular systems like dye aggregates or polymer strands has a long tradition. In the late 1940s and early 1950s the field has been pioneered by Förster [51] and Dexter [52]. Later Davydov [5] and Agranovich [9] established the theoretical basis for the description of electronic excitations, EVC, and excitation transfer dynamics. During the last decade the activities have been concentrated on the formulation of models adequate for the description of nonlinear spectroscopy, in particular in the ultrafast (femtosecond) domain. This required to include multiple electronic excitations and the utilization of techniques of dissipative quantum dynamics (see e.g. [10,53]). The fundamental nonlinear electronic excitation, the two-exciton state, which appears if two molecules of the same complex (or aggregate) are excited simultaneously, has been suggested to be responsible for nonlinear optical processes in dye aggregates [54–56].

Interestingly, the development in the field of Frenkel excitons found an immediate application to photosynthetic research (for an earlier review see [7]). Nowadays the study of light-harvesting antennae and PPC is a subject not only for biologists, but experimental and theoretical physics and chemistry have entered this field. Accordingly, one can state that the investigation of PPC acts back on the development of the concepts for Frenkel excitons in other molecular systems.

This section as well as Sections 4 and 5 are aimed to establish the basis for the description of electronic and vibrational excitations as well as their coupled dynamics in PPCs. First, we will review different approaches to the systematic description of multiple electronic excitations of PPCs. Some recent attempts to calculate the PPC electronic states either on an ab initio or a semiempirical level of quantum chemistry are discussed in Section 3.2. However, all these calculations are restricted to the lowest electronic excitation (single-exciton state) and they are unable to give quantitative hints on the strength of the exciton–vibrational coupling. Circumventing this problem we will start the description by using local Chl-states (site representation), as it is known from the traditional theory of Frenkel excitons (see, e.g., [9,53,57]). For the topics discussed in this review it suffices to formulate the site representation in an electronic two-level model for every Chl (Section 3.3) or in a three-level model (to account, in a later step, for intra-Chl excited state absorption, Appendix A). The results derived in these sections are used in Section 3.4 to diagonalize the electronic PPC Hamiltonian and to introduce *multi-exciton states* as well as their coupling to the radiation field (Section 3.5). The multi-exciton states represent the electronic *eigenstates* of the PPC and are of basic importance for the correct description of relaxation as discussed in Section 5.

3.1. The Hamiltonian of the pigment–protein complex

In order to arrive at the stationary Schrödinger equation and the respective Hamiltonian for the complete PPC we assume that there are N_{Chl} Chl molecules labeled by m and positioned (center of mass) at $\mathbf{z}_m$. The respective PPC Hamiltonian reads

$$H_{\mathrm{PPC}} = H_{\mathrm{el}}(r,R) + T_{\mathrm{nuc}} + V_{\mathrm{nuc\text{-}nuc}}(R)\ . \tag{1}$$

H_{el} comprises all electronic contributions of the various Chls. The complete set of electronic coordinates is denoted by r. The subset of the electronic coordinates belonging to Chl m will be labeled by r_m. All electronic contributions from the protein can be neglected for the present purpose. Throughout triplet excitation will not be considered which enables us to neglect the electron's spin.

Additionally, the electronic Hamiltonian H_{el} depends parametrically on the complete set, R, of nuclear DOF. The nuclear kinetic energy is given by T_{nuc} and the inter-nuclear interaction has been denoted by $V_{\mathrm{nuc\text{-}nuc}}$. In most cases a restriction to valence electrons is sufficient, i.e., "nuclei" means nuclei plus core electrons. The whole set of nuclear DOF can be separated into intramolecular coordinates R_{intra} and intermolecular coordinates R_{inter}. The former can be further subdivided into single-Chl sets $R_m^{(\mathrm{intra})}$. The intermolecular coordinates characterizing the relative positions of the various Chls in the PPC; they have to be understood as a part of the protein coordinates R_{protein}. A similar separation follows for the nuclear kinetic energy operator. The coupling $V_{\mathrm{nuc\text{-}nuc}}(R)$ splits up into a pair-wise combination of different types of nuclear DOF:

$$V_{\mathrm{nuc\text{-}nuc}}(R) = \sum_m \left(V_{\mathrm{nuc\text{-}nuc}}(R_m^{(\mathrm{intra})}) + V_{\mathrm{nuc\text{-}nuc}}(R_m^{(\mathrm{intra})}, R_{\mathrm{protein}})\right) + V_{\mathrm{nuc\text{-}nuc}}(R_{\mathrm{protein}})\ . \tag{2}$$

The contribution $V_{\mathrm{nuc-nuc}}(R_m^{(\mathrm{intra})})$ describes the coupling among the intra-Chl nuclear DOF in the mth chromophore. The interaction of these DOF with the protein coordinates are accounted for via the potential $V_{\mathrm{nuc\text{-}nuc}}(R_m^{(\mathrm{intra})}, R_{\mathrm{protein}})$. Both contribution are additive with respect to the Chl-index m. An additional contribution is given by the pure protein part $V_{\mathrm{nuc\text{-}nuc}}(R_{\mathrm{protein}})$.

Next, let us specify the electronic Hamiltonian in more detail. It can be written as

$$H_{\mathrm{el}} = \sum_m H_m^{(\mathrm{el})} + \frac{1}{2}\sum_{\substack{m,n\\ m\neq n}} V_{mn}^{(\mathrm{el\text{-}el})}\ , \tag{3}$$

where $H_m^{(\mathrm{el})}$ denotes the single-Chl contribution and $V_{mn}^{(\mathrm{el-el})}$ the mutual Chl–Chl Coulomb interaction. Let us discuss the single Chl contribution: The different types of electronic Chl excitations and their classification have been explained in Section 2.1. For the following we label the electronic states (S_0, S_1, etc., compare Fig. 3) by a. They are defined via the following stationary Schrödinger equation:

$$H_m^{(\mathrm{el})}(R)\varphi_{ma}(R) = \varepsilon_{ma}(R)\varphi_{ma}(R)\ . \tag{4}$$

The solution of Eq. (4) gives the site energies ε_{ma}. They are different from the Chl energies in the gas phase since $H_m^{(\mathrm{el})}(R)$ includes the influence of the whole protein environment, but not of the other Chl molecules. The single-Chl electronic Hamiltonian can be further split up into $H_m^{(\mathrm{el})} = T_{\mathrm{el}} + V_{\mathrm{el\text{-}el}}(r_m) + V_{\mathrm{el\text{-}nuc}}(r_m, R)$. The kinetic energy operator includes the contribution of all electrons from Chl m. $V_{\text{el-el}}(r_m)$ denotes the internal electron–electron Coulomb interaction; it only depends on the coordinate set r_m. Electron–nuclei interaction is denoted by $V_{\text{el-nuc}}$ comprising the coupling to all nuclear DOF of the PPC $V_{\text{el-nuc}}(r_m, R) = V_{\text{el-nuc}}(r_m, R_m^{(\text{intra})}) + \sum_{n \neq m} V_{\text{el-nuc}}(r_m, R_n^{(\text{intra})}) + V_{\text{el-nuc}}(r_m, R_{\text{protein}})$. The first contribution describes the coupling to the nuclear DOF of the same Chl whereas the second sum includes the coupling to all other Chl of the PPC. The last term accounts for the coupling to protein vibrations. Since our approach does not take into account the electronic structure of the protein the quantity $V_{\text{el-nuc}}(r_m, R_{\text{protein}})$ has to be understood as an effective coupling also determined by the electrons of the various protein parts.

3.2. Electronic states of the pigment–protein complex

In order to treat the interacting pigments of a PPC we start from the solutions of Eq. (4) which give the energies ε_{ma} and electronic wave functions φ_{ma} of a single Chl. Since the approach accounts for the influence of the surrounding protein, the obtained energies are called site energies and may differ for the Chls in the PPC. Then, the φ_{ma} can be used to construct the electronic wave function for all Chls in the PPC. The details of this procedure depend on the actual geometry of the PPC. If the Chl molecules are close to each other (< 10 Å, [58]) wave function overlap and charge transfer states have to be incorporated [59–61]. Otherwise, only the pure Coulomb interaction of electrons belonging to different pigments has to be considered (see, e.g., [62]).

To classify the electronic states with respect to the various intramolecular electronic excitations we introduce a Hartree-type product ansatz (not antisymmetrized)

$$\phi_A^{\text{HP}}(\{r_m\}; R) = \prod_{m=1}^{N_{\text{mol}}} \varphi_{ma}(r_m; R) \ . \tag{5}$$

The multi-index $A \equiv \{a\} = (a_1, \dots, a_{N_{\text{Chl}}})$ defines the electronic configuration of the PPC based on the zeroth-order states φ_{ma}. Next, an antisymmetrization of ϕ_A^{HP} is introduced:

$$\phi_A(\{r_m\}; R) = \frac{1}{\sqrt{N_{\text{p}}!}} \sum_{\text{perm}} (-1)^p \mathscr{P}[\phi_A^{\text{HP}}(\{r_m\}; R)] \ . \tag{6}$$

Here, $\mathscr{P}$ generates a permutation of electron coordinates of different molecules in the PPC, and p counts the number of permutations. Expanding the Schrödinger equation for the PPC electronic state $|\psi\rangle$ with respect to the basis (6) as $|\psi\rangle = \sum_A C(A)|\phi_A\rangle$ one obtains $\sum_B (\langle\phi_A|H_{\text{el}}|\phi_B\rangle - E\langle\phi_A|\phi_B\rangle) = 0$. Since the single-Chl functions are assumed to be known the main difficulty here is to calculate matrix elements of the Coulomb interaction operator. For two Chls labeled 1 and 2, the matrix elements describe the direct contribution J_{12} and the exchange contributions K_{12} and we have

$$\langle \phi_{a_1 a_2} | V_{12}^{(\text{el-el})} | \phi_{b_1 b_2} \rangle = J_{12}(a_1, a_2, b_2, b_1) - K_{12}(a_1, a_2, b_2, b_1) \ . \tag{7}$$

Using the concept of transition densities [62] $\rho_{mab}(r_m) = \varphi_{ma}^*(r_m)\varphi_{mb}(r_m)$ the direct Coulomb interaction can be written as

$$J_{12}(a_1, a_2, b_2, b_1) = \int \mathrm{d}r_1 \, \mathrm{d}r_2 \, \rho_{1a_1b_1}(r_1) V_{12}^{(\text{el-el})} \rho_{2a_2b_2}(r_2) \ . \tag{8}$$

If the spatial extension of the transition density is comparable to the inter-Chl distance or larger, one has to use Eq. (8) for J_{12}. This is the case for the LH2 complex of purple bacteria where the inter-Chl distance is less than 10 Å. For other types of PPCs a multipole expansion is possible with the dipole–dipole coupling as the leading term ($\boldsymbol{n}_{12} = (z_1 - z_2)/|z_1 - z_2|$, z_1 and z_2 denote the center of mass coordinates of both Chl):

$$J_{12}(a_1, a_2, b_2, b_1) = \frac{(\boldsymbol{d}^{(1)}_{a_1 b_1}, \boldsymbol{d}^{(2)}_{a_2 b_2}) - 3(\boldsymbol{d}^{(1)}_{a_1 b_1}, \boldsymbol{n}_{12})(\boldsymbol{d}^{(2)}_{a_2 b_2}, \boldsymbol{n}_{12})}{|z_1 - z_2|^3} . \tag{9}$$

This expression includes dipole operator matrix elements

$$\boldsymbol{d}^{(m)}_{ab} = \langle \varphi_{ma} | \hat{\mu}_m | \varphi_{mb} \rangle \tag{10}$$

with the Chl (electronic) dipole operator given as

$$\hat{\mu}_m = \sum_{r_m} e\boldsymbol{r}_m . \tag{11}$$

The exchange part $K_{12}(a_1, a_2, b_2, a_1)$ is mainly determined by the spatial overlap between molecular orbitals, which belong to Chl 1 and to Chl 2. Such a wave function overlap decreases exponentially with increasing intermolecular distance. Usually, for distances larger than about 1 nanometer one can neglect the exchange contributions to the interaction energy. In principle, for a system like the LH2 neither the use of J_{12} according to Eq. (9) nor the neglect of exchange contributions is rigorously justified. However, quite often the approximate coupling expression, Eq. (9), is taken as an *effective interaction* with effective transition dipole moments and reduced by the dielectric constant accounting for the screening effect due to the protein environment [63–65].

The determination of the PPC electronic state becomes extremely involved if one steps from the Chl states to the total PPC electronic wave function $|\psi\rangle = \sum_A C(A)|\phi_A\rangle$. Recently, this problem has been approached using different levels of sophistication. Here the focus has been mainly on the LH2 of purple bacteria whose structure is well-defined. There are a number of calculations of effective Hamiltonians using a point-dipole [65–69] or a point-monopole [70] description. Based on a semiempirical QCFF/PI (quantum mechanical consistent-force-field/π-electron) approach absorption and circular dichroism spectra for *Rps. acidophila* have been calculated in Ref. [59]. A semiempirical INDO/S configuration interaction calculation on the single-excitation level has been presented for *Rhodospirillum* (*Rs.*) *molischianum* in Ref. [60]. While in this work the protein environment has been modeled by a dielectric constant, there are attempts to include parts of the protein explicitly. Linnanto et al. [71] reported results of a configuration interaction exciton method (based on the semiempirical ZINDO/S level of theory) including histidine residues. They estimated the effective Coulomb interaction matrix elements by comparing a dimer supermolecule calculation with the respective monomer result. As another application of semiempirical methods the structure of the whole photosynthetic unit of *Rhodobacter* (*Rb.*) *spheroides* has been proposed based on the assumed homology with known structures of other bacteria [65].

There are also a number of ab initio calculations (CIS level) for supermolecule-type substructures of the PPC. Particularly, the results gave valuable insight into the nature of the Coulomb interaction which is not necessarily well-described within the dipole approximation (see above)

[62]. These type of calculations also included parts of the protein (Mg ligands and H-bonding residues [61]) or focused on the role of carotenoids [72].

All calculations reported so far have been restricted to the case of a single excitation only. Further, in view of the complex structure of the PPCs there appears to be no easy way to elucidate the effect of nuclear motions, or even to obtain a PES. However, these two extensions are of primary importance for the description of nonlinear optical spectroscopy.

Here we proceed with the PPC wave function ansatz, Eq. (5) (or Eq. (6)) assuming that the Chl wave functions are known. Concentrating on the Hartree ansatz (5) we will use the notation

$$|\phi_A\rangle \equiv |\phi_A^{\mathrm{HP}}\rangle\ . \tag{12}$$

As a consequence of the neglect of intermolecular wave function overlap, the states $|\phi_A\rangle$ form a complete basis. The ansatz Eq. (12) enables us to introduce the electronic PPC unit operator as

$$\mathbf{1}_{\mathrm{PPC}} = \sum_A |\phi_A\rangle\langle\phi_A|\ . \tag{13}$$

The expansion of the Hamiltonian Eq. (3) follows as

$$H_{\mathrm{el}} \equiv \mathbf{1}_{\mathrm{PPC}} H_{\mathrm{el}} \mathbf{1}_{\mathrm{PPC}} = \sum_{A,B} \langle\phi_A|H_{\mathrm{el}}|\phi_B\rangle|\phi_A\rangle\langle\phi_B|\ . \tag{14}$$

The single-Chl contributions to H_{el} result in single-molecule matrix elements of the following type $\langle\varphi_{ma}|H_m^{(\mathrm{el})}|\varphi_{ma}\rangle \equiv \varepsilon_{ma}$. Two-state terms follow from the interaction contribution where the wave functions are arranged in a way such that exchange contributions do not appear. Although we have restricted ourselves to a two-center integral, four different electronic quantum numbers have to be considered. According to the two types of matrix elements the expansion can be written as

$$H_{\mathrm{el}} = \left\{\sum_{ma} \varepsilon_{ma}|\varphi_{ma}\rangle\langle\varphi_{ma}| + \frac{1}{2}\sum_{mn}\sum_{abcd} J_{mn}(a,b,c,d)|\varphi_{ma}\rangle\langle\varphi_{md}|\otimes|\varphi_{nb}\rangle\langle\varphi_{nc}|\right\}\mathbf{1}_{\mathrm{PPC}}\ . \tag{15}$$

Clearly, the electronic PPC unit operator can be neglected, but it is important to keep in mind that the remaining Hamiltonian is exclusively defined in this electronic N_{Chl}-PPC state space. The quantity J_{mn} abbreviates the inter-pigment matrix element of $V_{mn}^{(\mathrm{el-el})}$ involving different types of transitions.

For further considerations we will restrict the complete electronic spectrum of the various Chl to the (singlet) ground-state, i.e. $a = S_0 \equiv g$, the first excited singlet state with $a = S_1 \equiv e$, and a higher excited singlet state $a = S_n \equiv f (n > 1)$. The latter is fixed by the condition $\varepsilon_e - \varepsilon_g \approx \varepsilon_f - \varepsilon_e$ and has been introduced to account for intra-Chl excited state absorption [13,67]. The present state-space reduction allows to classify the electronic PPC configurations with respect to the number of (elementary) excitations with energy approximately equal to the S_0–S_1 transition. For the following it will be instructive to carry out this classification within an electronic two-level model first, i.e. to neglect the S_n-state. The steps necessary for including this state are sketched in Appendix A.

3.3. The chlorophyll two-level model and the site representation

In the two-level model for the various Chls of the PPC we consider the electronic ground-state φ_{mg} and a single excited state φ_{me} per Chl molecule. To specify the inter-Chl electronic Coulomb interaction, Eq. (9) we neglect diagonal dipole operator matrix elements ($\boldsymbol{d}_{gg}^{(m)}$, $\boldsymbol{d}_{ee}^{(m)} = 0$) and restrict ourselves to off-diagonal matrix elements $\boldsymbol{d}_{eg}^{(m)}$ (of the dipole operator in the dipole–dipole coupling). Furthermore, contributions proportional to, e.g. $|\varphi_{me}\rangle\langle\varphi_{mg}|\otimes|\varphi_{ne}\rangle\langle\varphi_{ng}|$ are neglected. This approximation which discards the simultaneous excitation (or de-excitation) of both Chl is known as the Heitler–London approximation (for a recent discussion see [10]). For the dipole–dipole coupling it gives ($\hat{J}_{mn}$ denotes the operator of the Coulomb coupling)

$$\frac{1}{2}\sum_{m,n} \hat{J}_{mn} = \sum_{m,n} J_{mn}|\varphi_{me}\rangle\langle\varphi_{mg}|\otimes|\varphi_{ng}\rangle\langle\varphi_{ne}| \tag{16}$$

with

$$J_{mn} = \frac{(\boldsymbol{d}_{eg}^{(m)}\boldsymbol{d}_{eg}^{(n)*}) - 3(\boldsymbol{d}_{eg}^{(m)}\boldsymbol{n}_{mn})(\boldsymbol{d}_{eg}^{(n)*}\boldsymbol{n}_{mn})}{|\boldsymbol{z}_m - \boldsymbol{z}_n|^3} . \tag{17}$$

The complete electronic Hamiltonian is obtained as

$$H_{\mathrm{el}} = \sum_{m} \{\varepsilon_{mg}|\varphi_{mg}\rangle\langle\varphi_{mg}| + \varepsilon_{me}|\varphi_{me}\rangle\langle\varphi_{me}|\} + \sum_{m,n} J_{mn}|\varphi_{me}\rangle\langle\varphi_{mg}|\otimes|\varphi_{ng}\rangle\langle\varphi_{ne}| . \tag{18}$$

There exists an alternative notation for the Hamiltonian using *second quantization* operators. This notation does not introduce any additional assumptions or extensions of the model but sometimes provides a clearer description. To this end one introduces excitation (creation) operators

$$B_m^+ = |\varphi_{me}\rangle\langle\varphi_{mg}| \tag{19}$$

and de-excitation (annihilation) operators

$$B_m = |\varphi_{mg}\rangle\langle\varphi_{me}| . \tag{20}$$

The operators result in an excitation or de-excitation, respectively, of the *m*th Chl and have to be understood as quantities acting in the complete PPC electronic state space. The operators are of the Pauli type obeying the commutation relations

$$[B_m^+, B_n]_+ = \delta_{mn} + (1 - \delta_{mn})2B_m^+ B_n \tag{21}$$

and

$$[B_m^+, B_n^+]_+ = (1 - \delta_{mn})2B_m^+ B_n^+ . \tag{22}$$

The electronic Hamiltonian can be written as

$$H_{\mathrm{el}} = \sum_{m} (\varepsilon_{mg} B_m B_m^+ + \varepsilon_{me} B_m^+ B_m) + \sum_{\substack{m,n \\ m \neq n}} J_{mn} B_m^+ B_n . \tag{23}$$

Using relation (21) a more common notation can be derived (see e.g. [57,73,74]). For this reason, we introduce the PPC electronic ground state energy:

$$E_0 = \sum_m \varepsilon_{mg} \; . \tag{24}$$

In the present description, it gives the exact electronic ground state energy since the inter-pigment Coulomb interaction has been approximated by the coupling of transition dipoles, Eq. (17). Furthermore, we define the single-Chl excitation energy

$$\varepsilon_m(eg) = \varepsilon_{me} - \varepsilon_{mg} \tag{25}$$

and get

$$H_{\mathrm{el}} = E_0 \mathbf{1}_{\mathrm{PPC}} + \sum_{m,n} (\delta_{mn}\varepsilon_m(eg) + (1-\delta_{mn})J_{mn})B_m^+ B_n \; . \tag{26}$$

The main building block of this Hamiltonian is a $N_{\mathrm{Chl}} \times N_{\mathrm{Chl}}$ matrix with the excitation energies of the various Chl on its diagonal and the Coulomb couplings on its off-diagonals. As it is the case for expression (18), the derived Hamiltonian is valid for any excited PPC state based on the Chl two-level model.

It is advisable to introduce an ordering of the excited electronic PPC states which is related to the optical experiments used to study PPC properties. In a linear absorption experiment the energy of a single photon is deposited into the PPC leading to an excitation of a single Chl molecule into a particular excited state (or more general, leading to a superposition of single Chl states, i.e. to a PPC eigenstate). The lowest excited electronic states are of primary importance in this respect. Since the intensity of the sunlight is weak, this single excited PPC state is the only one of interest under physiological conditions. But applying nonlinear spectroscopic techniques some higher excited electronic states of the PPC can be populated. We mention the two-exciton and the three-exciton state with two or three excited chromophores, respectively, present in the PPC. Higher intra-chromophore excitations have to be considered, too. All these states will be called *multi-excitation states* of the PPC.

In the following, we will classify the excited electronic states of the PPC starting with the ground state and introducing step by step higher excited states. Multiple electronic excitations of PPCs have been proposed in [54–56]. A first experimental verification in pseudo-isocyanine dye aggregates in solution could be given in [11]. In the earlier literature on the theory of Frenkel-excitons [5,8,9] an exclusive concentration on single-excited states prevailed. This is surprising since multiple exciton systems either as free moving Wannier–Mott excitons or as bound excitons are investigated in semiconductor physics since the early seventies.

The ordering of the states is achieved if the total wave function is classified with respect to the number N of excited Chl molecules. The related state contains the subset $\{m\}_N$ of excited Chls and the subset $\{n\}_{N_{\mathrm{Chl}}-N}$ of $N_{\mathrm{Chl}}-N$ Chls in the ground state. The (zeroth-order) state vector can be written as $|\{m\}_N\rangle \equiv |m_1, m_2, \ldots, m_{N_{\mathrm{Chl}}}\rangle$. The ground state $|0\rangle$ with zero excitations is the product state of all electronic ground state molecular wave functions

$$|0\rangle = \prod_n |\varphi_{ng}\rangle \; . \tag{27}$$

The first excited state of the PPC is characterized by the presence of a single molecular excitation (from the electronic ground state S_0 to the first excited singlet state S_1). It reads

$$|m\rangle = |\varphi_{me}\rangle \prod_{n \neq m} |\varphi_{ng}\rangle \; . \tag{28}$$

Here, every Chl is in its electronic ground state except molecule m, which has been excited to state $e \equiv S_1$. Two excited Chls are described by

$$|m,n\rangle = |\varphi_{me}\rangle|\varphi_{ne}\rangle \prod_{k \neq m,n} |\varphi_{kg}\rangle \; . \tag{29}$$

For most nonlinear optical experiments the inclusion of these three types of states is sufficient. Nevertheless, it is of general interest to formulate the approach independent of the actual number of excited Chls. The general type of state vector in the case of N excitations reads

$$|\{m\}_N\rangle = \prod_{k=m_1}^{m_N} |\varphi_{ke}\rangle \prod_{l=n_1}^{n_{N_{\mathrm{Chl}}-N}} |\varphi_{lg}\rangle = \left(\prod_{k=m_1}^{m_N} B_k^+ \right)|0\rangle \; , \tag{30}$$

where in the last part the excitation operators, Eq. (19) have been used.

Introducing the N-excitation subspace projector

$$\hat{P}_N = \sum_{\{m\}_N} |\{m\}_N\rangle\langle\{m\}_N| \; , \tag{31}$$

the classification scheme for the possible electronic configurations of the PPC can be formally understood as a rearrangement of particular terms in the unit operator

$$\mathbf{1}_{\mathrm{PPC}} = \sum_{N=0}^{N_{\mathrm{Chl}}} \hat{P}_N \; . \tag{32}$$

The summation in the projector has to be carried out over all possible states with N excitations. The expansion of the unit operator results in the expansion of the electronic PPC Hamiltonian

$$H_{\mathrm{el}} = \sum_N H_{\mathrm{el}}^{(N)} \hat{P}_N \; , \tag{33}$$

where $H_{\mathrm{el}}^{(N)}$ exclusively acts in the N-excitation subspace. The number N represents a good quantum number and will be used in all forthcoming considerations to classify the PPC spectrum and related transition processes.

To obtain $H_{\mathrm{el}}^{(N)}$ we have to determine the action of H_{el}, Eq. (23) on $|\{k\}_N\rangle$. It results in

$$H_{\mathrm{el}}^{(N)} = \sum_{\{k\}_N} \left(\sum_{m \notin \{k\}_N} \varepsilon_{mg} + \sum_{m \in \{k\}_N} \varepsilon_{me} + \sum_{m \notin \{k\}_N} \sum_{n \in \{k\}_N} J_{mn} B_m^+ B_n \right) |\{k\}_N\rangle\langle\{k\}_N| \; . \tag{34}$$

For an alternative notation we split off the energy of the PPC electronic ground state E_0, Eq. (24) and write

$$H_{\mathrm{el}}^{(N)} = E_0 + \mathscr{H}_{\mathrm{el}}^{(N)} \tag{35}$$

with

$$\mathscr{H}_{\mathrm{el}}^{(N)} = \sum_{\{k\}_N} \left(\sum_{m\in\{k\}_N} \varepsilon_m(eg) + \sum_{m\notin\{k\}_N} \sum_{n\in\{k\}_N} J_{mn} B_m^+ B_n \right) |\{k\}_N\rangle\langle\{k\}_N| \,. \tag{36}$$

Here, $\varepsilon_m(eg)$, Eq. (25) is the electronic excitation energy of the mth chromophore.

It is instructive to give explicit expressions for the N-excitation Hamiltonian for the lowest excited PPC-states. The Hamiltonian in the presence of a single electronic excitation reads

$$\begin{aligned}\mathscr{H}_{\mathrm{el}}^{(1)} \equiv \mathscr{H}_{\mathrm{el}}^{(1)}\hat{P}_1 &= \sum_m \varepsilon_m(eg) B_m^+ B_m + \sum_{\substack{m,n\\ m\neq n}} J_{mn} B_m^+ B_n \\ &= \sum_m \varepsilon_m(eg)|m\rangle\langle m| + \sum_{\substack{m,n\\ m\neq n}} J_{mn}|m\rangle\langle n| \,. \end{aligned}\tag{37}$$

Both notations are common in the literature dealing with single-excitation properties of dye aggregates and chromophore complexes. For the presence of two electronic excitations the respective Hamiltonian reads

$$\begin{aligned}\mathscr{H}_{\mathrm{el}}^{(2)}\hat{P}_2 &= \sum_{k\neq l} \left(\varepsilon_k(eg) + \varepsilon_l(eg) + \sum_{m\neq k,\, l} (J_{mk} B_m^+ B_k + J_{ml} B_m^+ B_l) \right) |k,l\rangle\langle k,l| \\ &= \sum_{k\neq l} (\varepsilon_k(eg) + \varepsilon_l(eg))|k,l\rangle\langle k,l| + \sum_{k\neq l} \sum_{m\neq k,l} (J_{mk}|m,l\rangle\langle k,l| + J_{ml}|k,m\rangle\langle k,l|) \,. \end{aligned}\tag{38}$$

All formulas given so far for the two-level model of the single Chl can be easily extended to the three-level case and are summarized in Appendix A.

If it is possible to restrict the considerations to a linear arrangement of Chl molecules with a nearest-neighbor Coulomb coupling an alternative description of the various excited electronic states can be given [74,75]. It is based on the Jordan–Wigner transformation applied to the open-chain version of Hamiltonian H_{el}, Eq. (23). It results in a Hamiltonian formulated in terms of Fermi operators instead of the Pauli operators B_m^+ and B_m. If diagonalized the multiple electronic excitations reduce to a system of noninteracting fermions. Unfortunately, this elegant way to describe the electronic excitations is restricted to a chain of chromophores and therefore of less importance for PPCs.

3.4. Multi-exciton states and multi-exciton expansion

The determination of the eigenstates of the electronic PPC Hamiltonian H_{el} results in the so-called *multi-exciton states* $|\alpha_N\rangle$. They describe the delocalization (or partial delocalization) of simultaneously excited states at different Chls. To indicate that the multi-exciton state belongs to the N-excitation manifold the multi-exciton quantum number α will be given the subscript N. To solve the stationary Schrödinger equation for the multi-exciton state one introduces a superposition of state vectors $|\{m\}_N\rangle$ according to

$$|\alpha_N\rangle = \sum_{\{n\}_N} C_{\alpha_N}(\{n\}_N)|\{n\}_N\rangle \,. \tag{39}$$

The summation includes all possible configurations in the PPC which contain excitations of N different molecules. The expansion coefficients C define the N-exciton wave function (in the site-representation) and are labeled by the N-exciton quantum number α_N. Next, we formulate the eigenvalue equation for the multi-exciton state with reference to the ground state energy E_0, Eq. (24):

$$\mathscr{H}_{\mathrm{el}}^{(N)}|\alpha_N\rangle = E_{\alpha_N}|\alpha_N\rangle \; . \tag{40}$$

Inserting Hamiltonian (36) and multiplying with the state vector $|\{m\}_N\rangle$ from the left we obtain for the expansion coefficients

$$\left(E_{\alpha_N} - \sum_{k\in\{m\}_N} \varepsilon_m(eg)\right)C_{\alpha_N}(\{m\}_N) = \sum_{k\notin\{m\}_N}\sum_{l\in\{m\}_N} J_{kl}C_{\alpha_N}(\{m\}_{N|l\to k}) \; . \tag{41}$$

The label $l \to k$ at the expansion coefficient on the right-hand side of Eq. (41) indicates a particular interchange of the site indices l and k. The notation has been chosen to highlight that the excitation at molecule l is a part of the multi-excitation configuration $\{m\}_N$; $l \to k$ indicates that this excitation has been transferred to a site k which does not belong to the configuration $\{m\}_N$.

As a special case of Eq. (41) we obtain the eigenvalue equation for the one-exciton expansion coefficients as (α_1 covers N_{Chl} different values):

$$(E_{\alpha_1} - \varepsilon_m(eg))C_{\alpha_1}(m) = \sum_{n\neq m} J_{mn}C_{\alpha_1}(n) \; . \tag{42}$$

Correspondingly, the respective two-exciton equation reads (note $m \neq n$, here α_2 covers $N_{\mathrm{Chl}}(N_{\mathrm{Chl}}-1)/2$ different values)

$$(E_{\alpha_2} - \varepsilon_m(eg) - \varepsilon_n(eg))C_{\alpha_2}(m,n) = \sum_{k\neq m,n} (J_{km}C_{\alpha_2}(k,n) + J_{kn}C_{\alpha_2}(m,k)) \; . \tag{43}$$

The solution of the multi-exciton equation (41) enables us to introduce a new notation of the PPC unit operator Eq. (13). By expanding the projector $\hat{P}_N$ with respect to the multi-exciton states of manifold N we may write

$$\hat{P}_N = \sum_{\alpha} |\alpha_N\rangle\langle\alpha_N| \; . \tag{44}$$

Using the same expansion for the N-excitation Hamiltonian, Eq. (36) it becomes diagonal

$$\mathscr{H}_{\mathrm{el}}^{(N)} = \sum_{\alpha} E_{\alpha_N}|\alpha_N\rangle\langle\alpha_N| \; . \tag{45}$$

3.5. Coupling to the radiation field

To simulate optical experiments on PPCs it is sufficient to take the coupling to the radiation field in the electric dipole approximation resulting in the following expression to be added to the PPC Hamiltonian, Eq. (1):

$$H_{\mathrm{F}}(t) = -\boldsymbol{E}(\boldsymbol{r},t)\hat{\mu}_{\mathrm{PPC}} \; . \tag{46}$$

The dipole operator of the total PPC reads

$$\hat{\mu}_{\mathrm{PPC}} = \sum_m \hat{\mu}_m \;, \tag{47}$$

where the single-Chl contribution (electronic part) has been given in Eq. (11). The electric field strength $\boldsymbol{E}$ can be taken at an arbitrary point inside the PPC since the dimension of the latter is much smaller than the wavelength of the light field in the visible region.

Expanding the dipole operator, Eq. (11), with respect to the electronic states and concentrating on the Chl two-level model results in

$$\hat{\mu}_{\mathrm{PPC}} = \sum_m (\boldsymbol{d}_{eg}^{(m)} B_m^+ + \text{h.c.}) \;. \tag{48}$$

The multi-excitation expansion of the PPC dipole operator, Eq. (48) follows as

$$\hat{\mu}_{\mathrm{PPC}} = \sum_N \sum_{m \notin \{k\}_N} \sum_{\{k\}_N} (\boldsymbol{d}_{eg}^{(m)} |m, \{k\}_N\rangle\langle\{k\}_N| + \text{h.c.}) \;. \tag{49}$$

The dipole operator is responsible for transitions between neighboring N-excitation manifolds. Therefore, we can write

$$\hat{\mu}_{\mathrm{PPC}} = \sum_{N=0}^{N_{\mathrm{Chl}}-1} \hat{\mu}_{N+1,N} + \text{h.c.} \;, \tag{50}$$

where transitions between the manifold of N and $N+1$ electronic PPC excitations are explicitly indicated. The transition operator to the first excited manifold reads

$$\hat{\mu}_{1,0} = \sum_m \boldsymbol{d}_{eg}^{(m)} B_m^+ |0\rangle\langle 0| \equiv \sum_m \boldsymbol{d}_{eg}^{(m)} |m\rangle\langle 0| \tag{51}$$

and for the transition from the first to the second manifold we obtain

$$\hat{\mu}_{2,1} = \sum_{\substack{m,n \\ m \neq n}} \boldsymbol{d}_{eg}^{(m)} B_m^+ |n\rangle\langle n| \equiv \sum_{\substack{m,n \\ m \neq n}} \boldsymbol{d}_{eg}^{(m)} |m,n\rangle\langle n| \;. \tag{52}$$

Finally, we give the multi-exciton representation which is

$$\hat{\mu}_{\mathrm{PPC}} = \sum_{N=1}^{N_{\mathrm{Chl}}-1} \sum_{\alpha_{N+1},\beta_N} \boldsymbol{d}(\alpha_{N+1},\beta_N) |\alpha_{N+1}\rangle\langle\beta_N| + \text{h.c.} \;, \tag{53}$$

where the multi-exciton representation of the transition dipole operator reads

$$\boldsymbol{d}(\alpha_{N+1},\beta_N) = \sum_{m \notin \{n\}_N} \boldsymbol{d}_{eg}^{(m)} \sum_{\{n\}_N} C^*_{\alpha_{N+1}}(m, \{n\}_N) C_{\beta_N}(\{n\}_N) \;. \tag{54}$$

In particular, we get for the transition into the single-exciton manifold

$$\boldsymbol{d}(\alpha_1, 0) = \sum_m C^*_{\alpha_1}(m) \boldsymbol{d}_{eg}^{(m)} \;. \tag{55}$$

The expression for the transition from the single- to the two-exciton manifold reads

$$\boldsymbol{d}(\alpha_2,\beta_1)=\sum_{m,n}C^*_{\alpha_2}(m,n)\boldsymbol{d}^{(m)}_{eg}C_{\beta_1}(n)\;. \tag{56}$$

3.6. Nonadiabatic couplings

Nonadiabatic transitions are important for the description of the so-called *exciton annihilation* (see Section 5.3). The process incorporates the coupling of two Chls being close together and both excited in the S_1-state (state φ_e). Due to the mutual Coulomb interaction the excitation energy of one of the Chls can be used to transfer the other Chl molecule into a higher excited singlet state. A fast internal conversion back to the S_1-state results in a final state of a single excited Chl, i.e. one excited state (exciton) has been annihilated.

The internal conversion process can be related to nonadiabatic couplings which are obtained as the residual interactions among the eigenstates of the electronic Hamiltonian (see, for example [53]). They directly follow from the Born–Oppenheimer ansatz for the complete electron–vibrational wave function. Of main interest are intra-Chl nonadiabatic couplings which are due to the different single-Chl electronic states. We start with an expansion of the complete PPC Hamiltonian, Eq. (1) with respect to the electronic states ϕ_A and include the nonadiabatic coupling. It follows that

$$H_{\mathrm{PPC}}=\sum_{A,B}(\delta_{AB}\{T_{\mathrm{nuc}}+E^{(0)}_A(R)+V_{\mathrm{nuc\text{-}nuc}}(R)\}+\Theta_{AB}(R)+W_{AB}(R))|\phi_A(R)\rangle\langle\phi_B(R)|\;, \tag{57}$$

where the nonadiabatic coupling is introduced via electronic matrix elements of the nuclear kinetic energy part $\Theta_{AB}=\langle\phi_A(R)|T_{\mathrm{nuc}}|\phi_B(R)\rangle+\sum_{\mathrm{nuc}}1/M\ \langle\phi_A(R)|\hat{P}|\phi_B(R)\rangle\hat{P}$ (the summation is over all nuclear momentum operators). The quantity $W_{AB}(R)$ is the electronic matrix element of $1/2\sum_{m,n}V^{(\mathrm{el\text{-}el})}_{mn}$.

With this notation of the PPC Hamiltonian we can change to the site-representation, Section 3.3 or to the multi-exciton representation, Section 3.4. The EVC can be introduced in analogy to the procedure which will be given in the next section.

For a proper description of exciton annihilation and the step involving the internal conversion process it suffices to concentrate on intra-Chl processes. But it is necessary to use the three-level Chl model introduced in Appendix A. Specifying the general type of nonadiabatic coupling operator to the three-level Chl model we obtain

$$H_{\mathrm{na}}\equiv\sum_{A,B}\Theta_{AB}|\phi_A\rangle\langle\phi_B|=\sum_m(\Theta_{mf,ne}D^+_m+\mathrm{h.c.}) \tag{58}$$

with $D^+_m=|\varphi_{mf}\rangle\langle\varphi_{me}|$. The expression combines all nonadiabatic couplings at the various Chls resulting in transitions between the higher excited state $|\varphi_f\rangle$ and the first excited state $|\varphi_e\rangle$. For simplicity it will be assumed in the following that the operator of the nonadiabatic coupling, $\Theta_{mf,ne}$ is independent of the nuclear DOF. The additional consideration of H_{na} results in the fact that the number N of excited Chl in the PPC (introduced in Section 3.3) is no longer a good quantum number, transitions among different multi-exciton manifolds become possible.

4. Exciton–vibrational interaction

Having discussed the electronic problem for frozen configurations, R, of the Chl nuclei as well as the protein environment, a description which incorporates the nuclear dynamics will be given next. The related EVC is caused by a modulation of the electronic pigment energies as well as the inter-pigment Coulomb interactions and can be accounted for in the framework of potential energy surfaces.

Before discussing any details of handling the set $R = (\{R_m^{(\mathrm{intra})}\}, R_{\mathrm{protein}})$ of PPC nuclear DOF (i.e. intra-Chl and protein contributions, respectively, compare Section 3.1) we briefly comment on some general aspects of the introduction of PPC vibrational DOF. To this end we will concentrate on the electronic two-level model for the chromophores. (Respective formulas for the three-level model are collected in Appendix A.) For the following derivations we make use of Eq. (33). Neglecting nonadiabatic couplings the nuclear kinetic energy commutes with the projectors $\hat{P}_N$, Eq. (31), and we can write the complete PPC Hamiltonian (electron–vibrational Hamiltonian) as

$$H_{\mathrm{PPC}} = \sum_N H_{\mathrm{PPC}}^{(N)} \hat{P}_N \; . \tag{59}$$

From the N-excitation PPC Hamiltonian, Eq. (36), it follows that

$$H_{\mathrm{PPC}}^{(N)} = T_{\mathrm{nuc}} + E_0 + \mathscr{H}_{\mathrm{el}}^{(N)} + V_{\mathrm{nuc\text{-}nuc}} \; . \tag{60}$$

After some rearrangement we arrive at PES defined for the multiple electronic excitation states of the PPC. The ground state PES reads

$$U_0(R) = E_0(R) + V_{\mathrm{nuc\text{-}nuc}}(R) \tag{61}$$

and the related ground state vibrational Hamiltonian is given by

$$H_{\mathrm{PPC}}^{(0)} = T_{\mathrm{nuc}} + U_0(R) \; . \tag{62}$$

For the excited state contributions we get

$$H_{\mathrm{PPC}}^{(N)} = \sum_{\{k\}_N} \left([T_{\mathrm{nuc}} + U(\{k\}_N; R)] + \sum_{m \notin \{k\}_N} \sum_{n \in \{k\}_N} J_{mn} B_m^+ B_n \right) |\{k\}_N\rangle\langle\{k\}_N| \; . \tag{63}$$

with the PES

$$U(\{k\}_N; R) = U_0(R) + \sum_{m \in \{k\}_N} \varepsilon_m(eg; R) \; . \tag{64}$$

Although the PES are defined with respect to the state vectors in the site representation, they are of a very general type and define the basis for more specific expressions.

It is also possible to diagonalize $H_{\mathrm{PPC}}^{(N)}$, Eq. (63) for a given nuclear configuration to get

$$H_{\mathrm{PPC}}^{(N)} = \sum_{\alpha_N} (T_{\mathrm{nuc}} + U(\alpha_N; R)) |\alpha_N; R\rangle\langle\alpha_N; R| \; . \tag{65}$$

The $U(\alpha_N; R)$ are the PES related to the multi-exciton level with quantum number α_N. It is important to notice that besides the PES also the multi-exciton state-vectors depend on the actual nuclear configuration. This type of multi-exciton state is often called an *adiabatic* (multi)-exciton state (see, for example, [76]).

Up to now we did not specify whether the R are quantum mechanical operators or classical time-dependent coordinates. In general we expect that all high-frequency intra-Chl vibrations (part of the sets $R_m^{(\text{intra})}$) have to be described within quantum mechanics (Section 4.5). But for the low-frequency motions of the proteins (coordinates R_{protein}) a classical description may be possible. This is also true for the low-frequency intra-Chl vibrations. For simplicity in the following, we will not point out this explicitly but refer to protein motions only.

The various strategies with respect to the description of PPC nuclear DOFs are compiled in Fig. 4. (Note that this scheme is applicable to other problems of condensed phase dynamics as well.) Within a classical description of the PPC nuclear DOF, molecular dynamics simulations of all coordinates represents a powerful tool (see Section 4.1). It provides information about the fluctuations of the electronic quantities, the PES $U(\{m\}_N; R)$ together with the inter-pigment couplings $J_{mn}(R)$, or of the multi-exciton spectrum $E(\alpha_N; R)$. Alternatively to the direct determination of these fluctuations one can introduce certain stochastic processes characterizing the fluctuation of, e.g., $U(\{m\}_N; R)$ (see Section 4.2).

A consequent (nonequilibrium) quantum statistical description of the whole set of coordinates R is possible if one can map them on the set of collective coordinates $\{Q_\xi\}$. Collective coordinates which will be introduced in Section 4.3 replace the Cartesian nuclear coordinates to represent their motion by means of a set of decoupled harmonic oscillators. Such a treatment leads to the widely applied Brownian oscillator model [57]. The resulting type of interaction is usually called "exciton–phonon coupling". The term "exciton–phonon coupling" has its origin in the theory of excitons in organic solids (see, for example, Refs. [5,9]). There, the motion of the periodic lattice can be described by normal mode vibrations called phonons after quantization. In other words, the term phonon has a very special meaning which is not applicable to protein vibrations and therefore it will not be used in the following.

The description based on harmonic normal mode protein vibrations represents a frequently used model to deal with dissipative exciton motion in PPCs [63,76–82]. It leads to the introduction of a spectral density $\mathcal{J}(\omega)$ (or more precisely of a set of these functions, see Section 5.1.4) which carries the complete information on the EVC. The quantity $\mathcal{J}(\omega)$ is usually understood as the coupling-weighted density of states of the reservoir vibrations (protein vibrations in the present case), i.e. $\mathcal{J}(\omega) = \kappa(\omega)\mathcal{N}(\omega)$. Here, $\mathcal{N}(\omega)$ is the vibrational density of states and $\kappa(\omega)$ describes the respective coupling. Below, we will derive explicit microscopic expressions for the various parameters describing the EVC. The crucial point here will be the use of locally defined spectral densities which, however, incorporate the possibility of correlated vibrational motions at different sites.

The normal mode analysis of the PPC vibrations assumes a restriction to small-amplitude harmonic protein motions. If the vibrational motion of the proteins is characterized by large amplitudes, anharmonic couplings among the normal modes have to be taken into account. Up to now there is no direct experimental evidence for vibrational energy re-distribution in photosynthetic antenna systems. Vibrational anharmonicities are, however, of interest for the determination of the so-called pure dephasing rates [83–86]. In Section 4.4, we shortly discuss the separation of all nuclear DOF into a small subset of active co-ordinates R_{active} and a remaining set of passive coordinates R_{passive}. The former are understood as those DOF which are directly coupled to the motion as well as the creation and destruction of excitons. The set R_{passive} forms a new type of

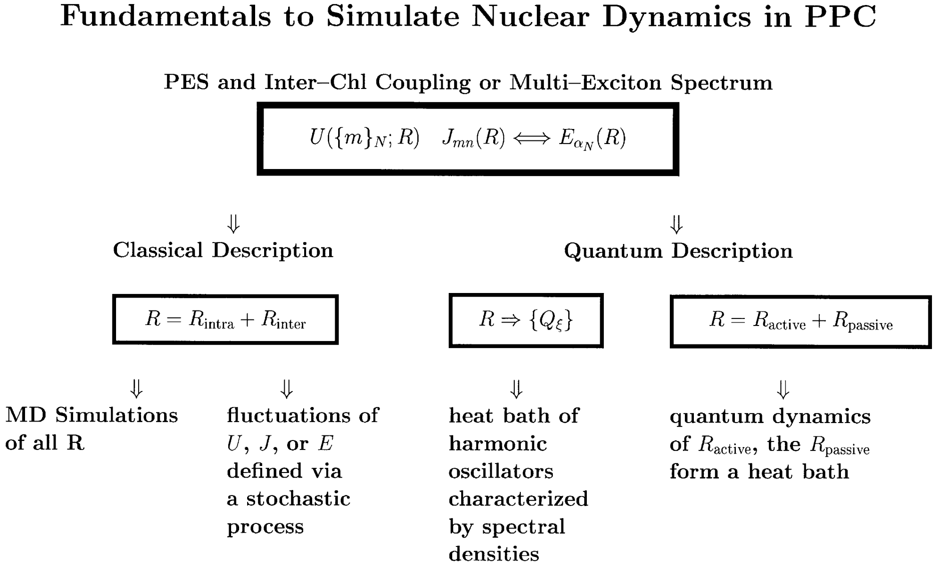

Fig. 4. Scheme for treating the coupled dynamics of electronic and nuclear DOF. The basis of the description is given by either the PES of localized PPC electronic excitations (and the vibrational modulation of the inter-Chl couplings) or the dependence of the multi-exciton energy levels on the various nuclear coordinates. If these quantities are available one can decide whether to carry out a classical or a quantum mechanical simulation. In the first case, it is possible to do MD simulations or to choose a more approximate description via simple stochastic models for nuclear vibrations and related fluctuations of PPC electronic energy levels. In the case of a quantum description one achieves a correct simulation of nuclear dynamics whenever all coordinates can be mapped to normal mode oscillators. Otherwise, a separation into a small set of active coordinates and a set of passive coordinates forming a heat bath would be advisable.

environment. Under certain conditions the correct quantum dynamics of the active coordinates can be described including any type of anharmonicity.

4.1. Molecular dynamics simulation

Molecular dynamics simulation represents a broadly applied technique to obtain insight into the structure and dynamics of molecules in solution, supramolecular complexes and the internal behavior of a large variety of macromolecules such as proteins. The approach is based on a description in terms of atoms or groups of atoms interacting via parameterized force fields and following Newton's equations of motion. In the case of biological macromolecules molecular dynamics simulations are of outstanding importance to get insight into their conformational changes and functionality, for instance. However, the complexity of these systems restricts the time-range which is accessible by present-day computer power to the sub-nanosecond region [46].

Classical dynamics simulation requires as an input interaction potentials among the various atoms or atomic groups as well as certain initial conditions [46,87,88]. The more difficult task, however, then consists in the combination of the classical simulations with Frenkel exciton motion. It touches the basic problem of how to incorporate into the description of classical nuclear dynamics on a single PES a nonadiabatic electronic quantum transition to a different PES. An approach widely used for small molecular systems in this respect is the so-called surface hopping method (see [53] and references therein). However, nothing has been done along these lines in the context of light-harvesting PPCs. On the other hand, within relaxation theory the influence of the environment can be described by means of time correlation functions, e.g. of the excitation energy gap (cf. Section 5). This type of correlation function is readily obtained from molecular dynamics simulations as has been demonstrated for the case of electron transfer in the photosynthetic reaction center in Refs. [89,90]. On the other hand, it would be also helpful to have data on the classical dynamics of PPCs in their ground state. Based on this knowledge one could try to construct the density of states $\mathcal{N}(\omega)$ or even the spectral density $\mathcal{J}(\omega)$ determining multi-exciton relaxation (see the introductory part of this section).

4.2. Stochastic models

If one is not interested in details of the coupling of the electronic excitations to PPC vibrations it is possible to replace the vibrational modulation of the chromophore electronic states (and of the Coulomb-interaction) by a stochastic process. Such a treatment has a long tradition in the field of Frenkel exciton theory and is well-known as the *Haken–Strobl–Reineker* model [91,92]. Up to now the stochastic description of the EVC has been restricted to the single-excited electronic state [8,63,93,95]. For the case of photosynthetic antenna systems it assumes the following type of PPC Hamiltonian (compare Eq. (37) and Ref. [95]):

$$H^{(1)}_{\mathrm{PPC}} = E_0 + \sum_{m,n} [\delta_{mn}(\varepsilon_m(eg) + \Delta\varepsilon_m(eg)(t)) + (1-\delta_{mn})(J_{mn} + \Delta J_{mn}(t))]|m\rangle\langle n| \,. \tag{66}$$

The $\Delta\varepsilon_m(eg)(t)$ and $\Delta J_{mn}(t)$ represent certain stochastic processes. They have to be defined via a hierarchy of related correlation functions. In the case of a Gaussian process it is sufficient to fix the lowest-order correlation functions

$$C^{(\varepsilon)}_{mn}(t-\bar{t}) = \langle \Delta\varepsilon_m(eg;t)\Delta\varepsilon_n(eg;\bar{t})\rangle_{\mathrm{stoch}} \tag{67}$$

and

$$C^{(J)}_{kl,mn}(t-\bar{t}) = \langle \Delta J_{kl}(t)\Delta J_{mn}(\bar{t})\rangle_{\mathrm{stoch}} \tag{68}$$

as well as the cross-correlation function

$$C^{(\varepsilon,J)}_{k,mn}(t-\bar{t}) = \langle \Delta\varepsilon_k(eg,t)\Delta J_{mn}(\bar{t})\rangle_{\mathrm{stoch}} \,, \tag{69}$$

where $\langle \dots \rangle_{\mathrm{stoch}}$ denotes the averaging with respect to the stochastic process. A typical choice for the correlation functions would be [63]

$$C^{(\varepsilon)}_{mn}(t-\bar{t}) = \delta_{mn}\langle \Delta\varepsilon_n(eg;t)\Delta\varepsilon_n(eg;\bar{t})\rangle_{\mathrm{stoch}} \,, \tag{70}$$

$$C^{(J)}_{kl,mn}(t-\bar{t}) = (1-\delta_{kl})[\delta_{lm}\delta_{kn}\langle \Delta J_{kl}(t)\Delta J_{lk}(\bar{t})\rangle_{\mathrm{stoch}} + \delta_{km}\delta_{ln}\langle \Delta J_{kl}(t)\Delta J_{kl}(\bar{t})\rangle_{\mathrm{stoch}}] \tag{71}$$

and $C^{(\varepsilon,J)}_{k,mn}(t-\bar{t}) = 0$. The time-dependence of the correlation function has to be assumed separately and gives the concrete type of process, e.g., the Gaussian process (see, for example, [8]).

An alternative to the Gaussian process is given by the dichotomic process. Here the fluctuating quantity $\eta(t)$ (provided it has been properly normalized) jumps randomly between 1 and -1

[93–96] and we have $\langle \eta(t)\eta \rangle_{\mathrm{stoch}} = \exp(-\nu t)$. Despite the rather simple structure of the correlation function it is a major advantage of the dichotomous noise that finite correlation times can be considered.

4.3. Analysis based on PPC normal mode vibrations

The introduction of PPC normal mode vibrations gives a common description of all those vibrational DOF of the PPC which carry out small-amplitude oscillations. All other types of motions related to, e.g., large conformational changes are neglected (or considered as static disorder provided they are slow enough). Nevertheless, for the actual status of the experiments this model allows for an excellent simulation of exciton dissipation on a sub-picosecond time scale. The description is based on microscopically defined coupling expressions, but enables one to condense them into certain frequency-dependent functions, the spectral densities. This circumstance makes the approach of particular interest for the present state of describing PPC. Since computations of the microscopic expressions for the EVC do not exist, it is a widely used alternative to make a reasonable ansatz for the spectral densities and to compare the results with measured data.

A correct description of (multi-) exciton relaxation relies on the use of the electronic (excitonic) eigenstates (see Section 5). Below, we will discuss an adequate formulation of the multi-exciton vibrational interaction Hamiltonian. It is based, however, on an assumption about the coupling of the local Chl-excitations as well as their mutual Coulomb-interaction to the PPC normal mode vibrations. Appendix B is devoted to a detailed description of this coupling. Here, we will use the respective expressions to derive the multi-exciton vibrational coupling. We use the transformation Eq. (39) for the two-level Chl model (or Eq. (A.13) for the three-level Chl model) and obtain the representation of the complete PPC Hamiltonian in terms of delocalized exciton states. Splitting off the PPC ground state energy E_0 one can write (instead of Eq. (B.23))

$$H^{(N)}_{\mathrm{PPC}} = E_0 + \mathscr{H}^{(N)}_{\mathrm{el}}(R_0) + H^{(N)}_{\mathrm{exc-vib}} + H_{\mathrm{vib}} \,. \tag{72}$$

The pure excitonic part $\mathscr{H}^{(N)}_{\mathrm{el}}(R_0)$ has been given in Eq. (36); it is specified here to the nuclear configuration R_0 corresponding to the minimum of the PPC ground state PES (see Appendix B). The Hamiltonian H_{vib}, Eq. (B.7), which is responsible for the free motion of the reservoir DOF is that of a set of uncoupled harmonic oscillators. The multi-exciton vibrational coupling reads

$$H^{(N)}_{\mathrm{exc-vib}} = \sum_{\alpha_N,\,\beta_N} \sum_{\xi} \hbar\omega_\xi g_\xi(\alpha_N,\beta_N) Q_\xi |\alpha_N\rangle\langle\beta_N| \,. \tag{73}$$

Here, the Q_ξ denote dimensionless normal mode coordinates (cf. Eq. (B.4)). The multi-exciton–vibrational coupling constants are obtained by introducing the exciton representation of Eq. (B.24) as has been done in Appendix B:

$$g_\xi(\alpha_N,\beta_N) = \sum_{\{k\}_N} \Bigg(C^*_{\alpha_N}(\{k\}_N) g_\xi(\{k\}_N) C_{\beta_N}(\{k\}_N) + \sum_{m\notin\{k\}_N} \sum_{n\in\{k\}_N} C^*_{\alpha_N}(\{k; n\to m\}_N) \tilde{g}_\xi(m,n) C_{\beta_N}(\{k\}_N) \Bigg) \,. \tag{74}$$

The $g_\xi(\{k\}_N)$ have been defined in Eq. (B.18) and are related to the vibrational modulation of the electronic Chl excitations. The $\tilde{g}_\xi(m,n)$, Eq. (B.22) follow from the modulation of the mutual Chl Coulomb coupling. The symbol $\{k; n \to m\}_N$ indicates that in the set $\{k\}_N$ the particular Chl index n has been replaced by m. For completeness we present the EVC constant for the single- and two-exciton manifold. For the former we get

$$g_\xi(\alpha_1, \beta_1) = \sum_k \left(C^*_{\alpha_1}(k) g_\xi(k) + \sum_{m \neq k} C^*_{\alpha_1}(m) \tilde{g}_\xi(m,k) \right) C_{\beta_1}(k) \,. \tag{75}$$

The two-exciton–vibrational coupling constant reads

$$g_\xi(\alpha_2, \beta_2) = \sum_{k,l,k \neq l} \left(C^*_{\alpha_2}(k,l) g_\xi(k,l) + \sum_{m \neq k,l} [C^*_{\alpha_2}(k,m)\tilde{g}_\xi(m,l) + C^*_{\alpha_2}(m,l)\tilde{g}_\xi(k,m)] \right) C_{\beta_2}(k,l) \,. \tag{76}$$

Finally, using all the preceding specifications of the contributions to $H^{(N)}_{\text{PPC}}$, Eq. (72), we obtain the exciton representation of the N-exciton part of the PPC Hamiltonian. Although very complex in its definition it has the simple form

$$H^{(N)}_{\text{PPC}} = \sum_N \sum_{\alpha_N, \beta_N} \left(\delta_{\alpha_N, \beta_N} \{ E_{\alpha_N} + H_{\text{vib}} \} + \sum_\xi \hbar\omega_\xi g_\xi(\alpha_N, \beta_N) Q_\xi \right) |\alpha_N\rangle\langle\beta_N| \,. \tag{77}$$

The vibrational Hamiltonian H_{vib} has been included in the multi-exciton expansion demonstrating that in the present model all relaxation processes will take place in a given manifold of the N-exciton state.

Next, we present a notation of the EVC which is appropriate for the description of the exciton motion in terms of dissipative quantum dynamics (Section 5). We consider the electronic (excitonic) DOF as those forming the active system S whereas the vibrational DOF define the reservoir R. According to this separation we identify the multi-exciton vibrational coupling with the system–reservoir coupling of dissipative quantum dynamics [53]

$$\sum_N H^{(N)}_{\text{exc-vib}} \hat{P}_N \equiv H_{\text{S-R}} = \sum_u \hat{K}_u \hat{\Phi}_u \,. \tag{78}$$

The separation of $H_{\text{S-R}}$ has to be understood in such a manner that the operators $\hat{K}_u$ ($\hat{\Phi}_u$) act exclusively in the state space of the system (the reservoir) DOF. According to Eq. (73) we can deduce the system parts of $H_{\text{S-R}}$ as (note that it is not hermitian)

$$\hat{K}_u = |\alpha_N\rangle\langle\beta_N| \,, \tag{79}$$

i.e. $u \equiv (\alpha_N, \beta_N)$. For the reservoir part we obtain

$$\hat{\Phi}_u = \hbar \sum_\xi \omega_\xi g_\xi(\alpha_N, \beta_N) Q_\xi \,. \tag{80}$$

In passing we note that if one incorporates a nonlinear coupling to the vibrational DOF the reservoir part of the systems–reservoir coupling becomes

$$\hat{\Phi}_u = \hbar \sum_\xi \omega_\xi (g_\xi(\alpha_N, \beta_N) Q_\xi + g^{(2)}_\xi(\alpha_N, \beta_N) Q^2_\xi) \,. \tag{81}$$

Since in the second-order contribution $\sim g_\xi^{(2)}(\alpha_N, \beta_N)$ it is difficult to discriminate between diagonal and off-diagonal contributions with respect to the mode index ξ we will restrict ourselves to the diagonal terms.

4.3.1. Excitonic potential energy surfaces

An intuitive notation of $H_{\mathrm{PPC}}^{(N)}$, Eq. (77), leading to a certain type of PES is obtained if one splits up the coupling constants $g_\xi(\alpha_N, \beta_N)$ into its diagonal and off-diagonal elements. The diagonal elements can be used to define PES. To this end, we take the potential energy part $\sum_\xi \hbar\omega_\xi Q_\xi^2/4$ of H_{vib} and combine it with the term $\propto Q_\xi$ of Eq. (77) to define the (shifted) *excitonic* PES (see the scheme in Fig. 5):

$$U(\alpha_N, Q) = E_{\alpha_N} - \sum_\xi \hbar\omega_\xi g_\xi^2(\alpha_N, \alpha_N) + \sum_\xi \frac{\hbar\omega_\xi}{4}(Q_\xi + 2g_\xi(\alpha_N, \alpha_N))^2 \ . \tag{82}$$

Then, the multi-exciton representation of the PPC Hamiltonian is obtained as

$$H_{\mathrm{PPC}}^{(N)} = \sum_N \sum_{\alpha_N, \beta_N} \left(\delta_{\alpha_N, \beta_N} \{T_{\mathrm{vib}} + U(\alpha_N, Q)\} + (1 - \delta_{\alpha_N, \beta_N}) \sum_\xi \hbar\omega_\xi g_\xi(\alpha_N, \beta_N) Q_\xi \right) |\alpha_N\rangle\langle\beta_N| \ . \tag{83}$$

Next, we clarify the type of the states which are of zeroth-order with respect to the off-diagonal elements of the EVC matrix. Neglecting the second contribution in the PPC Hamiltonian one easily obtains the eigenstates as

$$|\Psi_{\alpha_N}^{(0)}\rangle = |\alpha_N\rangle \prod_\xi \exp(g_\xi(\alpha_N, \alpha_N) C_\xi - \mathrm{h.c.}) |\mathcal{N}_\xi\rangle \ . \tag{84}$$

The expression describes the shift of every normal mode oscillator upon the excitation of the multi-exciton state $|\alpha_N\rangle$. The amount of this shift is determined by $g_\xi(\alpha_N, \alpha_N)$. It is related to the nonshifted normal mode oscillator states $|\mathcal{N}_\xi\rangle$ with $\mathcal{N}_\xi$ excited vibrational quanta. For the case of the single-exciton states we give a notation in terms of local Chl excitations,

$$|\Psi_{\alpha_1}^{(0)}\rangle = \sum_m C_{\alpha_1}(m) |m\rangle \prod_\xi \exp(g_\xi(\alpha_1, \alpha_1) C_\xi - \mathrm{h.c.}) |\mathcal{N}_\xi\rangle \ . \tag{85}$$

This type of exciton–vibrational state is usually called Davydov ansatz since it has been widely used (in a time-dependent version) by Davydov to describe soliton motion in molecular chains [97]. It is well known that this type of state if understood as an ansatz for a variational determination of the respective energy (with $C(m)$ and g_ξ to be determined) does not give the best result for the ground state energy of the so-called excitonic polaron. Of a more general type would be an ansatz where the g_ξ in the exponent of the shift operator depend on the molecule index m. Then, the state incorporates a superposition of vibrational displacements which depends on the different sites (for a recent application to exciton localization in the LH2 see [76,98]). In contrast, the ansatz in Eq. (85) only contains displacements of vibrational coordinates which are valid for all sites m. Nevertheless, the excitonic PES introduced so far correspond to a certain approximative description of the excitonic polaron. And, a natural generalization to multi-excitonic polarons can be directly deduced from Eq. (84). Including the off-diagonal multi-exciton–vibrational coupling within an approximate treatment one can expect an improvement of the Davydov-type state.

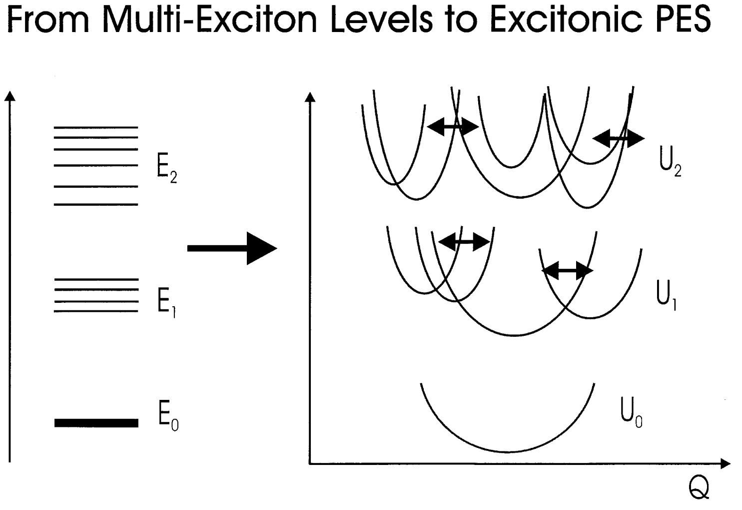

Fig. 5. Comparison of multi-exciton levels (left) and excitonic PES (right). Every multi-exciton level of a particular manifold is represented by an excitonic PES. (The horizontal arrows indicate the residual coupling among the PES via the part of the EVC being off-diagonal with respect to the multi-exciton quantum numbers.)

4.4. *Active and passive vibrational coordinates*

In the preceding section we chose a description based on normal mode coordinates $\{Q_\xi\}$ comprising all types of PPC vibrations. However, experimental evidence has been obtained for vibrational coherences [99] indicating that there might exist a reduced set of vibrational DOF which couples strongly to the electronic PPC excitations. In the context of dissipative quantum dynamics [53] this type of vibrational coordinates is usually called active coordinates. They will be incorporated into the active system and we will label this subset by $s = \{s_j\}$. The remaining set of passive coordinates is denoted as $Z = \{Z_\xi\}$. Along theses passive coordinates the vertical excitation energy from the ground state to a (multiple) excited states does not change significantly. Using the representation with respect to the multiple excited PPC states the respective PES $U(\{k\}_N; R)$, Eq. (64), splits up as $U(\{k\}_N; s) + U(Z)$. Independent of the excited electronic state the coordinates Z belong to a single PES which define the reservoir Hamiltonian H_R. But there may exist an electronic state-dependent coupling between active and passive coordinates leading in the present case the system–reservoir interaction of the form

$$H_\text{S-R} = \sum_N \mathscr{H}^{(N)}_\text{S-R} , \tag{86}$$

with

$$\mathscr{H}^{(N)}_\text{S-R} = \sum_{\{k\}_N} W_{\{k\}_N}(s, Z)|\{k\}_N\rangle\langle\{k\}_N| , \tag{87}$$

where $W_{\{k\}_N}(s,Z)$ is the respective coupling matrix element. Calculations for the coupled dissipative quantum dynamics of the electronic DOF and a set of active coordinates s comprising not more than two coordinates have been carried out in Refs. [12,14,100,101]. Since wave packet dynamics related to the active coordinates are incorporated, the description is well suited to simulate vibrational coherences observed in ultrafast optical spectroscopy.

4.5. High-frequency intramolecular chlorophyll vibrations

In Section 2.2, we referred to experimental data on intra-Chl vibrations. Here we focus on the high-frequency vibrations for which the vibrational quanta are so large that a separate treatment is advisable. This is also suggested by the fact that distinct vibrational progressions are observed in the experiments. This can be accounted for by combining the high-frequency modes with the electronic spectrum of the Chl molecules. The related stationary Schrödinger equation reads (see Eqs. (4) and (2))

$$\begin{aligned}&(H_m^{(\mathrm{el})}(R) + T_{\mathrm{nuc}} + V_{\mathrm{nuc\text{-}nuc}}(R_m^{(\mathrm{intra})}))\varphi_{ma}(R)\chi_{ma\nu}(R_m^{(\mathrm{intra})})\\ &\quad = (\varepsilon_{ma} + \hbar\omega_{ma\nu})\varphi_{ma}(R)\chi_{ma\nu}(R_m^{(\mathrm{intra})}) . \qquad (88)\end{aligned}$$

As stated earlier the electronic energies ε_{ma} are defined such that they already contain all types of vibrational zero-point energies. Eventually, nonadiabatic couplings have to be considered, which will be discussed in the following section. Eq. (88) is based on the assumption that there is no considerable coupling of a single set $R_m^{(\mathrm{intra})}$ of intramolecular coordinates to other types of nuclear DOF. We can use the eigenstates of the stationary Schrödinger equation to expand the PPC Hamiltonian with respect to these electron–vibrational states. All formulas given so far remain valid with the exception that one has to replace the electronic quantum numbers a (b, …) by the electron–vibrational quantum numbers $a\nu$. Furthermore, any electronic matrix element $A_{ma,mb}$ has to be multiplied by the Franck–Condon factor $\langle\chi_{ma\mu}|\chi_{mb\nu}\rangle$.

In the energy level scheme used so far the ground state level φ_g, the first excited level φ_e, and the higher excited level φ_f are supplemented by high-frequency vibrational quanta $\hbar\omega_{ma\nu}$. Thus the new energy spectrum ensures, for instance, that there exist a transition from φ_e into the vibrational manifold of the level φ_f which is nearly equal in energy to the transition from level φ_g to φ_e. In particular, this leads to a near degeneracy of the excitation into the higher excited state φ_{mf} with two excitations into φ_{me} and φ_{ne}. This possibility was the assumption for the multi-exciton representation for the three-level Chl model given in Appendix A.

5. Dissipative exciton dynamics

At the center of optical experiments on light-harvesting PPCs are the electronic transitions and the related exciton dynamics as it is induced by the interaction with the external laser field. Nevertheless, EVC as discussed in the previous section is of great importance for the detailed understanding of optical line shapes. Also it is fundamental for the energy funneling towards the reaction center which comes along with energy dissipation into the protein environment. Hence, any theoretical simulation has to be aimed at computing electronic expectation values related to the measured quantities. The vibrational DOF which couple weakly to the electronic (multi-excitonic) DOF can be considered to form a thermal reservoir. If the coupling is stronger, for example, for some selected modes (see Section 4.4), a description is necessary which incorporates the nonequilibrium dynamics of these modes.

In the following, we will present different approaches to the description of dissipative exciton dynamics. First, we shortly recall the well-established treatment of an open quantum system by means of the quantum master equation (QME) [53,102,103]. It assumes an unequivocal separation of the whole system into a small subsystem of active DOF and an environment. Such a separation is obvious in the case of weak or intermediate EVC strength where all vibrational DOF can be understood as forming a thermal environment (cf. Section 4.3). Here the standard QME can be used to study exciton transport and relaxation. In order to treat cases where the coupling of excitons to vibrational DOF becomes so strong that a perturbational treatment is impossible, we present an approach known as Liouville space pathway technique. It establishes generalized master equations (GME) and corresponds to a perturbation theory, for example with respect to inter-Chl Coulomb coupling. An alternative which goes back to the QME description is achieved if one can split off from the whole set of vibrational DOF a small subset of active coordinates coupling strongly to the exciton motion (cf. Section 4.4). Those active coordinates are put together with the electronic DOS to form the enlarged active system. This treatment is advisable, for example, if one wants to describe coherent vibrational motions which are observed, e.g., at very low temperatures [99].

It is important to note that all approaches discussed in the following have their background in the theory of open quantum systems [53]. The basics of this theory with the density matrix in its center were established at the end of the 1950s. But during the late 1970s and early 1980s a number of contributions to the transport properties of excitons in molecular systems have been given (see, e.g., [8,9,104–107]). The new aspects which have been worked out, in particular during the study of PPCs in the last decade, are the following. (i) In order to simulate the results from ultrafast spectroscopic measurements it is of great importance to generate the *time-dependence* of the density matrix in the course of numerical calculations. (ii) Since it is of interest to have a realistic description of exciton relaxation, improved models of EVC had to be used. (iii) In contrast to the pure single-exciton theories, the modern approach is based on a multi-exciton formulation to allow for simulation of nonlinear optical spectroscopy.

5.1. The reduced density operator approach

5.1.1. The quantum master equation

In typical experiments the interaction with the external electromagnetic fields basically influences the electronic DOF of the PPCs. Therefore, the observables to be calculated in numerical simulations are matrix elements defined via electronic wave functions. As a consequence it is suitable to introduce a quantity which carries the statistical information reduced to the electronic DOF only. This is achieved if one utilizes the well-established concept of the reduced statistical operator (RSO). If $\hat{W}(t)$ denotes the statistical operator of the complete exciton–vibrational system of the PPC, the RSO is obtained by taking its trace with respect to the subsystem of vibrational DOF:

$$\hat{\rho}(t) = \mathrm{tr}_{\mathrm{vib}}\{\hat{W}(t)\} . \qquad (89)$$

According to this definition the RSO describes the time-dependence of the electronic DOF under the influence of the vibrational DOF leading to energy dissipation and wave function dephasing. This statement is general and does not require weak EVC. And indeed, it is well known that an exact equation – the Nakajima–Zwanzig equation – can be derived which determines the RSO [108]. Unfortunately, any specific computation is restricted to a low-order version of this equation such as, for example, the second Born approximation. Therefore, any practical use of the QME has to be based on a weak EVC in the present case.

According to general relaxation theory the following separation of the complete PPC Hamiltonian is performed:

$$H_{\mathrm{PPC}} = H_{\mathrm{S}} + H_{\mathrm{S\text{-}R}} + H_{\mathrm{R}} \ . \tag{90}$$

First, we have an active system with Hamiltonian the H_{S}. For the present application it contains the electronic DOF of the PPC, which can be supplemented by a small set of vibrational DOF as discussed in Section 4.4. The reservoir Hamiltonian is denoted H_{R} and governs the motion of the nuclear DOF of the PPC. The coupling of the latter to the active system is contained in the interaction part, $H_{\mathrm{S\text{-}R}}$. (Various specifications of these operators will be given below.) The necessary combination of perturbation theory with respect to $H_{\mathrm{S\text{-}R}}$ and the reduction procedure to the state space of the active DOF is achieved by introducing a projection superoperator $\mathscr{P}$ [108] which acts on some operator $\hat{A}$ of the total system according to

$$\mathscr{P}\hat{A} = \hat{R}_{\mathrm{eq}}\mathrm{tr}_{\mathrm{R}}\{\hat{A}\} \ . \tag{91}$$

Here $\hat{R}_{\mathrm{eq}}$ is the equilibrium statistical operator of the reservoir and tr_{R} denotes the trace with respect to the reservoir DOF. If applied to the complete statistical operator $\hat{W}$ (or any other operator acting in the product state space of the system and reservoir states) the projector $\mathscr{P}$ leads to a factorization of $\hat{W}$ into a part which is exclusively defined in the system state space, i.e. in the present case to the RSO $\hat{\rho}$. The other part is fixed by $\hat{R}_{\mathrm{eq}}$ and acts in the reservoir state space. According to this property of $\mathscr{P}$ it enables us to derive exact equations of motion for $\hat{\rho}$ where the reservoir enters via its equilibrium properties.

To derive equations of motion for $\hat{\rho}$ which contain the effect of $H_{\mathrm{S\text{-}R}}$ up to second order we note that the Liouville–von Neumann equation for the complete statistical operator $\hat{W}$ written in the interaction representation (with the interaction part $H_{\mathrm{S\text{-}R}}$ and related Liouville superoperator $\mathscr{L}_{\mathrm{S\text{-}R}}$) reads

$$\frac{\partial}{\partial t}\hat{W}^{(\mathrm{I})}(t) = -\mathrm{i}\mathscr{L}^{(\mathrm{I})}_{\mathrm{S\text{-}R}}(t)\hat{W}^{(\mathrm{I})}(t) \ . \tag{92}$$

Here, $\hat{W}^{(\mathrm{I})}(t) = U_0^{\dagger}(t-t_0)\hat{W}(t)U_0(t-t_0)$ with the interaction-free time evolution operator $U_0(t-t_0) = \exp\{-\mathrm{i}(H_{\mathrm{S}} + H_{\mathrm{R}})(t-t_0)\}$ and the interaction operator $H^{(\mathrm{I})}_{\mathrm{S\text{-}R}}(t) = U_0^{\dagger}(t-t_0) \times H_{\mathrm{S\text{-}R}}U_0(t-t_0)$. Next we introduce the orthogonal complement, $\mathscr{Q}$, with $\mathscr{P} + \mathscr{Q} = 1$, which projects onto the irrelevant part of the statistical operator. The equation of motion for both parts are easily found to be

$$\frac{\partial}{\partial t}\mathscr{P}\hat{W}^{(I)} = -\mathrm{i}\mathscr{P}\mathscr{L}^{(\mathrm{I})}_{\mathrm{S\text{-}R}}(t)(\mathscr{P} + \mathscr{Q})\hat{W}^{(\mathrm{I})}(t) \tag{93}$$

and

$$\frac{\partial}{\partial t}\mathcal{Q}\hat{W}^{(I)} = -\mathrm{i}\mathcal{Q}\mathcal{L}^{(\mathrm{I})}_{\mathrm{S\text{-}R}}(t)(\mathcal{P} + \mathcal{Q})\hat{W}^{(\mathrm{I})}(t) \ . \tag{94}$$

Solving Eq. (94) and inserting the result into the equation for $\mathcal{P}\hat{W}^{(\mathrm{I})}$, a closed equation for the RSO is obtained (Nakajima–Zwanzig equation). We retain the second-order approximation with respect to $H_{\mathrm{S\text{-}R}}$ and neglect initial correlations by setting $\mathcal{Q}\hat{W}^{(\mathrm{I})}(t_0) = 0$. It results the QME in its non-Markovian version. Although it would be necessary to investigate systematically the importance of non-Markovian effects with respect to the EVC in PPCs we will take here as a reference case the Markov-approximation. We will return to the issue of non-Markovian dynamics in Section 9.2.4. Fortunately, the condensed-phase environment provided by the intramolecular chlorophyll vibrations or the motions of the protein scaffold are characterized by correlation functions which can be reasonable approximated as decaying rather rapidly on the time scale given by the dissipative dynamics of the relevant system. Concerning the LHA's three-pulse photon echo experiments on LH2 [109] as well as numerical simulation for the reaction center Warshel and Parson [110] suggest correlation times to be typically below 100 fs in photosynthetic systems which shows that the Markov approximation is of reasonable quality.

For the following considerations, the factorization ansatz for the system–reservoir interaction Hamiltonian (see Eqs. (78))

$$H_{\mathrm{S\text{-}R}} = \sum_u K_u \Phi_u \tag{95}$$

will provide sufficient flexibility. Here, K_u and Φ_u are operators in the system and reservoir space, respectively. Accordingly the non-Markovian QME for exciton dynamics reads

$$\frac{\partial}{\partial t}\hat{\rho} = -\frac{\mathrm{i}}{\hbar}[H_{\mathrm{S}}, \hat{\rho}] - \mathcal{R}[\hat{\rho}](t) \ . \tag{96}$$

The dissipative part becomes

$$\mathcal{R}[\hat{\rho}](t) = \sum_{u,v} \int_0^{t-t_0} \mathrm{d}\tau \, (C_{uv}(\tau)[K_u, U_{\mathrm{S}}(\tau)K_v\hat{\rho}(t-\tau)U^{\dagger}_{\mathrm{S}}(\tau)] \\ - C_{vu}(-\tau)[K_u, U_{\mathrm{S}}(\tau)\hat{\rho}(t-\tau)K_v U^{\dagger}_{\mathrm{S}}(\tau)]) \ . \tag{97}$$

Here the reservoir correlation function

$$C_{uv}(t) = \frac{1}{\hbar^2}\mathrm{tr}_{\mathrm{R}}\{\hat{R}_{\mathrm{eq}}\Phi^{(\mathrm{I})}_u(t)\Phi^{(\mathrm{I})}_v(0)\} \tag{98}$$

has been introduced. It is defined by the reservoir part Φ_u of the system reservoir coupling, Eq. (95), in the interaction representation. (If existing, the factorized part $(\mathrm{tr}_{\mathrm{R}}\{\hat{R}_{\mathrm{eq}}\Phi^{(\mathrm{I})}_u(0)\}/\hbar)^2$ of the correlation function has to be subtracted [53]). The correlation function can be related to a special type of dissipation–fluctuation theorem. It states how energy dissipation in the reservoir is determined by reservoir equilibrium fluctuations (see, for example [53]). Therefore, it is not surprising that $C_{uv}(t)$ mainly determines the dissipative part of the QME.

If the Markov approximation is made (for $\hat{\rho}$ taken in the interaction representation with respect to $H_{\mathrm{S\text{-}R}}$) the dissipative part is governed by the time-local relaxation superoperator

$$\mathscr{R}\rho(t) = \sum_u [K_u, \Lambda_u \hat{\rho}(t) - \hat{\rho}(t)\Lambda_u^\dagger] , \tag{99}$$

which contains the operator

$$\Lambda_u = \sum_v \int_0^\infty \mathrm{d}t \, C_{uv}(t) K_v^{(\mathrm{I})}(-t) . \tag{100}$$

In the following, we will use the more compact notation for the QME:

$$\frac{\partial}{\partial t}\hat{\rho} = -\mathrm{i}\mathscr{L}_{\mathrm{eff}}\hat{\rho} , \tag{101}$$

where the effective Liouville superoperator reads

$$\mathscr{L}_{\mathrm{eff}} = \mathscr{L}_{\mathrm{S}} - \mathrm{i}\mathscr{R} \tag{102}$$

and $\mathscr{L}_{\mathrm{S}}$ abbreviates the commutator with $H_{\mathrm{S}}/\hbar$. Eq. (101) together with Eq. (99) is a central result of general relaxation theory (see, e.g. [53]) which has to be specified to the case of LHA's next.

5.1.2. The spectral density

Before changing to the multi-exciton representation of the QME we shortly comment on the correlation function, Eq. (98) and its relation to the so-called spectral density. In fact, there appears a fundamental specification for the reservoir DOF if the QME, Eq. (96) or Eq. (101), is used. The particular treatment of the coupling between the active system and the environment results in an equilibrium description of the reservoir (neglecting any coupling to the active system). The reservoir state is characterized by the equilibrium statistical operator $\hat{R}_{\mathrm{eq}}$, and $C_{uv}(t)$ is the correlation function of the reservoir operators $\Phi_u^{(\mathrm{I})}(t)$ in thermal equilibrium. The diagonal part $C_{uu}(0)$ (at zero time) gives the expectation value of Φ_u^2. Under certain specifications for Φ_u (see below), $C_{uu}(0)$ can be related to the mean-square deviation of the reservoir coordinates from its equilibrium position (at finite temperature or at $T = 0$).

Besides the discussed quantum statistical description of the reservoir correlation function a simulation in terms of classical distribution functions is also possible as mentioned in Section 4.1. What has been not specified by the approach is the concrete type of PES governing the motion of the reservoir DOF. If the motion is mainly anharmonic (large-amplitude motion) and different DOF are strongly coupled the correct quantum statistical description and in particular the study of the low-temperature region would become difficult. However, if the reservoir DOF carry out a small-amplitude motion one can introduce a normal mode representation (compare Section 4.3 and Appendix B).

We will discuss here the resulting general structure of the correlation function assuming the existence of a single-coupling expression $\Phi = \sum_\xi \hbar\omega_\xi g_\xi Q_\xi$ similar to Eq. (80) (the Q_ξ are dimensionless normal mode coordinates). The mapping of the reservoir dynamics on the equilibrium state of a large set of decoupled harmonic oscillators makes it easy to compute the correlation function. Incorporating a Fourier transform we get for the frequency-dependent correlation function ($n(\omega)$ is the Bose–Einstein distribution)

$$C(\omega) = 2\pi\omega^2(1 + n(\omega))(\mathcal{J}(\omega) - \mathcal{J}(-\omega)) , \tag{103}$$

where we introduced the *spectral density*

$$\mathcal{J}(\omega) = \sum_\xi g_\xi^2 \delta(\omega - \omega_\xi) . \tag{104}$$

Via a simple frequency integration $\mathcal{J}(\omega)$ can be related to the quantity

$$S = \int d\omega\, \mathcal{J}(\omega) = \sum_\xi g_\xi^2 \tag{105}$$

which is known as the Huang–Rhys factor. The spectral density can be understood as the coupling constant weighted density of states of the normal mode oscillators. The latter quantity is given as

$$\mathcal{N}(\omega) = \sum_\xi \delta(\omega - \omega_\xi) . \tag{106}$$

If it is possible to replace g_ξ^2 by $\kappa(\omega_\xi)$, i.e. the mode index dependence is exclusively given via the normal mode frequencies ω_ξ, the spectral density indeed is obtained as $\mathcal{N}(\omega)$ weighted by the coupling constant distribution $\kappa(\omega)$.

The above given expressions demonstrate how one profits from the mapping of the reservoir DOF on harmonic oscillators. If their number is large enough one can consider the spectral density as a continuous function of the frequency. Hence, the large set of DOF has been replaced by a single function for which different analytical models exist (see below). Alternatively, $\mathcal{J}(\omega)$ can be obtained from fitting of experimental data [77,111], or from classical molecular dynamics simulations which has been done, for instance, for the reaction center [90].

This is the basic concept we will follow below to characterize the dissipative influence of the protein environment on the exciton motion in PPC. It will be explained in detail how spectral densities have to be defined and how they are combined with excitonic wave function expansion coefficients to describe relaxation among the (delocalized) multi-exciton states.

5.1.3. Multi-exciton representation

As discussed in the foregoing sections the actual definition of the reduced density operator and the understanding of the QME has to be based on a certain partitioning into active system and reservoir. In the present section we follow an approach where the whole set of vibrational DOF forms the reservoir and the active system is exclusively defined by the electronic (multi-exciton) DOF, i.e. we set (compare Eq. (45))

$$H_S = \sum_N \mathcal{H}_{el}^{(N)} \hat{P}_N \equiv \sum_N \sum_{\alpha_N} E_{\alpha_N} |\alpha_N\rangle\langle\alpha_N| . \tag{107}$$

The reservoir Hamiltonian is defined via the vibrational Hamiltonian, Eq. (B.7),

$$H_R = H_{vib} \tag{108}$$

and the system reservoir Hamiltonian follows from the coupling Hamiltonian $H^{(N)}_{\text{el–vib}}$, Eq. (B.24), between the exciton manifolds and the vibrational DOF (compare also Eq. (78)):

$$H_{\text{S–R}} = \sum_N H^{(N)}_{\text{ex–vib}} \hat{P}_N \ . \tag{109}$$

To change from the operator equations to those which can be solved at least numerically we introduce the RSO in the representation of multi-exciton states, Eq. (39),

$$\rho(\alpha_N, \beta_M; t) = \langle \alpha_N | \hat{\rho}(t) | \beta_M \rangle \ . \tag{110}$$

The equation of motion for the multi-exciton density matrix is directly obtained after taking the respective matrix elements of Eq. (101). It reads

$$\frac{\partial}{\partial t} \rho(\alpha_N, \beta_M; t) = -\,\mathrm{i}\Omega(\alpha_N, \beta_M)\rho(\alpha_N, \beta_M; t) - \langle \alpha_N | \mathscr{R}\hat{\rho}(t) | \beta_M \rangle \ . \tag{111}$$

The first term on the right-hand side includes the transition frequencies $\Omega(\alpha_N, \beta_M)$ between different multi-exciton states with energies E_{α_N} and E_{β_M}. The dissipative contribution $\mathscr{R}\hat{\rho}$ has to be calculated according to Eq. (99). We use Eq. (79) and obtain for the interaction representation of the system part of $H_{\text{S–R}}$ (u has to be identified with the pair of multi-exciton quantum numbers α_N and β_N)

$$\hat{K}^{(I)}_u(-\,t) = \mathrm{e}^{-\,\mathrm{i}\Omega(\alpha_N, \beta_N)t} |\alpha_N\rangle\langle\beta_N| \ . \tag{112}$$

The operator Λ_u of Eq. (100) follows as

$$\Lambda_u \equiv \Lambda_{\alpha_N,\, \beta_N} = \sum_{M,\; \gamma_M \delta_M} \tilde{C}(\alpha_N, \beta_N; \gamma_M, \delta_M; -\,\Omega(\gamma_M, \delta_M)) |\gamma_M\rangle\langle\delta_M| \ . \tag{113}$$

Here, we introduced the half-sided Fourier transform of the correlation function

$$\tilde{C}_{uv}(\omega) = \int_0^\infty \mathrm{d}t\, \mathrm{e}^{\mathrm{i}\omega t} C_{uv}(t) = -\int \frac{\mathrm{d}\bar{\omega}}{2\pi \mathrm{i}} \frac{C_{uv}(\bar{\omega})}{\omega - \bar{\omega} + \mathrm{i}\varepsilon} \ . \tag{114}$$

According to Eq. (99), expressions (112) and (113) allow to construct all contributions to the dissipative part of the QME in the multi-exciton representation. We do not give the complete expression here, but use an approximation based on the introduction of energy relaxation and dephasing rates. The approximation neglects fast oscillating contributions and is frequently known as the secular approximation [53,103]. Neglecting the so-called environment-induced coherence transfer one ends up with the Bloch model [112] which leads in the present case to the following type of equations:

$$\begin{aligned} \frac{\partial}{\partial t} \rho(\alpha_N, \beta_M; t) = &-\,\delta_{\alpha_N,\, \beta_M} \sum_{\gamma_N} (k(\alpha_N, \gamma_N)\rho(\alpha_N, \alpha_N; t) - k(\gamma_N, \alpha_N)\rho(\gamma_N, \gamma_N t)) \\ &- \mathrm{i}(1 - \delta_{\alpha_N,\, \beta_M})(\Omega(\alpha_N, \beta_M) - \mathrm{i}\Gamma(\alpha_N; \beta_M))\rho(\alpha_N, \beta_M; t) \ . \end{aligned} \tag{115}$$

The energy relaxation rates are given by

$$k(\alpha_N, \gamma_N) = C(\alpha_N, \gamma_N; \gamma_N, \alpha_N; \Omega(\alpha_N, \gamma_N)) \ . \tag{116}$$

Here, we identify $\tilde{C}$ with half of the complete Fourier transform of the correlation function, $C/2$. This approximation corresponds to the neglect of a renormalization of the transition frequencies due to the system-reservoir coupling [53].

Since the model for the EVC used so far does not include transitions among different exciton manifolds the rates are diagonal with respect to N. Further, the dephasing rates read

$$\Gamma(\alpha_N;\beta_M) = \frac{1}{2}\sum_{\gamma_N} k(\alpha_N,\gamma_N) + \frac{1}{2}\sum_{\gamma_N} k(\beta_M,\gamma_N) - 2\,\mathrm{Re}\,C(\alpha_N,\alpha_N;\beta_M,\beta_M;\omega=0)\,, \tag{117}$$

where the zero-frequency part describes pure dephasing.

Eqs. (116) and (117) relate energy dissipation and dephasing to reservoir correlation functions. Therefore, we will consider this quantity in more detail. For the sake of simplicity, we will concentrate on the linear contribution of the coupling to the vibrational DOF, Eq. (81) (nonlinearities in the EVC and the resulting type of correlation function are discussed in Appendix C). The correlation function related to a linear multi-exciton–vibrational coupling can be expressed via a spectral density in accordance with Eq. (103) as

$$C(\alpha_N,\beta_N;\gamma_M,\delta_M;\omega) = 2\pi\omega^2(1+n(\omega))(\mathcal{J}(\alpha_N,\beta_N;\gamma_M,\delta_M;\omega) - \mathcal{J}(\alpha_N,\beta_N;\gamma_M,\delta_M;-\omega))\,. \tag{118}$$

The spectral density reads

$$\mathcal{J}(\alpha_N,\beta_N;\gamma_M,\delta_M;\omega) = \sum_{\xi} g_{\xi}(\alpha_N,\beta_N)g_{\xi}(\gamma_M,\delta_M)\delta(\omega-\omega_{\xi})\,, \tag{119}$$

which is the generalization of Eq. (104). Finally, we note that the temperature enters the theory only via the Bose–Einstein distribution function. Since the correlation functions have to be taken at certain transition frequencies in the energy relaxation rates, Eq. (116) and dephasing rates, Eq. (117) the Bose–Einstein distribution takes a well-defined value. Of course one may let, for example, the site-energies of the Chl molecules become temperature-dependent. But that would be a heuristic way not incorporated in our microscopic theory.

5.1.4. Protein spectral densities

As demonstrated in the preceding section dissipative multi-exciton dynamics can be formulated such that its details are mainly governed by different spectral densities. In the following we will analyze the spectral density, Eq. (119). Since this quantity is given in the multi-exciton representation we have to step back to the site representation to reveal molecular spectral densities.

First, we use Eq. (74) which relates the exciton representation of the multi-exciton vibrational coupling constants to the coupling constants in the site representation. Since the microscopic origin of the coupling is two-fold (modulation of the Chl energy levels and modulation of the mutual Coulomb interaction) we get four different types of spectral densities in the site representation

$$\mathcal{J}(\alpha_N,\beta_N;\gamma_M,\delta_M;\omega)$$

$$= \sum_{\{k\}_N,\{l\}_M} C^*_{\alpha_N}(\{k\}_N)C_{\beta_N}(\{k\}_N)C^*_{\gamma_M}(\{l\}_M)C_{\delta_M}(\{l\}_M)\mathcal{J}(\{k\}_N,\{l\}_M;\omega)$$

$$
\begin{aligned}
&+ \sum_{\{k\}_N,\{l\}_M} \sum_{m\notin\{l\}_M} \sum_{n\in\{l\}_M} C^*_{\alpha_N}(\{k\}_N) C_{\beta_N}(\{k\}_N) C^*_{\gamma_M}(\{l;n\to m\}_M) C_{\delta_M}(\{l\}_M) \\
&\times \mathcal{J}(\{k\}_N, nm, \{l\}_M;\omega) + \sum_{\{k\}_N,\{l\}_M} \sum_{m\notin\{k\}_N} \sum_{n\in\{k\}_N} C^*_{\alpha_N}(\{k;n\to m\}_N) C_{\beta_N}(\{k\}_N) C^*_{\gamma_M}(\{l\}_M) C_{\delta_M}(\{l\}_M) \\
&\times \mathcal{J}(nm, \{k\}_N, \{l\}_N;\omega) + \sum_{\{k\}_N,\{l\}_M} \sum_{m\notin\{k\}_N} \sum_{n\in\{k\}_N} \sum_{\bar m\notin\{l\}_M} \sum_{\bar n\in\{l\}_M} \\
&\times C^*_{\alpha_N}(\{k;n\to m\}_N) C_{\beta_N}(\{k\}_N) C^*_{\gamma_M}(\{l;\bar n\to \bar m\}_M) C_{\delta_M}(\{l\}_M)\ \mathcal{J}(nm, \bar n\bar m;\omega)\ . \qquad (120)
\end{aligned}
$$

All contributions in these expressions are connected with multi-exciton state expansion coefficients (see Eq. (39)). This already indicates that the expression relates the multi-exciton spectral density to locally defined spectral densities. And it shows that the transition from these locally defined spectral densities, once we have them at hand, to the multi-exciton representation can be done exactly since the determination of the $C_{\alpha_N}(\{m\}_N)$ is rather straightforward.

The four different contributions in Eq. (120) are originated by the two types of multi-exciton vibrational coupling constants. The first type $g_\xi(\{k\}_N)$ results from vibrational modulation of the Chl energies and the second type $\tilde g_\xi(nm)$ follows from the modulation of the inter-Chl Coulomb interaction. In their order of appearance the four terms in Eq. (120) are given by the following combinations of coupling constants $g_\xi(\{k\}_N)g_\xi(\{l\}_M)$, $g_\xi(\{k\}_N)\tilde g_\xi(nm)$, $\tilde g_\xi(nm)g_\xi(\{l\}_M)$, and $\tilde g_\xi(nm)\tilde g_\xi(\bar n\bar m)$. These combinations define new spectral densities.

The spectral density in the first term of Eq. (120) reads

$$
\mathcal{J}(\{k\}_N, \{l\}_M;\omega) = \sum_\xi g_\xi(\{k\}_N) g_\xi(\{l\}_M)\delta(\omega-\omega_\xi)\ . \qquad (121)
$$

The spectral densities in the second, third, and fourth term of Eq. (120) are defined in a similar manner. But instead of the coupling constant combination $g_\xi(\{k\}_N)g_\xi(\{l\}_M)$ they contain $g_\xi(\{k\}_N)\tilde g_\xi(nm)$, $\tilde g_\xi(nm)g_\xi(\{l\}_M)$ and $\tilde g_\xi(nm)\tilde g_\xi(\bar n\bar m)$, respectively.

Since the coupling constants of type $g_\xi(\{k\}_N)$ are additive with respect to the different site contributions (compare Eq. (B.18)) three types of elementary spectral densities exist. They follow from the three possible combinations of the coupling constants $g_\xi(m)$ and $\tilde g_\xi(m,n)$. For example, we have

$$
\mathcal{J}(\{k\}_N, \{l\}_M;\omega) = \sum_{m\in\{k\}_N} \sum_{n\in\{l\}_M} \mathcal{J}_{mn}(\omega) \qquad (122)
$$

with the elementary type of spectral density

$$
\mathcal{J}_{mn}(\omega) = \sum_\xi g_\xi(m) g_\xi(n)\delta(\omega-\omega_\xi)\ . \qquad (123)
$$

To discuss the respective expressions in more detail we first introduce the correlation function of the Cartesian nuclear coordinates (Chl plus protein coordinates)

$$
C_{j\bar j}(t) = \langle \Delta R_j(t)\Delta R_{\bar j}\rangle\ . \qquad (124)
$$

Here, the ΔR_j is the deviation of the nuclear coordinate R_j from its equilibrium value $R_j^{(0)}$ (on the PPC ground state PES). The brackets denote the thermal average (with respect to the PPC electronic ground state). According to the normal mode transformation, Eq. (B.2) of Appendix B the thermal average leads to a Bose–Einstein distribution for the mean normal mode occupation numbers. At $T = 0$ one gets the Fourier transform relation

$$C_{j\bar{j}}(\omega; T = 0) = \frac{\hbar}{4\pi\omega} \sum_{\xi} \frac{A_{j\xi}}{\sqrt{M_j}} \frac{A_{\bar{j}\xi}}{\sqrt{M_{\bar{j}}}} \delta(\omega - \omega_\xi) . \tag{125}$$

It has to be understood as the Cartesian coordinate correlation function averaged with respect to the coordinate's zero-point motion. (The $A_{j\xi}$ are the coefficients of the normal mode transformation, and the M_j denote nuclear masses.) $C_{j\bar{j}}$ will be used to present the different types of elementary spectral densities. We have from Eq. (123)

$$\mathcal{J}_{mn}(\omega) = \frac{2\pi}{(\hbar\omega)^2} \sum_{j\bar{j}} \left.\frac{\partial\varepsilon_m(eg; R)}{\partial R_j}\right|_{R = R^{(0)}} \left.\frac{\partial\varepsilon_n(eg; R)}{\partial R_{\bar{j}}}\right|_{R = R^{(0)}} C_{j\bar{j}}(\omega; T = 0) . \tag{126}$$

The second type of spectral density $\mathcal{J}_{m,kl}(\omega)$ follows after replacing $g_\xi(n)$ by $\tilde{g}_\xi(k,l)$. This results in a replacement of $\partial\varepsilon_n(eg; R)/\partial R_{\bar{j}}$ by $\partial J_{kl}(R)/\partial R_{\bar{j}}$. The third type of spectral density $\mathcal{J}_{mn,kl}(\omega)$ is obtained if $g_\xi(m)$ in Eq. (126) is replaced by $\tilde{g}_\xi(m,n)$.

Since simulations for the correlation functions $C_{j\bar{j}}$ are not available for antenna complexes and all derivatives entering the spectral densities are unknown, one has to choose some qualitative arguments to get explicit expressions for the various $\mathcal{J}$. Therefore, let us take a closer look at $\mathcal{J}_{mn}(\omega)$, Eq. (126). This expression correlates sites m and n via their coupling to the various normal modes of the PPC. If there would be only a coupling to local modes around $\mathbf{z}_m$ as well as $\mathbf{z}_n$, $\mathcal{J}_{mn}$ becomes diagonal with respect to the site indices. On the contrary, if the coupling of the normal modes is uniform, i.e. site-independent we expect that $\mathcal{J}_{mn}$ becomes site-independent, too. These two limiting cases suggest that there would be a certain dependence of $\mathcal{J}_{mn}$ on the mutual distance $Z_{mn} = |\mathbf{z}_m - \mathbf{z}_n|$. To be specific, let us further analyze expression (126). It defines the spectral density via the various $C_{j\bar{j}}(\omega; T = 0)$ summed up and weighted with derivatives (of the excitation energies of Chl m and Chl n). We take two reasonable assumptions. First, we provide that $C_{j\bar{j}}(\omega; T = 0)$ can be replaced by a uniform autocorrelation function $C(\omega; T = 0)$ and a function $f(R_j - R_{\bar{j}})$ depending on the distance between the two considered atoms. And second, it is assumed that the derivatives $\partial\varepsilon_m(eg; R)/\partial R_{\bar{j}}$ have to be taken for a subset R_m of nuclear coordinates (coordinates which belong to atoms around Chl m). If we finally assume that the derivatives weakly depend on the site index we obtain

$$\begin{aligned}\mathcal{J}_{mn}(\omega) &\approx f(Z_{mn}) \frac{2\pi}{(\hbar\omega)^2} \left(\sum_j \left.\frac{\partial\varepsilon(eg; R)}{\partial R_j}\right|_{R = R^{(0)}} \right)^2 C(\omega; T = 0) \\ &\equiv f(Z_{mn}) \mathcal{J}(\omega) .\end{aligned} \tag{127}$$

The various functions $f(R_j - R_{\bar{j}})$ related to sites m and n have been approximated by a single function depending on the distance Z_{mn} between both sites. In the second part of this equation the unique spectral density $\mathcal{J}(\omega)$ valid for all sites has been introduced. Since different Chl in the PPC may experience a different protein environment it might be necessary to relax the assumption of a single local spectral density. But as long as there is no evidence for this difference the single spectral density together with the distance function should be a good approximation. With respect to the latter quantity we make the ansatz

$$f(Z_{mn}) = \exp(-Z_{mn}/Z_{\mathrm{corr}}) \,. \tag{128}$$

The quantity Z_{corr} defines a certain distance beyond which any correlation of different sites via protein vibrations vanishes. Using this ansatz we can interpolate between the case of localized and uniform vibrations. Since the distance function is characterized by a single parameter (correlation radius) it becomes possible to determine this quantity via a fit of experimental spectra [84,85]. In the same manner the shape of the unique spectral density can be determined. Therefore, one starts with a reasonable ansatz like

$$\mathcal{J}(\omega) = \mathcal{J}_0 \omega^p \mathrm{e}^{-\omega/\omega_{\mathrm{c}}} \tag{129}$$

and fixes the free parameters $\mathcal{J}_0$, p, and ω_{c} by a comparison with experimental data (for more details see also Section 8). This form is typical for condensed-phase environments whose density of states is characterized by an upper limit for possible frequencies. In principal, one expects a more structured spectral density than given by Eq. (129). However, in many experiments any fine-structure cannot be uncovered, in particular if inhomogeneous line-broadening is present. So it often suffices to only fix the power by which the spectral density grows at small frequencies and the range where it vanishes.

In the case of the elementary spectral density $\mathcal{J}_{k,mn}$ we can repeat this reasoning to get

$$\mathcal{J}_{k,mn}(\omega) \approx \frac{2\pi}{(\hbar\omega)^2}\left(\sum_j \frac{\partial\varepsilon(eg;R)}{\partial R_j}\bigg|_{R=R^{(0)}}\right) \times\left(\sum_{\bar{j}} \frac{\partial J_{mn}(R)}{\partial R_{\bar{j}}}\bigg|_{R=R^{(0)}}\right)(f(Z_{km})+f(Z_{kn}))C(\omega;T=0)\,. \tag{130}$$

However, an additional assumption with respect to the m and n dependence of the derivatives of J_{mn} would be necessary. The same problem appears when considering the last type of elementary spectral density. Up to now computations have only been carried out using relation (127) [84,85]. But it is important to note that the given analysis enables us to relate the general type of spectral density, Eq. (120), to linear combinations of three types of elementary spectral densities. These quantities can be classified with respect to their dependence on the site index. Further, knowing the multi-exciton expansion coefficients C_{α_N} we can evaluate any type of multi-exciton spectral density.

5.1.5. Single-exciton relaxation rates

The considerations in the foregoing sections gave a general frame to introduce multi-exciton correlation functions and spectral densities. To have more specific formulas at hand for further use in the following sections, we will specify the rate expressions, Eq. (116), and dephasing rates, Eq. (117), to the case of the single-exciton manifold. Pure dephasing contributions will be neglected and so we can concentrate on the determination of the single-exciton version $k(\alpha_1,\gamma_1)$ of the energy relaxation rate, Eq. (116). This quantity is related to the protein spectral density via Eq. (118) which, in the following, should be exclusively determined by the EVC induced by the introduction of the single-excitation PES, i.e. the coupling is proportional to $g_\xi(m)$. According to this assumption, Eq. (120) is reduced to the first part proportional to the elementary spectral density $\mathcal{J}_{mn}(\omega)$, Eq. (123). Applying the concept of the correlation radius of protein vibrations introduced in the preceding section the computation of the single-exciton energy relaxation rate is reduced to the determination of a single spectral density $\mathcal{J}(\omega)$ as given in Eq. (129). In summary, the energy relaxation rate (connecting exciton levels separated by the transition energy $\hbar\Omega(\alpha_1,\gamma_1)$) follows as

$$k(\alpha_1,\gamma_1) = 2\pi\Omega^2(\alpha_1,\gamma_1)[1 + n(\Omega(\alpha_1,\gamma_1))]\sum_{m,n} C^*_{\alpha_1}(m)C_{\gamma_1}(m)C^*_{\gamma_1}(n)C_{\alpha_1}(n)$$
$$\times f(Z_{mn})\mathcal{J}(\Omega(\alpha_1,\gamma_1)) - \mathcal{J}(-\Omega(\alpha_1,\gamma_1))\ . \tag{131}$$

From this expression the dephasing rates are simply obtained as

$$\Gamma(\alpha_1,\beta_1) \equiv \Gamma(\alpha_1) + \Gamma(\beta_1) = \frac{1}{2}\sum_{\gamma_1}(k(\alpha_1,\gamma_1) + k(\beta_1,\gamma_1)) \tag{132}$$

with single exciton-level dephasing rates $\Gamma(\alpha_1)$ needed, for example in Section 6.4.2 to characterize homogeneous line broading of an optical transition from the PPC ground-state into a single-exciton level.

5.1.6. Site representation

To derive the site (multi-excitation) representation let us consider the situation where every Chl is described within a three-level model (see Appendix A). In this case one has to compute the density matrix in the site representation (multi-excitation density matrix)

$$\rho(\{ke\}_K\{lf\}_L,\{me\}_M\{nf\}_N;t) = \langle\{ke\}_K;\{lf\}_L|\hat{\rho}(t)|\{me\}_M;\{nf\}_N\rangle\ , \tag{133}$$

which is defined with respect to the multi-excitation states. The advantage of this quantity is that it enables us, for example, to get the spatial distribution of the PPC electronic excitations since it contains the states $|\{ke\}_K\{lf\}_L\rangle$ and $|\{me\}_M;\{nf\}_N\rangle$. From the diagonal elements of the RDM the probability distribution of excited electronic states within the whole PPC is available. In principle, one can calculate the RDM using the site-representation of the QME, Eq. (101). But for a correct description of the electronic excitation energy dissipation one has to change to the electronic eigenstates of the PPC [20,53]. Using these states (the multi-exciton states) one can calculate the dissipative part, Eq. (99), of the QME. Therefore, it is more advisable to compute the RDM in the multi-exciton representation from the very beginning and to change if necessary to a site representation using the inverse relation of Eq. (39). In this manner, for example, the single-excitation distribution is obtained as

$$P_m(t) = \sum_{\alpha_1,\beta_1} C_{\alpha_1}(m)C^*_{\beta_1}(m)\rho(\alpha_1,\beta_1;t)\ . \tag{134}$$

But coherences between different sites are also important which becomes obvious if one calculates the single-excitation RDM for the equilibrium distribution of the electronic PPC excitation over the single exciton states which is given by

$$\rho^{(\mathrm{eq})}_{mn} = \sum_{\alpha_1} C_{\alpha_1}(m)C^*_{\alpha_1}(n)\frac{\exp(-E_{\alpha_1}/k_{\mathrm{B}}T)}{\sum_{\bar{\alpha}_1}\exp(-E_{\bar{\alpha}_1}/k_{\mathrm{B}}T)}\ . \tag{135}$$

Although the single-exciton manifold is in a mixed state spatial coherences are present. However, one has to note that this result is only valid for the case of weak EVC [76].

If details of the EVC are of less importance a description of PPC dynamics using the RDM in the multi-excitation (site) representation can be carried out. In the next section, a related equation of motion approach is shortly reviewed which allows to reduce the number of equations as compared to the number one is faced with in the RDM theory.

5.2. Exciton–vibrational coupling beyond perturbation theory

Since the perturbative treatment of all vibrational DOF offers a numerically feasible way to model exciton dynamics [63] it has found widespread application to simulate related optical spectra as will be documented in detail in Sections 7–9.

However, in order to investigate the possibility of effects like polaron formation or vibrational coherences one has to go beyond the weak coupling limit. Access to this area is provided by models including one or two effective vibrational modes in an exact manner [12,14,100,101]. A procedure based on the wave packet dynamics of certain collective nuclear coordinates representing a set of spectral densities has been proposed in [113]. In the limit of strong static disorder the nonlinear optical response of aggregates described by excitonic PES (see Section 4.3.1) has been given without [79] and with perturbative inclusion [81] of interlevel relaxation. This approach allows for a Brownian oscillator-type modeling of the nuclear DOF [57], assigning them to (in principle arbitrary) spectral densities. An alternative to the effective mode approach is given by a method resulting in the derivation of GMEs for the electronic level populations [78,114,115]. Here, the non-Markovian effect typical for generalized rate equations may become essential since the theory incorporates state populations (diagonal density matrix elements) only.

Since the mentioned techniques did not find such a broad application as the theory accounting for the vibrational DOF perturbatively we only shortly comment on these approaches without going into the theoretical details.

5.2.1. Effective mode models

To account for vibrational coherences one can use a combined description of electronic (excitonic) and vibrational DOF. Obviously, such an approach requires a restriction to effective mode models with one or two vibrational DOF. Otherwise, the dissipative propagation of the electronic and vibrational DOF becomes numerically intractable. An exact description of exciton–vibrational dynamics in a model of a Chl-dimer (appropriate to a Chl*a*–Chl*b* pair of the LHCII PPC) with a single effective mode per monomer was given in [12,14,100,101]. The effect of the remaining nuclear DOF is incorporated via relaxation and dephasing rates for the exciton–vibrational states using the QME (101).

The treatment has been inspired by the description of ultrafast photoinduced electron transfer in donor–acceptor complexes using an electron–vibrational representation of the density matrix [53,116–118]. To compute, for example, the differential absorption measured in a pump–probe experiment [14,101] one expands the density matrix in the product of the two electron–vibrational states $|\varphi_{ma}\rangle|\chi_{ma\mathcal{M}}\rangle$. Here, the site index runs over 1 and 2 and the electronic level index covers besides the ground state index g the first excited state e and a higher excited state f. The vibrational quantum number $\mathcal{M}$ labels the vibrational levels of the respective mode. The central idea of such an effective description is to chose the characteristics of the effective modes (frequency, coupling to electronic levels, vibrational life time and dephasing) by fitting the calculations to measured spectra which show clearly resolved vibrational coherences. If such a characteristic beating structures are absent in the measured spectra the approach is still of great usefulness. It enables one to model polaron effects and to consider the possible retardation of the EVC (non-Markovian effects) [14,101]. Both effects can be accounted for since the coupling of electronic excitations to some effective modes has been treated in an exact manner (cf. Section 9).

5.2.2. The Förster limit

To derive the QME in Section 5.1.1 a perturbation theory with respect to the EVC has been carried out. If this coupling becomes strong an alternative treatment would be the perturbative expansion with respect to the inter-Chl Coulomb interaction J_{mn}, Eq. (15). A microscopic foundation of the EVC expression, Eq. (B.24), could be given in Section B. There it was possible to construct harmonic oscillator PES for the various local PPC excitations. This part of the general EVC can be accounted for exactly. But the remaining off-diagonal coupling part (see the second part in Eq. (15)) requires a perturbative treatment similar to that usually done for J_{mn}. It has been demonstrated in [78] that the lowest-order contribution with respect to J_{mn} and the restriction to the single-exciton manifold results in the well-known Förster-rate of exciton transfer [51].

The general approach beyond a perturbation theory with respect to the EVC can be derived via a so-called Liouville space approach (for an introduction see [53]). It results in a rate equation for state populations including retardation effects (Generalized Master Equation)

$$\frac{\partial}{\partial t} P_A(t) = \sum_B \int_{t_0}^{t} \mathrm{d}\bar{t}\, M_{AB}(t-\bar{t}) P_B(\bar{t}) \; . \tag{136}$$

Here, A and B abbreviate a multi-excitation state, e.g. the state $|\{me\}_M, \{nf\}_N\rangle$ based on the three-level Chl model. The respective state population has been denoted by $P_A(t)$. It is possible to derive a formal exact expression for the memory kernel $M_{AB}(t)$ [53,78,114,115] which is obtained as a power expansion with respect to the Coulomb inter-Chl coupling.

One can easily change to an ordinary rate equation if the memory effect has been neglected in Eq. (136). As an illustration we show how to obtain the standard rate expression for the transfer of a single excitation between two Chl $m = 1$ (excitation energy donor) and $m = 2$ (acceptor) with the perturbation J_{12}. From the lowest-order two-state version of the exact memory kernel we obtain the transition rate as

$$k_{1\to 2} = -\,\mathrm{i}\,\mathrm{tr}\{\hat{P}_2 \mathscr{L}_J \mathscr{G}_0(\omega = 0) \mathscr{L}_J \hat{R}_1 \hat{P}_1\} \; . \tag{137}$$

Here, "tr" abbreviates the trace with respect to all electron–vibrational DOF and incorporates the projection operators $P_{m=1,2} = |m\rangle\langle m|$ which project on the two electronic states involved. The Liouville superoperator describing the effect of the Coulomb coupling J_{mn} reads

$$\mathscr{L}_J \ldots = \frac{1}{\hbar}(J_{12}|\phi_1\rangle\langle\phi_2| + \mathrm{h.c.}, \ldots)_- \; . \tag{138}$$

Finally, $\hat{R}_1$ is the equilibrium statistical operator of the vibrational DOF if the excitation is at site $m = 1$. The time evolution from initial state $m = 1$ (projector $\hat{P}_1$ at the right part of the trace) to the final state $m = 2$ (projector $\hat{P}_2$ at the left part of the trace) is contained in the superoperator $\mathscr{G}_0(\omega)$. This Green's superoperator follows from a half-sided Fourier transformation of the time-evolution superoperator. It is defined as $\mathscr{U}_0(t)\ldots = U_0(t)\ldots U_0^+(t)$, where the ordinary time-evolution operator U_0 is given by the zeroth-order Hamiltonian without the Coulomb coupling, i.e. they are defined by the single-Chl vibrational Hamiltonian $H_{m=1,2} = T_{\mathrm{nuc}} + U(m; R)$ (compare Eqs. (64) and (63)). Utilizing the definition of the Green's operator and introducing the explicit form of $\mathscr{L}_J$ one obtains the transfer rate as

$$k_{1\to 2} = -\frac{1}{\hbar^2}\int_0^\infty \mathrm{d}t\,\mathrm{tr}_{\mathrm{vib}}\{\langle\phi_2|[(J_{12}|\phi_1\rangle\langle\phi_2| + \mathrm{h.c.}),$$

$$U_0(t)[J_{12}|\phi_1\rangle\langle\phi_2| + \mathrm{h.c.}, \hat{R}_1\hat{P}_1]_- U_0^+(t)]_-|\phi_2\rangle\}\ . \tag{139}$$

This expression has been derived in separating the trace into the electronic part $\sum_{m=1,2}\langle\phi_m|\ldots|\phi_m\rangle$ and the vibrational part $\mathrm{tr}_{\mathrm{vib}}\{\ldots\}$. Furthermore, the action of $\hat{P}_2$ has already been accounted for. Performing the commutation operations we finally get

$$k_{1\to 2} = \frac{|J_{12}|^2}{\hbar^2}\int_0^\infty \mathrm{d}t\,\mathrm{tr}_{\mathrm{vib}}\{\hat{R}_1 U_1^+(t)U_2(t)\} + \mathrm{c.c.} \tag{140}$$

The Förster rate can be recovered after introducing two sets of independent electron–vibrational states belonging either to Chl 1 or 2. We introduce the vibrational quantum numbers belonging to the electronic ground-state φ_{mg} and the excited electronic state φ_{me} as $\mathscr{M}_m$ and $\mathscr{N}_m$, respectively, and obtain

$$k_{1\to 2} = \frac{2\pi}{\hbar^2}|J_{12}|^2 \sum_{\mathscr{M}_1,\mathscr{N}_1}\ \sum_{\mathscr{M}_2,\mathscr{N}_2} f(E_{1e\mathscr{N}_1})f(E_{2g\mathscr{M}_2})$$

$$\times|\langle\chi_{1e\mathscr{N}_1}|\chi_{1g\mathscr{M}_1}\rangle|^2|\langle\chi_{2g\mathscr{M}_2}|\chi_{2e\mathscr{N}_2}\rangle|^2\delta(E_{1e\mathscr{N}_1} + E_{2g\mathscr{M}_2} - E_{1g\mathscr{M}_1} - E_{2e\mathscr{N}_2})\ . \tag{141}$$

As it is well-known the rate can be written as [53]

$$k_{1\to 2} \sim \int \mathrm{d}\omega\, e_1(\omega)a_2(\omega)\ , \tag{142}$$

where $e_1(\omega)$ and $a_2(\omega)$ describe the normalized emission rate of Chl 1 and absorption rate of Chl 2, respectively. This notation is a consequence of the separation of the vibrational DOF into two independent subsets whose spectral overlap determines the strength of the (incoherent) excitation energy transfer.

Higher-order contributions may enter the approach in two different ways. On the one-hand side, one can go beyond the second-order rate expression derived before. Such an extension includes higher orders in the electronic coupling between Chl 1 and Chl 2. Alternatively, the description may involve a third Chl. This three-site system of a donor Chl, a single intermediate Chl (bridge unit), and an acceptor Chl ($m = D, B, A$, respectively) results in a transfer rate proportional to $|J_{DB}|^2|J_{BD}|^2$ (the direct coupling J_{DA} has been assumed to be negligible small). Depending on the rate of vibrational relaxation in the intermediate state B, this higher-order transfer is called superexchange or sequential transfer. In the latter case, the fast relaxation in the intermediate state destroys any electronic coherence between state D and A. The situation is opposite in the superexchange transfer. Here, the electronic state cover all three states D, B and A. Such a situation has been discussed in Ref. [78] concentrating on the single-exciton transfer.

In the three-site system the lowest-order contribution to the rate connecting the donor and acceptor is of the fourth order with respect to J. Its nonfactorized part reads (all parts are defined in similarity to Eq. (137), for a detailed derivation see, e.g. [53])

$$k^{(4)}_{D\to A} = -\mathrm{i}\,\mathrm{tr}\{\hat{P}_A \mathscr{L}_J \mathscr{G}_0(\omega=0)\mathscr{L}_J \mathscr{G}_0(\omega=0)\mathscr{L}_J \mathscr{G}_0(\omega=0)\mathscr{L}_J \hat{R}_D \hat{P}_D\}\ . \tag{143}$$

The expression under the trace can be understood as the frequency-domain form of the multiple action of the inter-Chl coupling J (via $\mathscr{L}_J$) and the subsequent action of time-evolution operators (via $\mathscr{G}_0(\omega)$). Therefore, provided that the different Green's superoperators are transformed into the time-domain, one arrives at the multi-time correlation function expression for the transfer rate. It is similar to the third-order response function which will be introduced in Section 6.5.1 in connection with the description of third-order nonlinear optical processes. Since the present description was formulated in the multiple-excitation representation one has to choose the respective PES, for example, of the type $U(\{k\}_N; Q)$, Eq. (B.17). Then, the rate, Eq. (143) can be exclusively expressed by correlation functions introduced in Eq. (120) with site-local spectral densities $\mathscr{J}_m(\omega)$. In [78] the rate expression, Eq. (143) has been computed using a spectral density which describes overdamped motion of the vibrational DOF. Some parameter ranges could be identified where the frequency-dependent rate becomes negative. This behavior indicates that the rate equation neglecting memory effects is no longer valid.

5.2.3. Multi-exciton–vibrational relaxation

An alternative to the perturbation theory discussed in the preceding section is obtained using the separation of the multi-exciton–vibrational Hamiltonian given in Eq. (83). Here, excitonic PES have been introduced leaving a residual EVC which is off-diagonal with respect to the multi-exciton quantum numbers [79,81] (see also scheme 5). The latter can be handled within a perturbation theory either as in [79] ending up with a QME for conditional probabilities, or leading to the generalized rate equation of the present approach.

According to the general notation of Eq. (136) we directly obtain the rate equation for the multi-exciton level population $P(\alpha_N; t)$ after identifying the indices A and B with the multi-exciton quantum numbers. The transition rate in the lowest-order of the off-diagonal multi-exciton–vibrational coupling, Eq. (83), follows from Eq. (137) as

$$k_{\alpha_N\to\beta_N} = -\mathrm{i}\,\mathrm{tr}\{\hat{P}_{\beta_N} \mathscr{L}_{\mathrm{od}} \mathscr{G}_0(\omega=0)\mathscr{L}_{\mathrm{od}} \hat{R}_{\alpha_N} \hat{P}_{\alpha_N}\}\ . \tag{144}$$

The Liouville superoperator $\mathscr{L}_{\mathrm{od}}$ is defined via a commutator with the off-diagonal contributions to the multi-exciton vibrational coupling, Eq. (83). The expression is valid for the N-excitation manifold and already incorporates the fact that the relaxation proceeds without inter-manifold transitions. A projection on the initial and final multi-exciton state is described by $\hat{P}_{\beta_N}$ and $\hat{P}_{\alpha_N}$, respectively. Furthermore, $\hat{R}_{\alpha_N}$ denotes the equilibrium statistical operator related to the initial-state excitonic PES $U(\alpha_N, Q)$, and $\mathscr{G}_0(\omega=0)$ gives the half-sided Fourier-transformed time-evolution superoperator (defined via the excitonic PES).

Although the rate expression, Eq. (144), describes exciton–vibrational relaxation in any exciton manifold we will concentrate on the single-exciton case in the following (the index $N = 1$ is suppressed for simplicity). Consequently, the relaxation rate is obtained as

$$k_{\alpha\to\beta} = \sum_{\xi,\bar{\xi}} \omega_\xi \omega_{\bar{\xi}} g_\xi(\alpha\beta) g_{\bar{\xi}}(\beta\alpha) \int \mathrm{d}t \, \mathrm{tr}_{\mathrm{vib}}\{\hat{R}_\alpha U_\alpha^+(t) Q_\xi U_\beta(t) Q_{\bar{\xi}}\} \ . \tag{145}$$

Besides the off-diagonal EVC constants $g_\xi(\alpha\beta)$ the expression contains the statistical operator $\hat{R}_\alpha$ and the time-evolution operators $U_\alpha^+(t)$, and $U_\beta(t)$ defined via the vibrational Hamiltonians for the various exciton states (including excitonic PES). Since in the present model all excitonic PES have the same parabolic shape and are displaced with respect to the coordinates Q_ξ the rate expression can be calculated exactly. One obtains

$$k_{\alpha\to\beta} = \int \mathrm{d}t \, \mathrm{e}^{\mathrm{i}\omega_{\alpha\beta}t} K_{\alpha\beta}(t) \tag{146}$$

with

$$K_{\alpha\beta}(t) = \int_0^\infty \mathrm{d}\omega \, \omega^2 \mathrm{e}^{-\mathrm{i}\omega t}(1 + n(\omega))(\mathscr{J}(\alpha,\beta,\beta,\alpha;\omega) - \mathscr{J}(\alpha,\beta,\beta,\alpha;\, -\omega))$$
$$+ \Gamma_{\alpha\beta}^{(1)*}(-t)\Gamma_{\alpha\beta}^{(1)}(t)\exp(\Gamma_{\alpha\beta}^{(2)}(t)) \ . \tag{147}$$

The spectral density $\mathscr{J}$ has already been introduced in Eq. (120). The first term corresponds to the correlation function of the vibrational coordinates. The remaining terms are obtained as

$$\Gamma_{\alpha\beta}^{(1)}(t) = \int_0^\infty \mathrm{d}\omega \, \omega(1 + \mathrm{e}^{-\mathrm{i}\omega t}(1 + n(\omega)))(\mathscr{J}(\alpha,\beta,\alpha,\alpha;\omega) - \mathscr{J}(\alpha,\beta,\beta,\beta;\omega)) \tag{148}$$

and

$$\Gamma_{\alpha\beta}^{(2)}(t) = \int_0^\infty \mathrm{d}\omega \, (1 + \mathrm{e}^{-\mathrm{i}\omega t})(1 + n(\omega))$$
$$([\mathscr{J}(\alpha,\alpha,\alpha,\alpha;\omega) - 2\mathscr{J}(\alpha,\alpha,\beta,\beta;\omega) + \mathscr{J}(\beta,\beta,\beta,\beta;\omega)] - [\omega \leftarrow -\omega]) \ . \tag{149}$$

Eq. (146) gives a closed expression for the description of exciton–vibrational relaxation in the single-exciton manifold.

5.3. Exciton annihilation

Exciton annihilation has to be incorporated into the description of the PPC dynamics whenever higher pump intensities are applied. The annihilation process consists of two steps. First, the mutual Coulomb interaction between two excitons leads to an excitation of one molecule into a higher excited state and the other molecule gets de-excited. In the second step, the highly excited state relaxes back to the original state via internal conversion. As a result a single exciton has been annihilated and heat is released into the local environment.

The investigation of exciton annihilation has a long history in particular in the context of molecular crystals. The appropriate theoretical frame has been provided in [119] and later in

[120,121] where the following kinetic equation could be derived:

$$\frac{\partial n(\boldsymbol{r};t)}{\partial t} = -\gamma_{\mathrm{anni}}[n(\boldsymbol{r};t)]^2 . \tag{150}$$

Here, $n(\boldsymbol{r};t)$ denotes the spatial density of excitons, and the expression γ_{anni} is the bimolecular annihilation rate. Moreover, Ref. [119] contains a quantum statistical formulation of exciton hopping based on multi-exciton density matrices. This approach reveals that the quadratic dependence on the exciton density in Eq. (150) results from a certain type of mean-field approximation (the exact treatment will lead to linear rate equations, see below). Similar conclusions have been reached in Ref. [120] where also a Generalized Master Equation description of exciton annihilation incorporating spatial coherences on the lattice was given. The latter effect was shown to influence quantum yields and fluorescence intensity.

Exciton annihilation has also been studied in dye aggregates [122–125] and PPCs. In photosynthesis research, it was appreciated early that measuring fluorescence decay and quantum yields versus pulse intensity can provide valuable information on exciton migration in a so-called domain, that is, a connected assembly of photosynthetic units each consisting of light harvesting antennae as well as reaction centers. A phenomenological Master Equation describing the kinetics of the number of excitations in a domain under annihilation and unimolecular loss conditions was given in [126]. From an analytical solution of the Master Equation by means of the generating function approach it was shown that the fluorescence yield versus intensity curve contains information on the number of connected units in the domain. This approach was later extended in [127] to include the different states (open/closed) of the reaction center. The early work on exciton annihilation in PPC has been summarized in [128]. More recent studies on energy migration and trapping include the modeling of structural and spectrally inhomogeneous situations [129] and the extension of the approach given in [119] to higher excited intramolecular electronic states, to trapping, and to the excitation process [130].

In the experiment, it has been demonstrated that singlet–singlet and singlet–triplet annihilation can be discriminated upon changing the pulse repetition rate (see, e.g., [131]). Combined with phenomenological theories this allowed to study, for instance, the connectivity of chloroplasts [132], or energy migration in photosynthetic bacteria; the latter revealing a percolation-like nature of the dynamics [131]. Further, pump–probe spectroscopy has been used to elucidate the effect of local heating due to exciton annihilation in the FMO complex [133], to study the interplay between exciton relaxation and annihilation in the strongly coupled peripheral antennae of *Rps. acidophila* [134], and to investigate spectral redistribution in the LHC-II of green plants [135].

In the recent paper [15], the anharmonic oscillator model for PPC electronic excitations (compare Appendix D) has been used to model exciton annihilation. Here, we will discuss this process in the same spirit as exciton hopping and relaxation has been discussed in the foregoing sections. To this end we take in the present section the PPC Hamiltonian, Eq. (83), which includes excitonic PES and off-diagonal exciton vibrational coupling. The latter as well as the internal conversion caused by the nonadiabatic coupling, Eq. (58), can be subject to a perturbational treatment. Applying the Liouville space approach one can derive rate equations (or GMEs) for the multi-exciton state populations. This general concept enables one, for example, to describe the transition from the two-exciton manifold to the single-exciton manifold induced by the nonadiabatic coupling between the S_1-state of a single Chl and a higher excited singlet state. Having calculated the respective transition rate one can make contact with the standard description of the exciton annihilation process. This is achieved by including perturbationally the transition from the state $|me, ne\rangle$ of the set of double-excited PPC states to the state $|mf\rangle$ with a double excitation at a single Chl.

The general rate expression describing transitions among neighboring exciton manifolds and being of the lowest order with respect to intra-Chl nonadiabatic electronic level coupling reads (compare the notation used in the two foregoing sections)

$$k_{\alpha_M \to \beta_N} = -\mathrm{i}\,\mathrm{tr}\{\hat{P}_{\beta_N} \mathscr{L}_{\mathrm{na}} \mathscr{G}_0(\omega = 0) \mathscr{L}_{\mathrm{na}} \hat{R}_{\alpha_M} \hat{P}_{\alpha_M}\} \; . \tag{151}$$

The trace incorporates the transition from the initial state $|\alpha_M\rangle$ of the M-excitation exciton manifold (characterized here be the respective projector $\hat{P}_{\alpha_M}$ on this state and the thermal equilibrium statistical operator of the vibrational DOF) to the final state $|\beta_N\rangle$ (projector $\hat{P}_{\beta_N}$). The transition is realized by the action of the nonadiabatic coupling, Eq. (58), represented here by the Liouville superoperator $\mathscr{L}_{\mathrm{na}} \ldots = (H_{\mathrm{na}}, \ldots)_-/\hbar$, and by the action of the time-evolution operator contained in the half-sided Fourier transformed superoperator $\mathscr{G}_0(\omega = 0)$.

In the following, we will concentrate on the decay of a two-exciton state $|\alpha_2\rangle$ into a single-exciton state $|\beta_1\rangle$. We expect a rate equation of the type

$$\frac{\partial}{\partial t} P(\alpha_2, t) = -\sum_{\beta_1} k_{\alpha_2 \to \beta_1} P(\alpha_2, t) \tag{152}$$

to exist. The annihilation rate is obtained from the general expression (151) as

$$k_{\alpha_2 \to \beta_1} = \frac{1}{\hbar^2} \int \mathrm{d}t\, \mathrm{tr}_{\mathrm{vib}}\{\hat{R}_{\alpha_2} U^+_{\alpha_2}(t) \hat{V}_{\alpha_2\beta_1} U_{\beta_1}(t) \hat{V}^+_{\alpha_2\beta_1}\} \; , \tag{153}$$

where we introduced the multi-exciton representation of the nonadiabatic coupling, Eq. (58). It results in

$$\begin{aligned} \hat{V}_{\alpha_2,\beta_1} &= \sum_m \Theta(mf, me) \langle \alpha_2 | D^+_m | \beta_1 \rangle \\ &= \sum_m \Theta(mf, me) C^*_{\alpha_2}(me) C_{\beta_1}(mf) \; . \end{aligned} \tag{154}$$

The single- and two-exciton expansion coefficients can be found in Eqs. (42) and (43).

To obtain the rate $k_{me,ne \to me}$ which is of second order in the coupling matrix $J_{mn}(fg, ee)$ we first consider the trace in Eq. (153) obtained after carrying out the expansion Eq. (154). One gets $\mathrm{tr}_{\mathrm{vib}}\{\hat{R}_{\alpha_2} U^+_{\alpha_2}(t) \Theta_{mf,me} U_{\beta_1}(t) \Theta^*_{mf,me}\}$. To describe the internal conversion process at the mth Chl one has to identify α with mf and β with me. The transition from state $|me, ne\rangle$ to state $|mf\rangle$ is included via an expansion of $C_{\alpha_2}(me)$ with respect to $J_{mn}(fg, ee)$. To this end one calculates the first-order correction to $C_{\alpha_2}(me)$, if α (in zeroth-order) has been identified with (me, ne). This gives $J_{mn}(fg, ee)/(\varepsilon_m(fg) - \varepsilon_m(eg) - \varepsilon_n(eg))$ and we obtain the exciton annihilation rate as

$$k_{me,ne \to me} = \left| \frac{J_{mn}(fg, ee)}{\varepsilon_m(fg) - \varepsilon_m(eg) - \varepsilon_n(eg)} \right|^2 k^{(\mathrm{IC})}_m \; . \tag{155}$$

The rate of the internal conversion process at Chl$m$ can be written as

$$k_m^{(\mathrm{IC})} = \frac{|\Theta_{mf,me}|^2}{\hbar^2} \int \mathrm{d}t \ \mathrm{tr}_{\mathrm{vib}}\{\hat{R}_{mf} U_{mf}^{+}(t) U_{me}(t)\} \ . \tag{156}$$

For simplicity, we have considered the nonadiabatic coupling as being constant. The time-evolution operators are defined via the vibrational Hamiltonian of the two involved electronic states of Chl m. The respective vibrational DOF are of the intramolecular type and act as accepting modes for the nonradiative transition. Here in particular the high-frequency vibrations will play an important role.

The relevance of the derived result for the exciton annihilation rate, Eq. (155), derives from the fact that it becomes directly proportional to the correct internal conversion rate expression. According to the general PPC model introduced in the foregoing sections one can include from the very beginning the correct nonadiabatic coupling as well as the respective accepting modes for the internal conversion process. And, the method shows how to derive higher-order corrections to the rate expression Eq. (155). In particular, it seems appropriate to carry out the calculations within in the multi-exciton representation thus avoiding the incorporation of any perturbational description of the Coulomb coupling J_{mn}.

6. Optical properties of excitons in pigment–protein complexes

6.1. General

Various spectroscopic techniques have been employed to investigate the properties of PPC in light-harvesting antennae in the time and frequency domain (for reviews see [17,19]). From the theoretical point of view the methods of macroscopic electrodynamics of dielectrics have to be used. Within this approach the basic quantity is the macroscopic polarization vector

$$\boldsymbol{P}(\boldsymbol{r}, t) = \frac{1}{\Delta V(\boldsymbol{r})} \sum_{\mathrm{PPC} \in \Delta V(\boldsymbol{r})} \langle \hat{\mu}_{\mathrm{PPC}}(t) \rangle \ , \tag{157}$$

which emerges from a spatial averaging procedure and which enters Maxwell's equations as a source term. Here, $\hat{\mu}_{\mathrm{PPC}}$ is the dipole moment operator, Eq. (47), describing one of those PPCs located in the volume element ΔV around the spatial point $\boldsymbol{r}$. The time-dependent expectation value of the dipole operator is given by the statistical operator for the particular PPC according to $\langle \hat{\mu}_{\mathrm{PPC}}(t) \rangle = \mathrm{tr}\{\hat{W}(t)\hat{\mu}_{\mathrm{PPC}}\}$. If inhomogeneous broadening (static disorder) can be neglected the formula for the polarization can be simplified by introducing the volume density n_{PPC} of PPCs and one obtains $\boldsymbol{P}(\boldsymbol{r}, t) = n_{\mathrm{PPC}} \langle \hat{\mu}_{\mathrm{PPC}}(\boldsymbol{r}, t) \rangle$. The only difference among the various PPCs defining $\langle \hat{\mu}_{\mathrm{PPC}}(\boldsymbol{r}, t) \rangle$ is the amplitude and phase of the externally applied radiation field. This induces the spatial $\boldsymbol{r}$-dependence of the dipole operator expectation value.

The statistical operator $\hat{W} = \hat{W}(t; \boldsymbol{E})$ is defined including the external fields. It can be straightforwardly calculated using a perturbation expansion with respect to the external field $\boldsymbol{E}$ [57,136]. This leads to multiple time integrals over nonlinear response functions which can be used, for example, to develop an intuitive doorway-window picture of pump–probe spectroscopy [80,137].

In general, one has to account for propagation effects of the external field inside the sample when calculating optical signals. This would require a self-consistent solution of the Liouville equation for the statistical operator and Maxwell's equation with $\boldsymbol{P}(\boldsymbol{r}, t)$ as the source term. Usually, this ambitious program must not be executed if it is possible to assume an optically thin sample. Within the context of LHAs the perturbation expansion of the statistical operator is complicated by the structure of the PPC Hamiltonian which contains two types of perturbations itself: the Coulomb interaction between different Chl and the EVC. Depending on the situation this problem can be tackled by different types of perturbation expansions as discussed in Section 6.2, In order to keep the matter simple we will consider the case of linear absorption spectroscopy first. In Section 6.5, we then discuss some points concerning the nonlinear spectroscopy of LHAs.

For most of the experiments on PPCs a third-order expansion of the polarization with respect to the electric field strength defines the appropriate theoretical framework. The various spectroscopic techniques which can be described by means of a third-order response function are explained in detail in Ref. [57]. If the electron–vibrational levels involved in the optical transitions can be characterized by harmonic PES, the third-order response function can be calculated exactly. Alternatively, one can derive equations of motion for exciton creation and annihilation operators which are closed within a certain order and can be solved by standard numerical methods [138]. If only linear spectroscopic techniques are concerned one can stay with the first-order contribution resulting in the linear susceptibility $\chi^{(1)}$.

Ultrafast nonlinear spectroscopy has proven to be a powerful method for investigating the energy transfer dynamics of LHAs in real time [17,19]. In the weak field limit it is customary to classify the various techniques according to the wave vector dependence, the frequencies, and the timings of the various fields [57]. The external field for an N-pulse setup can be written as

$$\boldsymbol{E}(\boldsymbol{r}, t) = \sum_{p=1}^{N} \boldsymbol{e}_p E_p(t) \exp\{\mathrm{i}(\boldsymbol{k}_p \boldsymbol{r} - \Omega_p t)\} + \text{c.c.} \tag{158}$$

This type of field corresponds to a multi-wave mixing experiment. Here $\boldsymbol{e}_p$ denotes the unit vector of the polarization of the pth pulse and $E_p(t)$ is the pulse envelope. Since we will work in the limit of an optically thin probe we can neglect the $\boldsymbol{r}$-dependence of the field at the end. In order to classify the polarization created by the different pulses one can start with an expansion of the field-dependent statistical operator with respect to the various partial waves forming the complete external field pulse, Eq. (158). In the general case, this results in an infinite-order expansion with respect to every partial wave [139]

$$\hat{W}(t; \boldsymbol{E}) = \sum_{n_1=-\infty}^{\infty} \cdots \sum_{n_N=-\infty}^{\infty} \exp\left\{\mathrm{i} \sum_{p=1}^{N} n_p(\boldsymbol{k}_p \boldsymbol{r} - \omega_p t)\right\} \hat{W}^{(\{n_p\})}(t; \{E_p\}) \,. \tag{159}$$

This expression can be understood as the result of an expansion of the evolution operators for propagating $\hat{W}$ in time with respect to all partial waves (pulses) forming the total field. In particular, the expansion coefficients depend on the whole set $\{E_p\}$. Seeming at first glance too difficult for any concrete calculation we will demonstrate below that, if applied in the framework of the QME, this expansion offers a nice alternative to the application of third (or fifth)-order response functions (see also the similar expansion used in [140]). For a compact notation we introduce sum-wave vectors

$$\boldsymbol{k}(n) = \sum_p n_p \boldsymbol{k}_p \tag{160}$$

and sum-frequencies

$$\omega(n) = \sum_p n_p \omega_p \ , \tag{161}$$

where n abbreviates the set $\{n_p\}$ (and similar for E). It follows that

$$\hat{W}(t;\boldsymbol{E}) = \sum_n \exp\{\mathrm{i}(\boldsymbol{k}(n)\boldsymbol{r} - \omega(n)t)\}\hat{W}^{(n)}(t;E) \ . \tag{162}$$

The expansion of the statistical operator translates into a similar expansion of the polarization vector

$$\boldsymbol{P}(\boldsymbol{r},t) = \sum_n \boldsymbol{e}(n)P^{(n)}(t)\exp\{\mathrm{i}(\boldsymbol{k}(n)\boldsymbol{r} - \omega(n)t)\} \ . \tag{163}$$

The signal measured in a multi-wave mixing experiment can be obtained from the rate of change in energy a probe pulse experiences in the sample (heterodyne detection, [57])

$$S(t) = -\int \mathrm{d}^3\boldsymbol{r}\frac{\partial \boldsymbol{E}(\boldsymbol{r},t)}{\partial t}\boldsymbol{P}(\boldsymbol{r},t) \ . \tag{164}$$

If the expansion relation, Eq. (158) for the radiation field and Eq. (163) for the polarization are inserted one gets within the slowly varying amplitude approximation

$$S(t) = \sum_p \sum_n 2\omega_p \mathrm{Re}\int \mathrm{d}^3\boldsymbol{r}\exp - \mathrm{i}[(\boldsymbol{k}_p - \boldsymbol{k}(n))\boldsymbol{r} - (\omega_p - \omega(n))t](\boldsymbol{e}_p\boldsymbol{e}(n))E_p^*(t)P^{(n)}(t) \ . \tag{165}$$

The polarization wave traveling along a particular direction specified by $\boldsymbol{k}_s$ can be calculated from the respective expansion coefficient in Eq. (159). In a pump–probe setup, for example, the detection is along the direction of the probe pulse, $\boldsymbol{k}_s = \boldsymbol{k}_1$, and one needs to calculate $\hat{W}^{0,1}(t)$. In a general four-wave mixing experiment the determination of the polarization along $\boldsymbol{k}_s = \boldsymbol{k}_3 + \boldsymbol{k}_2 - \boldsymbol{k}_1$, the coefficient $\hat{W}^{-1,1,1}(t)$ is required [138].

The signal related to the energy loss Eq. (165) can be measured in the time-integrated mode $\sim \int \mathrm{d}t\, S(t)$. Alternatively, the transmitted probe-pulse can be dispersed in a monochromator and one obtains a signal $\sim \mathrm{Im}\{E_\omega^* P_\omega\}$. Here the Fourier components read $E_\omega^* = 1/2\pi \times \int \mathrm{d}t \exp\{\mathrm{i}(\omega_p - \omega)t\}E_p^*(t)$ and $P_\omega = 1/2\pi \times \int \mathrm{d}t \exp\{\mathrm{i}(\omega - \omega_p)t\}P_p(t)$. In this way, the Fourier spectrum of ultrafast pulses can be used to obtain additional spectral information on ultrafast processes. However, it is clear from the energy–time uncertainty relation that the spectrometer will stretch the probe-pulse and also the polarization wave in time, thus giving rise to additional interference effects. The smaller the detection bandwidth the longer the time interval for which these interferences occur. This explains, for example, the oscillations found for negative delay times in pseudo-two-color pump–probe experiments [141]. In the case of homodyne detection the intensity of the field emitted by the induced polarization is directly measured, and the signal is given by $S(t) = \int d^3\boldsymbol{r}\,|\boldsymbol{P}(\boldsymbol{r},t)|^2$.

6.2. Application of the reduced density operator formalism

Expansion Equation (162) for the statistical operator in terms of the partial waves of the light field can of course be applied to the reduced density operator. In this case it leads to the expansion coefficients $\hat{\rho}^{(n)}(t;\boldsymbol{E})$. While this generates in principle an infinite hierarchy of equations of motion for the time-dependent expansion coefficients $\hat{\rho}^{(n)}(t)$ in practice, up to a certain order in the field and for a particular experimental setup, only a few coefficients need to be calculated [64]. If one is interested in a nonperturbative treatment of the field–matter interaction, the hierarchy of equations has to extended until some convergence criteria are fulfilled. For the special case of pump–probe experiments it has been shown in [101] that the set of equations can be closed when using the rotating wave approximation.

Let us first show how the QME for the RSO modifies if the partial-wave expansion is introduced. Using Eq. (101), one obtains

$$\left(\frac{\partial}{\partial t} + \mathrm{i}\omega(n)\right)\hat{\rho}^{(n)}(t) = -\mathrm{i}\mathscr{L}_{\mathrm{eff}}\hat{\rho}^{(n)}(t) + \frac{\mathrm{i}}{\hbar}\sum_{p}\big(E_p(t)[\boldsymbol{e}_p\hat{\mu}_{\mathrm{PPC}}, \hat{\rho}^{(\ldots,n_p-1,\ldots)}(t)]$$

$$+ E_p^*(t)[\boldsymbol{e}_p\hat{\mu}_{\mathrm{PPC}}, \hat{\rho}^{(\ldots,n_p+1,\ldots)}(t)]\big)\ . \tag{166}$$

The field-independent part of the QME has been comprised in $\mathscr{L}_{\mathrm{eff}}$ (see Eq. (102)). For the following it is important that the energy gap between neighboring excitonic manifolds, $E_{\alpha_{N+1}} - E_{\beta_N}$, is approximately the same for all manifolds and in the range of the frequencies of the external light fields. We further assume that the rotating wave approximation can be applied and that the system can be excited between neighboring levels only.

To see how the infinite set of equations of motion (166) can be truncated let us discuss a pump–probe configuration where a weak probe pulse ($p = \mathrm{pr}$) is used to study the effect of a strong pump pulse ($p = \mathrm{pu}$). It is advantageous for the following discussion to change to the multi-exciton representation of Eq. (166). In the absence of the external field and without the partial-wave expansion the multi-exciton representation of the QME has been given in Eqs. (111) and (115) where the dissipative part has been specified. A detailed inspection of the dissipative contribution to the QME as given in Section 5.1.3 shows that they do not couple different exciton-manifolds (obviously, the inclusion of internal conversion processes would change this conclusion). Therefore, we can concentrate on the free multi-exciton part and the coupling to the light pulses. For the former we get from Eqs. (111) and (166) (for clarity, multi-exciton quantum numbers, for example α_N, are replaced by the manifold indices M, N, and so on)

$$\frac{\partial}{\partial t}\rho^{(n_{\mathrm{pu}},n_{\mathrm{pr}})}(M,N;t)|_0 = -\left(\sum_{p=\mathrm{pu,pr}} n_p\omega_p - \Omega(M,N)\right)\rho^{(n_{\mathrm{pu}},n_{\mathrm{pr}})}(M,N;t)\ . \tag{167}$$

Note that these relations account for the fact that the frequencies of the external fields have to match the transition energies of the system. For the field-dependent part of the QME expansion we get

$$\frac{\partial}{\partial t}\rho^{(n_{\rm pu},n_{\rm pr})}(M,N;t)|_F = \frac{\rm i}{\hbar}\sum_{p={\rm pu,pr}} E_p(t)(\boldsymbol{e}_p\boldsymbol{d}(M,M-1)\rho^{(n_p-1)}(M-1,N;t)$$

$$-\,\boldsymbol{e}_p\boldsymbol{d}(N+1,N)\rho^{(n_p-1)}(M,N+1;t))$$

$$+\frac{\rm i}{\hbar}\sum_{p={\rm pu,pr}} E_p^*(t)(\boldsymbol{e}_p\boldsymbol{d}(M,M+1)\rho^{(n_p+1)}(M+1,N;t)$$

$$-\,\boldsymbol{e}_p\boldsymbol{d}(N-1,N)\rho^{(n_p+1)}(M,N-1;t))\;. \tag{168}$$

Finally, we mention two properties of the RDM expansion coefficients which are important for the numerical solution of the QME. From the hermiticity of the density matrix it follows that $(\rho^{(n_{\rm pu},n_{\rm pr})}(M,N;t))^* = \rho^{(-n_{\rm pu},-n_{\rm pr})}(N,M;t)$, and for all times t the relation $n_{\rm pu}+n_{\rm pr}=M-N$ among the indices of $\rho^{(n_{\rm pu},n_{\rm pr})}(M,N;t)$ holds. To prove the latter statement we assume that at time $t=t_0$ no external field has acted on the system, hence the system is in its ground state characterized by the density matrix $\rho(M,N;t_0)=\rho^{(n_{\rm pu},n_{\rm pr})}(M,N;t_0)=\delta_{M,N}\delta_{M,0}\delta_{n_{\rm pu},n_{\rm pr}}\delta_{n_{\rm pu},0}$. Next, one looks at the expansion coefficients of the density matrix which are generated after an infinitesimal time step dt due to the action of the external field. From Eq. (168) it follows that only those coefficients are generated for which the above mentioned relation is fulfilled. The conservation of this relation for any time follows by successively repeating this procedure.

The relation $n_{\rm pu}+n_{\rm pr}=M-N$ allows to close the set of equations for the expansion coefficients of the RDM. The index $n_{\rm pu}$ can be expressed by the other indices and for $n_{\rm pr}$ one needs to take into account the range $n_{\rm pr}=\{-1,0,1\}$ since the weak probe field acts only in first order with respect to $H_{\rm F}$, Eq. (46). In comparison to the number of equations of motion for the complete density matrix, the number of equations of motion for the expansion coefficients is three times larger. However since in the latter equations only the envelopes of the external fields enter it can be solved with a much higher time step.

The RDM expansion can be circumvented if the RDM is propagated with different phases of the external field as it was proposed in Ref. [142]. In this manner it is possible to obtain the wave vector dependence of the polarization in a nonperturbative scheme. The propagation of the RDM, however, includes the total fields and not only the envelopes. Furthermore, the RDM has to be propagated for at least three different phases to extract the desired part of the polarization wave. Therefore, this approach could hardly manage the numerical effort involved in the investigation of the PPC dynamics discussed below.

6.3. *Linearization with respect to a weak-field part*

For further use we specify the approach to the case that via a linear expansion a certain weak-field part of the total field $\boldsymbol{E}_{\rm w}$ (low-intensity pulse) is eliminated. The remaining strong part $\boldsymbol{E}_{\rm s}$ will be considered exactly. To carry out the linearization with respect to $\boldsymbol{E}_{\rm w}$ we use the formal solution of the QME for the reduced density operator in the presence of the total field:

$$\hat\rho(t)=\mathscr{U}(t,t_0;\boldsymbol{E})\hat\rho(t_0)\equiv\mathscr{U}(t,t_0;\boldsymbol{E}_{\rm s})\mathscr{S}(t,t_0;\boldsymbol{E}_{\rm w})\hat\rho(t_0)\;. \tag{169}$$

Here, $\mathscr{U}$ denotes the complete time-evolution superoperator. In the second part of this equation we have split up this superoperator into a part where the strong field appears alone and into the S-superoperator. The latter quantity is exclusively defined via the coupling of the weak-field part to system. The Liouville-superoperator describing this coupling reads

$$\mathscr{L}_{\mathrm{w}}(t)\bullet = \frac{1}{\hbar}[-\mu_{\mathrm{PPC}}\boldsymbol{E}_{\mathrm{w}}, \bullet]_- \; . \tag{170}$$

The respective linearization of the density operator follows as

$$\hat{\rho}(t) \approx \mathscr{U}(t,t_0;\boldsymbol{E}_{\mathrm{s}})\hat{\rho}(t_0) - \mathrm{i}\int_{t_0}^{t} \mathrm{d}\bar{t}\; \mathscr{U}(t,\bar{t};\boldsymbol{E}_{\mathrm{s}})\mathscr{L}_{\mathrm{w}}(\bar{t})\mathscr{U}(\bar{t},t_0;\boldsymbol{E}_{\mathrm{s}})\hat{\rho}(t_0)\; . \tag{171}$$

The polarization induced by the weak-field part is given by

$$\boldsymbol{P}_{\mathrm{w}} = -\mathrm{i}n_{\mathrm{PPC}}\int_{t_0}^{t} \mathrm{d}\bar{t}\; \mathrm{tr}_{\mathrm{el}}\{\mu_{\mathrm{PPC}}\mathscr{U}(t,\bar{t};\boldsymbol{E}_{\mathrm{s}})\mathscr{L}_{\mathrm{w}}(\bar{t})\mathscr{U}(\bar{t},t_0;\boldsymbol{E}_{\mathrm{s}})\hat{\rho}(t_0)\}\; . \tag{172}$$

Obviously, this relation reduces to the linear response case if the strong-field part is removed. We will use this version in the next section to discuss linear optical properties of PPCs.

6.4. Linear absorption

6.4.1. Correlation function description

The linear susceptibility is obtained applying first-order perturbation theory with respect to matter light-field coupling $H_{\mathrm{F}}(t)$ as the second-rank tensor

$$\chi^{(1)}_{j\bar{j}}(t-t') = n_{\mathrm{PPC}}\frac{\mathrm{i}}{\hbar}\Theta(t-t')\mathrm{tr}\{\hat{W}_{\mathrm{eq}}[\hat{\mu}_j(t),\hat{\mu}_{\bar{j}}(t')]\}\; . \tag{173}$$

The PPC dipole operator has been introduced in Eq. (47), where $\hat{\mu}_j$ denotes the jth Cartesian vector component. The statistical operator $\hat{W}_{\mathrm{eq}}$ describes an isolated PPC. In equilibrium it will project onto the electronic ground state only, i.e. $\hat{W}_{\mathrm{eq}} = \hat{R}_{\mathrm{eq}}|0\rangle\langle 0|$, where $\hat{R}_{\mathrm{eq}}$ is the equilibrium statistical operator for the vibrational DOF. Furthermore, we tacitly assumed that inhomogeneous broadening can be neglected. The frequency-domain absorption coefficient is derived using $\alpha(\omega) = 4\pi\omega\,\mathrm{Im}\sum_j \chi^{(1)}_{jj}(\omega)/c$ (c is the speed of light in the medium). One obtains

$$\alpha(\omega) = \frac{4\pi\omega n_{\mathrm{PPC}}}{\hbar c}\;\mathrm{Re}\int_0^{\infty}\mathrm{d}t\;\mathrm{e}^{\mathrm{i}\omega t}\;C^{(2)}_{\mathrm{d\text{-}d}}(t)\; . \tag{174}$$

The absorption spectrum is completely defined by the (second-order) dipole–dipole correlation function

$$C^{(2)}_{\mathrm{d\text{-}d}}(t) = \mathrm{tr}\{\hat{W}_{\mathrm{eq}}[\hat{\mu}(t),\hat{\mu}(0)]\}\; . \tag{175}$$

Note that this expression is a scalar since the dipole operators are multiplied according to a scalar product. The trace in the correlation function can be subdivided into a trace $\mathrm{tr}_{\mathrm{vib}}$ over the vibrational DOF and a trace with respect to the electronic states. For the present purpose the time-evolution operator can be restricted to a part referring to the electronic ground and to a part related to the single-excitation manifold, i.e. $U(t) \approx U_0(t)\hat{P}_0 + U_1(t)\hat{P}_1$. Here, U_0 and U_1 are defined via $H^{(0)}_{\mathrm{PPC}}$ and $H^{(1)}_{\mathrm{PPC}}$, respectively. Therefore, we may write

$$C^{(2)}_{\mathrm{d\text{-}d}}(t) = \mathrm{tr}_{\mathrm{vib}}\{\hat{R}_{\mathrm{eq}} U_0^+(t) | \langle 0|\hat{\mu} U_1(t) P_1 \hat{\mu}|0\rangle\} - \text{c.c.} \tag{176}$$

The structure of Eq. (176) follows from the assumption that the dipole operators do not contain diagonal contributions with respect to the electronic states.

It is well-known (see, e.g. [57]) that the linear absorption spectrum of a chromophore complex can be calculated analytically if one neglects either the dipole–dipole interaction J_{mn} or the electron–vibrational coupling. To include both types of coupling requires to use approximation schemes (see e.g. [143,144]). For this purpose, we concentrate on the resonant contributions to Eq. (176) and split up $H^{(1)}_{\mathrm{PPC}}$ into a perturbation $\hat{V}$ and an unperturbed part $\mathscr{H}_0$. Then, one can introduce a subdivision of the time-evolution operator according to $U_1(t) \equiv \exp(-\mathrm{i}\mathscr{H}^{(1)}_{\mathrm{PPC}} t/\hbar) = U_1^{(0)}(t) S(t,0)$. Here, $U_1^{(0)}(t)$ is the time-evolution operator defined by $\mathscr{H}_0$, and the S-operator reads

$$S(t,0) = T \exp\left(-\frac{\mathrm{i}}{\hbar} \int_0^t \mathrm{d}\tau\, \hat{V}^{(\mathrm{I})}(\tau) \right) \tag{177}$$

with $\hat{V}^{(\mathrm{I})}(\tau) = U_1^{(0)+}(\tau) \hat{V} U_1^{(0)}(\tau)$. After fixing the partitioning of $\mathscr{H}^{(1)}_{\mathrm{PPC}}$ the relations given above offer a convenient way to carry out a (low-order) perturbation expansion. Accordingly, the dipole–dipole correlation function reads (note that Eq. (48) defines the transition dipole operators)

$$C^{(2)}_{\mathrm{d\text{-}d}}(t) = \mathrm{tr}_{\mathrm{vib}}\{\hat{R}_{\mathrm{eq}} U_0^+(t) \hat{\mu}_{0,1} U_1^{(0)}(t) S(t,0) P_1 \hat{\mu}_{1,0}\} . \tag{178}$$

For the case where the EVC is much weaker than J_{mn} one has to carry out a perturbation expansion in J_{mn} setting $\hat{V} = \sum_{mn} J_{mn} |m\rangle\langle n|$ and using the site-representation for the electronic states

$$C^{(2)}_{\mathrm{d\text{-}d}}(t) = \sum_{mn} \boldsymbol{d}^*_m(eg) \boldsymbol{d}_n(eg) \mathrm{tr}_{\mathrm{vib}}\{\hat{R}_{\mathrm{eq}} U_0^+(t) U_m(t) \langle m|S(t,0)|n\rangle\} . \tag{179}$$

The zeroth-order contribution in J_{mn} results in the trace-expression $\mathrm{tr}_{\mathrm{vib}}\{\hat{R}_{\mathrm{eq}} U^\dagger_{m,g}(t)\, U_{m,e}(t)\}$ giving the absorption as the sum of monomeric correlation functions which are known from molecular spectroscopy. Within the displaced oscillator model adopted for the EVC the trace can be calculated analytically yielding $\exp(-\mathrm{i}\omega_{eg} t - G_m(0) + G_m(t))$, with the so-called lineshape function

$$G_m(t) = \int_0^\infty \mathrm{d}\omega (\mathrm{e}^{-\mathrm{i}\omega t}(1 + n(\omega)) + \mathrm{e}^{\mathrm{i}\omega t} n(\omega)) \mathscr{J}_m(\omega) . \tag{180}$$

The single-molecule spectral density $\mathscr{J}_m(\omega)$ is the diagonal part of the spectral density introduced in Eq. (126).

In the context of PPC it is more instructive, however, to consider the possibility of a perturbation theory with respect to the EVC. In Section 4.3.1, we have seen that in the exciton eigenstate representation one can define excitonic PES. Transitions between different PES then correspond to energy relaxation in the one-exciton band. Suppose that this relaxation can be treated perturbatively, the expansion allows to compute corrections to an absorption coefficient which is determined exclusively by the single-exciton PES. To this end, one has to change from the site-representation to the representation with respect to the single exciton states $|\alpha_1\rangle$. In a first step, we switch from the excitonic PES to the single-exciton energies E_{α_1}. Then, the perturbation operator is given by the complete EVC $\hat{V}(\tau) = \sum_{\alpha,\beta} \sum_\xi \hbar\omega_\xi g_\xi(\alpha_1, \beta_1) Q_\xi(\tau) |\alpha_1\rangle\langle\beta_1|$ (cf. Eq. (73)). Expanding the S-operator (177) in powers of $\hat{V}$ introduces vibrational satellites to the pure excitonic absorption spectrum which is given by $\alpha(\omega) = 4\pi^2\omega n_{\mathrm{PPC}}/\hbar c \times \sum_{\alpha_1} |\boldsymbol{d}(\alpha_1, 0)|^2 \delta(\omega - E_{\alpha_1}/\hbar)$. The transition dipole matrix elements are given in Eq. (55).

In a next step, one generalizes this description by replacing the pure electronic energies E_{α_1} by excitonic PES U_{α_1} such that the diagonal EVC has been accounted for exactly. Only the off-diagonal part $g_\xi(\alpha_1, \beta_1)$, $\alpha \neq \beta$, needs to be considered as a perturbation $\hat{V}$. We introduce $U_{\alpha_1}(t) = \exp\{-\mathrm{i}(T_{\mathrm{vib}} + U(\alpha_1))t/\hbar\}$ defined with the single-exciton Hamiltonian, Eq. (45), and obtain the correlation function as

$$C^{(2)}_{\mathrm{d\text{-}d}}(t) = \sum_{\alpha\beta} \boldsymbol{d}^*(\alpha_1, 0)\boldsymbol{d}(\beta_1, 0)\mathrm{tr}_{\mathrm{vib}}\{\hat{R}_{\mathrm{eq}} U_0^+(t) U_{\alpha_1}(t) \langle\alpha_1|S(t, 0)|\beta_1\rangle\} . \tag{181}$$

If one neglects the S-operator the trace-expression becomes diagonal with respect to the exciton quantum number and the single-exciton PES contribution reads $\mathrm{tr}_{\mathrm{vib}}\{\hat{R}_{\mathrm{eq}} U_0^+(t) U_{\alpha_1}(t)\} = \exp(-G_{\alpha_1}(0) + G_{\alpha_1}(t))$ with the lineshape function similar to Eq. (180), but with the spectral density $\mathscr{J}_{\alpha_1}(\omega)$ instead of $\mathscr{J}_m(\omega)$. The newly introduced spectral density $\mathscr{J}_{\alpha_1}(\omega)$ can be obtained from the general type, Eq. (119), after specifying this expression to the single-exciton case and to a single-exciton quantum number ($\alpha_1 = \beta_1 = \gamma_1 = \delta_1$).

Calculating the absorption spectrum in zeroth-order, all excitonic levels contribute independently from the other levels. But in contrast to the approximation of the rigid PPC the absorption lines are broadened due to the inclusion of the vibrational DOF. In Ref. [76] it has been argued that the neglect of relaxation processes (described by the off-diagonal part of $g_\xi(\alpha_1, \beta_1)$) is justified whenever static disorder tends to localize the excitations. For localized excitations according to Mott the spatial overlap between wave function overlap having comparable energies vanishes, i.e., the relaxation rates between energetically close states will be rather small.

6.4.2. Reduced density matrix description

In the case of weak or intermediate EVC the perturbation theory introduced at the end of the foregoing section is appropriate to compute the PPC frequency domain absorption spectrum. We give here an alternative formulation which makes use of the exciton RDM [85,86]. In doing so there is no need to formulate the perturbation theory with respect to the EVC since this has been already done when deriving the QME. We start with expression (172) to come into contact with linear absorption for the absence of the strong field $\boldsymbol{E}_{\mathrm{s}}$. The derived expression for the linear susceptibility can be translated into the dipole–dipole correlation function

$$C^{(2)}_{\mathrm{d\text{-}d}}(t) = \mathrm{tr}_{\mathrm{el}}\{\hat{\mu}_{\mathrm{PPC}} \mathscr{U}(t) [\hat{\mu}_{\mathrm{PPC}}, |0\rangle\langle 0|]_-\} . \tag{182}$$

It contains the (dissipative) propagation of the commutator between the electronic equilibrium statistical operator $|0\rangle\langle 0|$ and the PPC dipole operator. The propagation has to be carried out according to the QME as indicated by the time-propagation superoperator $\mathscr{U}(t)$.

In order to write Eq. (182) in the representation of the single-exciton states we set (in analogy to retarded Green's functions, $\Theta(t)$ denotes the unit-step function)

$$G_{\alpha_1}(t) = \Theta(t)\langle\alpha_1|\mathscr{U}(t)[\hat{\mu}_{\mathrm{PPC}},|0\rangle\langle 0|]_-|0\rangle \ . \tag{183}$$

The absorption follows according to Eq. (174) as

$$\alpha(\omega) = \frac{4\pi\omega n_{\mathrm{PPC}}}{\hbar c}\,\mathrm{Re}\sum_{\alpha_1}(\boldsymbol{d}^*(\alpha_1,0)G_{\alpha_1}(\omega) + \boldsymbol{d}(\alpha_1,0)G^*_{\alpha_1}(-\omega)) \ . \tag{184}$$

From the non-Markovian QME (97) we obtain an equation of motion for $G_{\alpha_1}(t)$ which reads (note that $t_0 = 0$ and that the integration goes to infinity according to the introduction of the unit step function)

$$\frac{\partial}{\partial t}G_{\alpha_1}(t) = \delta(t)\boldsymbol{d}(\alpha_1,0) - \mathrm{i}\Omega_{\alpha_1}G_{\alpha_1}(t) - \frac{1}{\hbar^2}\sum_{\beta,\gamma_1}\int_0^\infty \mathrm{d}\tau\, C(\alpha_1,\beta_1,\beta_1,\gamma_1;\tau)\mathrm{e}^{-\mathrm{i}\Omega_{\beta_1}\tau}G_{\gamma_1}(t-\tau) \ . \tag{185}$$

Transforming this expression into the frequency domain gives (cf. Eq. (114), $\Omega_{\alpha_1} = E_{\alpha_1}/\hbar$)

$$-\mathrm{i}(\omega - \Omega_{\alpha_1})G_{\alpha_1}(\omega) = \boldsymbol{d}(\alpha_1,0) - \frac{1}{\hbar^2}\sum_{\beta_1,\gamma_1}\tilde{C}(\alpha_1,\beta_1,\beta_1,\gamma_1;\omega_1 - \Omega_{\beta_1})G_{\gamma_1}(\omega) \ . \tag{186}$$

If we neglect all elements of $\tilde{C}(\alpha_1,\beta_1,\beta_1,\gamma_1;\omega)$ where γ_1 is different from α_1 it follows that

$$G_{\alpha_1}(\omega) = \frac{\mathrm{i}\boldsymbol{d}(\alpha_1,0)}{\omega - \Omega_{\alpha_1} + (\mathrm{i}/\hbar^2)\sum_{\beta_1}\tilde{C}(\alpha_1,\beta_1,\beta_1,\alpha_1;\omega - \Omega_{\beta_1}) + \mathrm{i}\varepsilon} \tag{187}$$

and the absorption spectrum becomes (nonresonant contributions have been neglected)

$$\alpha(\omega) = \frac{4\pi\omega n_{\mathrm{PPC}}}{\hbar c}\sum_{\alpha_1}|\boldsymbol{d}(\alpha_1,0)|^2\frac{\Gamma(\alpha_1,\omega)}{(\omega - \Omega_{\alpha_1} - \Sigma(\alpha_1,\omega))^2 + \Gamma^2(\alpha_1,\omega)} \ . \tag{188}$$

Here, the complex self-energy is given by

$$\Sigma(\alpha_1,\omega) + \mathrm{i}\Gamma(\alpha_1,\omega) = -\frac{\mathrm{i}}{\hbar^2}\sum_{\beta_1}\tilde{C}(\alpha_1,\beta_1,\beta_1,\alpha_1;\omega - \Omega_{\beta_1}) \ . \tag{189}$$

Eq. (188) shows that the effect of EVC is two-fold: the spectrum is renormalized ($\Sigma(\alpha_1,\omega)$) and broadened ($\Gamma(\alpha_1,\omega)$). Both effects are state-specific, i.e., they depend on the coupling matrix $g_\xi(\alpha_1,\beta_1)$. The frequency dependence of the self-energy expresses the non-Markovian character of the underlying dynamics. Replacing ω by Ω_{α_1} in $\Gamma(\alpha_1,\omega)$ (Markovian limit) and neglecting $\Sigma(\alpha_1,\omega)$, a Lorentzian-type spectrum is obtained

$$\alpha(\omega) = \frac{4\pi\omega n_{\mathrm{PPC}}}{\hbar c}\sum_{\alpha_1}|\boldsymbol{d}(\alpha_1,0)|^2\frac{\Gamma(\alpha_1)}{(\omega - \Omega_{\alpha_1})^2 + \Gamma^2(\alpha_1)} \tag{190}$$

with the dephasing rates $\Gamma(\alpha_1)$ already introduced in Eq. (132). An iteration of the EVC which goes beyond the one used to derive the QME has been given recently in [145].

6.5. Nonlinear optical properties

6.5.1. Third-order response function

The formalism based on the third-order susceptibility $\chi^{(3)}$ is well established and has been extensively discussed for molecular systems in Ref. [57]. As long as the considered molecular system can be described by a set of levels coupled in a diagonal manner to vibrational DOF one can derive an expression for $\chi^{(3)}$ which is beyond any perturbation theory with respect to the coupling to the vibrational DOF. This is achieved by using a cumulant expansion. The result for $\chi^{(3)}$ becomes exact if the vibrational DOF are characterized by parabolic PES [57]. In Section 4.3.1, we mapped the PPC excitations onto such a model by introducing excitonic PES. Unfortunately, there remain off-diagonal contributions to the multi-exciton vibrational coupling. However, neglecting this contribution (compare Eq. (83)) one can follow the derivation of Ref. [79] to obtain closed expressions.

According to Mukamel [57] one can relate $\chi^{(3)}$ to the nonlinear response function using the relation

$$\boldsymbol{P}(\boldsymbol{r},t) = \int_0^\infty \mathrm{d}t_1\,\mathrm{d}t_2\,\mathrm{d}t_3\, R(t_1,t_2,t_3)\boldsymbol{E}(\boldsymbol{r},t-t_1)\boldsymbol{E}(\boldsymbol{r},t-t_1-t_2)\boldsymbol{E}(\boldsymbol{r},t-t_1-t_2-t_3)\,. \tag{191}$$

The response function $R(t_1,t_2,t_3)$ has the following structure (here specified to the case of no inhomogeneous broadening):

$$\begin{aligned} R(t_1,t_2,t_3) = 2n_{\mathrm{PPC}}^4 \,\mathrm{Re}(&C^{(4)}_{\mathrm{d\text{-}d}}(t_1,t_1+t_2,t_1+t_2+t_3,0) \\ &+ C^{(4)}_{\mathrm{d\text{-}d}}(0,t_1+t_2,t_1+t_2+t_3,t_1) + C^{(4)}_{\mathrm{d\text{-}d}}(0,t_1,t_1+t_2,t_1+t_2+t_3) \\ &+ C^{(4)}_{\mathrm{d\text{-}d}}(t_1+t_2+t_3,t_1+t_2,t_1,0))\,, \end{aligned} \tag{192}$$

where the fourth-order dipole–dipole correlation function is given by

$$C^{(4)}_{\mathrm{d\text{-}d}}(t_1,t_2,t_3,t_4) = \mathrm{tr}\{\hat{W}_{\mathrm{eq}}\,\hat{\mu}_{\mathrm{PPC}}(t_1)\,\hat{\mu}_{\mathrm{PPC}}(t_2)\,\hat{\mu}_{\mathrm{PPC}}(t_3)\,\hat{\mu}_{\mathrm{PPC}}(t_4)\}\,. \tag{193}$$

The arrangement of the vectorial dipole operators has to be understood in the sense of dyadic products leading to a fourth-rank correlation tensor. $\hat{W}_{\mathrm{eq}} = \hat{R}_{\mathrm{eq}}|0\rangle\langle 0|$ describes the ground state of the PPC with the vibrational equilibrium statistical operator $\hat{R}_{\mathrm{eq}}$. The time-dependence of the PPC dipole-operators, Eq. (47) is defined by the complete PPC Hamiltonian (see Eq. (1) or Eq. (B.28)). Obviously the fourth-order dipole–dipole correlation function only contains contributions from the single- and the two-exciton manifold. Using the notation introduced in Eq. (50) we obtain

$$\begin{aligned} C^{(4)}_{\mathrm{d\text{-}d}}(t_1,t_2,t_3,t_4) = \mathrm{tr}_{\mathrm{vib}}\{\hat{R}_{\mathrm{eq}}\langle 0|&\hat{\mu}_{0,1}(t_1)\hat{\mu}_{1,0}(t_1)\hat{\mu}_{0,1}(t_3)\hat{\mu}_{1,0}(t_4) \\ &+ \hat{\mu}_{0,1}(t_1)\hat{\mu}_{1,2}(t_1)\,\hat{\mu}_{2,1}(t_3)\hat{\mu}_{1,0}(t_4)|0\rangle\}\,. \end{aligned} \tag{194}$$

In this expression, the various time-dependencies are given by the PPC Hamiltonian $H^{(N)}_{\mathrm{PPC}}$ for the ground state and the first two excited exciton manifolds

$$\hat{\mu}_{N,M}(t) = \exp\{\mathrm{i}H^{(N)}_{\mathrm{PPC}}t/\hbar\}\hat{\mu}_{N,M}\exp\{-\mathrm{i}H^{(M)}_{\mathrm{PPC}}t/\hbar\}\,. \tag{195}$$

The fourth-order dipole–dipole correlation function $C^{(4)}_{\mathrm{d-d}}$ can be calculated according to standard procedures (see, e.g., [53,57]) if one uses the Hamiltonian $H^{(N)}_{\mathrm{PPC}}$ $(N = 0, 1, 2)$ in the multi-exciton representation (Eq. (77) or Eq. (83)), but neglects the off-diagonal multi-exciton vibrational coupling, i.e. $g_\xi(\alpha_N, \beta_N) = 0$ if $\alpha \neq \beta$. It has been discussed in Section 4.3.1 under what conditions this approximation becomes possible. Furthermore, we note that the analytical determination of $C^{(4)}_{\mathrm{d-d}}$ relies on the harmonic oscillator model for the PPC vibrations. In this case, the correlation function is obtained as a certain combination of the PPC spectral density of the type introduced in Eq. (120):

$$C^{(4)}_{\mathrm{d-d}}(t_1, t_2, t_3, t_4) = \sum_{\alpha_1, \beta_1} \Bigg(\boldsymbol{d}(0, \alpha_1)\boldsymbol{d}(\alpha_1, 0)\boldsymbol{d}(0, \beta_1)\boldsymbol{d}(\beta_1, 0)$$
$$\times \exp(-\mathrm{i}\Omega_{\alpha_1}(t_3 - t_4) - \mathrm{i}\Omega_{\beta_1}(t_1 - t_2) + G(\alpha_1, \beta_1; t_1, t_2, t_3, t_4))$$
$$+ \sum_{\gamma_2} \boldsymbol{d}(0, \alpha_1)\boldsymbol{d}(\alpha_1, \gamma_2)\boldsymbol{d}(\gamma_2, \beta_1)\boldsymbol{d}(\beta_1, 0)$$
$$\times \exp(-\mathrm{i}\Omega_{\alpha_1}(t_3 - t_4) - \mathrm{i}\Omega_{\beta_1}(t_1 - t_2) - \mathrm{i}\Omega_{\gamma_2}(t_2 - t_3))$$
$$\times \exp(\tilde{G}(\alpha_1, \beta_1, \gamma_2; t_1, t_2, t_3, t_4)) \Bigg) . \tag{196}$$

The two newly introduced functions $G(\alpha_1, \beta_1; t_1, t_2, t_3, t_4)$ and $\tilde{G}(\alpha_1, \beta_1, \gamma_2; t_1, t_2, t_3, t_4)$ are determined by the type of correlation functions introduced in Eq. (118). Explicit expressions for G and $\tilde{G}$ have been given in Ref. [79]. The derivation shows that the description of the nonlinear optical response in the model of harmonic multi-exciton PES and using the nonlinear response function, Eq. (192), has a number of advantages. First, the expression does not involve any perturbation theory with respect to the diagonal part of the EVC. Such a perturbation theory was indeed the basis for the derivation of the multi-exciton QME in Section 5.1.3. Second, the nonlinear response function does not contain any assumption with respect to retardation effects in the EVC (no Markov approximation). And, the neglect of the off-diagonal multi-exciton vibrational coupling necessary to get the exact expression for the nonlinear response function [79] can be circumvented as explained in [81]. The nonlinear response function approach has been applied to simulated photon echo and pump–probe experiments on PPCs.

6.5.2. *Ultrafast pump–probe spectroscopy*

In a pump–probe experiment the absorption of a weak probe pulse in the presence or after the action of a strong pump pulse is measured. In this respect, the dependence of the absorption on the delay time τ_{d} between the two pulses is of most interest. The probe-pulse absorption can be related to the respective energy loss $S^{(\mathrm{pr})}$. This quantity is obtained from Eq. (165) if restricted to the probe field E_{pr} and the related polarization $P^{(\mathrm{pr})}$. But the latter has to be determined in dependence on the pump- field envelope E_{pu}. Accordingly, the differential absorption can be calculated as follows

$$\frac{\Delta\alpha}{\alpha_0} = \frac{S^{(\mathrm{pr})}(E_{\mathrm{pu}}, E_{\mathrm{pr}}, \tau_{\mathrm{d}}) - S^{(\mathrm{pr})}(E_{\mathrm{pu}} = 0, E_{\mathrm{pr}})}{S^{(\mathrm{pr})}(E_{\mathrm{pu}} = 0, E_{\mathrm{pr}})} , \tag{197}$$

where $S^{(\mathrm{pr})}(E_{\mathrm{pu}} = 0, E_{\mathrm{pr}})$ is proportional to the linear absorption measured by the probe pulse alone. To determine $S^{(\mathrm{pr})}$ one can use an approach based on the third-order response function (see Section 6.5.1). Alternatively, one can apply the technique based on the partial wave expansion of the density operator as given in Eq. (159). In both cases one has to chose for $S^{(\mathrm{pr})}$ the time-integrated expression (165), and, in particular, the term referring to $p = \mathrm{pr}$, i.e. the probe-beam contribution. Furthermore, n has to be identified with ($n_{\mathrm{pu}} = 0, n_{\mathrm{pr}} = 1$), resulting in the properly oscillating polarization part according to the expansion Eq. (163). Additionally, the transmitted probe-pulse may be dispersed in a monochromator, thus obtaining an increased frequency resolution. Here, instead of a single detector one has to assume that there is a detector for each Fourier component E_ω of the probe field.

6.5.3. Photon echo spectroscopy

Photon echo techniques have been described in detail, for example, in the Refs. [57,79,81,109,138, 146–150]. In the case of stimulated (three-pulse) photon echo three different pulses are applied

$$\begin{aligned} \boldsymbol{E}(\boldsymbol{r},t) = {} & E_1(t)\exp\{\mathrm{i}(\boldsymbol{k}_1\boldsymbol{r} - \omega_1 t)\} + E_2(t)\exp\{\mathrm{i}(\boldsymbol{k}_2\boldsymbol{r} - \omega_2 t)\} \\ & + E_3(t)\exp\{\mathrm{i}(\boldsymbol{k}_3\boldsymbol{r} - \omega_3 t)\} + \text{c.c.}\,, \end{aligned} \tag{198}$$

delayed by τ and T. At time τ after the action of the third pulse one can detect in the direction $\boldsymbol{k}_1 - \boldsymbol{k}_2 - \boldsymbol{k}_3$ the echo signal whose characteristic decay gives access to the PPC dephasing times. To see, how the observed echo signal is related to the correlation function of the electronic excitation energies of the pigments we consider in the following the model used before to describe linear absorption (Section 6.4.1, note the change of the time-arguments). The descriptiom is based on the assumption of weakly interacting pigments and uses the site representation. Neglecting the coupling between the pigments the third-order polarization which determines the echo signal reads

$$\begin{aligned} P(t) = {} & \frac{1}{(\mathrm{i}\hbar)^3}\int_{t_0}^{t}\mathrm{d}\tau\int_{t_0}^{\tau}\mathrm{d}\tau_1\int_{t_0}^{\tau_1}\mathrm{d}\tau_2\; E_3(\tau)E_2(\tau_1)E_1(\tau_2)\exp\{-\mathrm{i}\omega(t-\tau-\tau_1+\tau_2)\} \\ & \times\sum_{mn}|\boldsymbol{d}_m(e,g)|^2|\boldsymbol{d}_n(e,g)|^2\,\mathrm{tr}_{\mathrm{vib}}\{\hat{R}_{\mathrm{eq}}U_0^+(\tau_1)U_m(\tau_1)U_m^+(t)U_0(t)U_0^+(\tau)U_n^+(\tau)U_n(\tau_2)U_0^+(\tau_2) \\ & + \hat{R}_{\mathrm{eq}}U_0^+(\tau)U_m(\tau)U_m^+(t)U_0(t)U_0^+(\tau_1)U_n^+(\tau_1)U_n(\tau_2)U_0^+(\tau_2)\}\,. \end{aligned} \tag{199}$$

Here we have assumed the same carrier frequencies for the three pulses, i.e. we set $\omega_1 = \omega_2 = \omega_3 = \omega$. The time evolution operators U_m of the excited states are the same as used in Eq. (179). Since here we are calculating a nonlinear polarization we obtain four-point dipole correlation functions. However, as suggested in [57] these four-point functions can be expressed by two-point correlation functions within a cumulant expansion. For the discussion below it is appropriate to take the impulsive limit, i.e. to set $E_3(t) = A\delta(t)$, $E_2(t) = A\delta(T + t)$, and $E_1(t) = A\delta(T + \tau + t)$. After performing an average over the inhomogeneous distribution of the pigment's transition energies one obtains an analytical result for the echo signal $\propto |P(t)|^2$, reading

$$\begin{aligned} |P(t)|^2 \propto {} & \sum_{mn}|d_m(e,g)|^4|d_n(e,g)|^4\{(1-\delta_{mn})\mathrm{e}^{-2\sigma_{\mathrm{inh}}^2(t-\tau)^2} + \delta_{mn}\mathrm{e}^{-\sigma_{\mathrm{inh}}^2(t-\tau)^2}\} \\ & \times\exp\{-2(2G^{(1)}(0) - G^{(1)}(\tau) + G^{(1)}(t+T+\tau) \end{aligned}$$

$$
\begin{aligned}
&- G^{(1)}(T+\tau) - G^{(1)}(T+t) + G^{(1)}(T) - G^{(1)}(t))\} \\
&\times \cos^2\{G^{(2)}(T) + G^{(2)}(t) - G^{(2)}(T+\tau) - G^{(2)}(0)\}\,. \qquad (200)
\end{aligned}
$$

As a consequence of the applied cumulant expansion the complex lineshape function $G(t) = G^{(1)}(t) + \mathrm{i}G^{(2)}(t)$ appears (compare Eq. (180)). For simplicity, we have assumed equal EVC for all pigments, i.e. the the lineshape function is assumed to be independent on the site indices m and n.

The exponential term in the first line of Eq. (200) contains the half-width σ_{inh} of the inhomogeneous distribution of pigment energies. This term after all is responsible for the occurrence of an echo at $t = \tau$. In this way, the inhomogeneous contribution to the overall dephasing of coherences can be eliminated and the echo decay in dependence on τ is a direct measure of the homogeneous dephasing described here by the complex lineshape function $G(t)$. Hence, we expect a decay of the echo signal with increasing values of τ. As it has been pointed out in [109] the integrated three-pulse photon echo signal has its maximum at slightly higher values of τ and this so-called three-pulse photon echo peak shift (from the value $\tau = 0$) depends on the time delay T between the second and third pulse. As it could be demonstrated numerically [109] and analytically [146] the peak shift function in dependence on T is direct proportional to the lineshape function $G(T)$. This offers a direct way from photon echo experiments to the spectral density of the proteins.

Another attractive feature of three-pulse photon echo experiments is that the period in which the system resides in a population state (during T) rather than in a polarization state can be large. Thus, changes in the population on very different time scales can be investigated extending from femtosecond energy transfer [147,149,150] up to conformational motion monitored by spectral diffusion of the pigments transition energies [44]. Finally, we note that our standard picure given above does include neither of these processes. It is, however, straightforward, to introduce a S operator which treats the dipole–dipole interactions between the pigments in perturbation theory. As it has been investigated in [147,149,150] the interpigment transfer destroys the echo signal for large population periods T. Furthermore, our qualitative picture also did not treat higher excited states of the aggregate. We will investigate this point in Section 9.3 where it will be discussed how photon echo experiments can be used to investigate the two-exciton manifold. (Note, that in a two-pulse photon echo experiment the second and third interaction of the system with the light field happens at once. This situation can be described by setting $T = 0$ in Eq. (200).)

6.5.4. Green's function approach to nonlinear susceptibilities

An alternative description of the nonlinear optical response is provided by the equation of motion approach. Here a closed set of Heisenberg equations of motion for exciton creation and annihilation operators are is derived (cf. Appendix D). This technique lends itself to develop a Green's function formulation of nonlinear optical spectroscopy in PPCs [137]. For an PPC of three-level systems it has been shown in Ref. [151] that in the limit of negligible pure dephasing the third-order nonlinear optical susceptibility can be expressed as

$$
\begin{aligned}
\chi^{(3)}(-\omega_s;\omega_1,\omega_2,\omega_3) = &-\frac{1}{6}\sum_{perm}\sum_{m_s,m_1,m_2,m_3} \boldsymbol{d}_{m_s}\boldsymbol{d}_{m_1}\boldsymbol{d}_{m_2}\boldsymbol{d}_{m_3}\sum_{mn} G_{m_s m}(\omega_s)G^{*}_{mm_2}(-\omega_2) \\
&\times \bar{\Gamma}_{mn}(\omega_1+\omega_3)G_{nm_1}(\omega_1)G_{nm_3}(\omega_3) + \mathrm{c}'.\mathrm{c}'. \qquad (201)
\end{aligned}
$$

Here $\omega_s = \omega_1 + \omega_2 + \omega_3$ and c′.c′. stands for complex conjugation and changing of the signs of all frequencies $\omega_j \to -\omega_j$ $(j = 1, 2, 3)$. Further, *perm* denotes the sum over all permutations of pairs (m_j, ω_j). Furthermore, the expression contains the single-exciton Green's function $G_{nn}(\omega)$, Eq. (D.11), as well as the exciton scattering matrix

$$\bar{\Gamma}_{mn}(\omega) = [F(\omega)]^{-1}_{mn}[(\hbar\omega + g_n)\kappa_n^2 - 2\hbar\omega] \tag{202}$$

with

$$F_{mn}(\omega) = \delta_{mn}\kappa_m^2 - [(\hbar\omega + g_m)\kappa_m^2 - 2\hbar\omega]\mathscr{G}_{mn}(\omega) \; . \tag{203}$$

Here, the zero-order two-exciton Green's function

$$\mathscr{G}_{mn}(\omega) = \int \frac{\mathrm{d}\omega'}{2\pi \mathrm{i}} F_{mn}(\omega') F_{mn}(\omega - \omega') \tag{204}$$

has been introduced. The parameter κ_n is the ratio between the transition dipoles $d_{eg}^{(n)}$ and $d_{fe}^{(n)}$ and $g_n = 2\hbar(\Omega_{nf}/\kappa_n^2 - \Omega_{n,e})$. The structure of the two-exciton scattering matrix, Eq. (202), reflects the roles of statistics and anharmonicities in the optical nonlinearities. Obviously, $\bar{\Gamma}(\omega)$ reduces to the two-level limit with Pauli statistics $(\kappa_n = 0)$ [137] as well as to the limit of a three-level anharmonic oscillator with Bose statistics ($\kappa_n = \sqrt{2}$, anharmonicity g_n). Calculating the susceptibility using Eq. (201) has the advantage that there is no need to diagonalize the exciton Hamiltonian. Moreover, due to the local nature of the commutation relations for the Pauli operators the exciton scattering matrix is not a tetradic $N^2 \times N^2$ but a $N \times N$ matrix. The incorporation of weak EVC and static disorder within the two-level limit has been provided in [137].

7. The LH2 of purple bacteria

In this section we discuss some results on the dynamics of excitons in the peripheral antenna complex of purple bacteria. The photosynthetic apparatus of purple bacteria is fully incorporated into the cell membrane. Every photosynthetic unit organizes about 300 BChl molecules within the antenna aggregates. The so-called core (LH1) complex has circular geometry with the reaction center in its middle [24]. In addition, BChl*a* containing complexes have a second peripheral antenna system, the so-called LH2, which is also of circular geometry. Several LH2 complexes are assumed to surround the LH1 in a way to provide effective connectivity for energy transfer [19,65]. High-resolution structural data have been obtained for *Rps. acidophila* [4] and *Rs. molischianum* [152].

Both complexes consist of $\alpha\beta$ protein pairs arranged in eight-fold (*Rs. molischianum*) and nine-fold (*Rps. acidophila*) symmetry forming concentric rings with the α/β polypeptides inside/outside. The basic unit of such a circular aggregate is shown in Fig. 6. Every $\alpha\beta$ pair noncovalently binds three BChl*a* molecules and two carotenoids. In Fig. 6 only one carotenoid molecule is shown, the second one could only partly be resolved. The bacteriochlorophylls are arranged in two rings. The BChls in the upper layer with large inter pigment distances of about 21 Å are called the B800 pigments according to their absorption maximum at 800 nm. Their macrocycles are roughly

Fig. 6. Basic unit of the LH2 antenna. The α-helices of the two proteins binding the BChl are shown together with a B800 pigment, two B850 pigments and a single carotenoid.

parallel to the membrane plane. The lower layer consists of more densely packed B850 bacteriochlorophylls (with nearest-neighbor distances of 9 Å) absorbing at 850 nm. Their macrocycles are approximately perpendicular to the membrane plane. The structurally resolved carotenoid molecule in a basic unit comes into close contact to all three BChls (< 10 Å) indicating its role in light-harvesting, energy transfer, and triplet quenching. A full view of the LH2 of *Rps. acidophila* is given in Fig. 7.

The unravelling of the atomic structure of the LH2 for *Rps. acidophila* [4] and *Rs. molischianum* [152] has placed this system into the focus of experimental and theoretical investigations [19,20,153,154]. Its unique structure inhabits dipole–dipole interactions spanning a wide range of magnitudes. This is reflected in a multitude of time scales for excitation energy transfer. Since the LH2 of *Rps. acidophila*, for instance, comprises 27 BChl*a* molecules, the theoretical analysis will be restricted to the case of weak EVC. We first discuss the linear absorption spectrum together with the localization properties of the one-exciton wave function. This will provide us with a parameter set which is used to address the B800 and B850 intraband and the B800–B850 interband transfer dynamics in the context of nonlinear optical spectroscopy.

7.1. Linear absorption and wave function localization

The expression for the linear absorption coefficient has been given in Eq. (190). Even though microscopic structural data are available for the LH2 complex, monomeric transition energies as

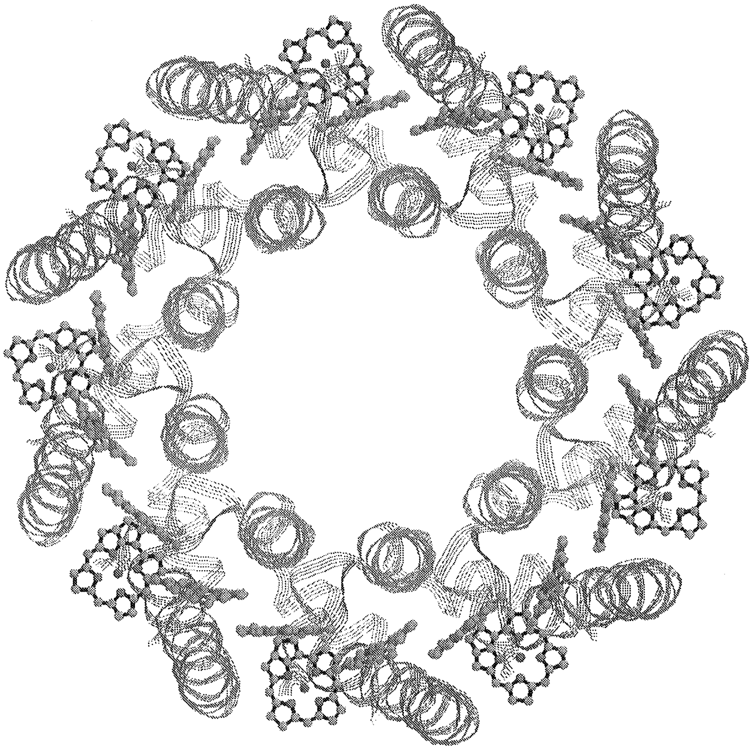

Fig. 7. Schematic view of the LH2 antenna with the bacteriochlorophyll molecules, of which only the porphyrine planes are shown. The pigment molecules form two rings which are stabilized by proteins (figure courtesy of T. Pullerits).

well as the mutual interactions between the pigments are not unambiguously defined. Particularly, the interaction energies reported in literature scatter quite considerably ranging from below 300 cm^{-1} [62,70], to about 400 cm^{-1} [67] up to about 800 cm^{-1} [65,71]. These numbers reflect the different approaches to the calculation of J_{mn} as well as different parameters used to characterize the dielectric properties of the protein environment and for the monomeric transition dipole moments (cf. Section 3). The different assumptions can only be tested by comparing the simulated optical response with experimental observations. Since static and dynamic disorder are contributing to the optical spectra as well, different techniques have to be compared to establish reasonable parameters for the exciton–vibrational Hamiltonian Eq. (72). In the following we will explore the linear optical properties of the LH2 first.

The calculated linear absorption spectrum of the 18 pigment B850 ring of an LH2-type system is shown in Fig. 8 using the interaction matrix of Ref. [67] which was derived from the *Rps. acidophila* structure [4]. The solid curve shows the stick spectrum for the isolated case, i.e., neglecting static and dynamic disorder. In this case the energy levels E_{α_1} take 10 distinct values. The states at the upper and lower band egde are nondegenerate, whereas the states inside the band are grouped into pairs of identical energy. Because of the ring-like structure and because the dipoles are almost in the

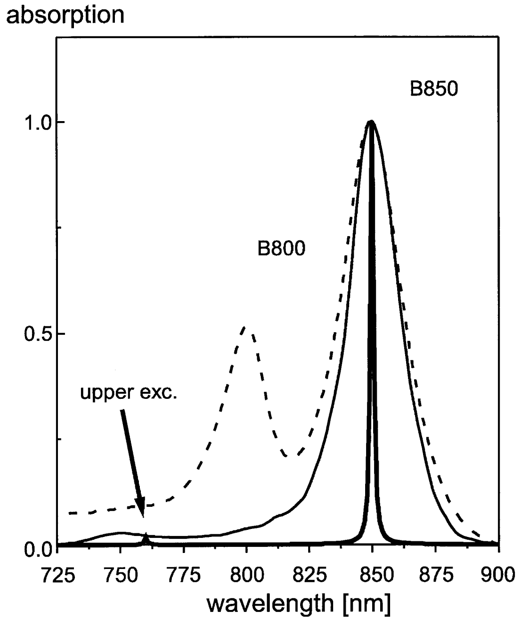

Fig. 8. Linear absorption spectrum of LH2 of *Rb. sphaeroides* at room temperature. The dashed line shows the experimental result (data courtesy of J. Herek) while the solid lines corresponds to the calculated spectrum for the isolated B850 pigment pool (thick line) and the homogeneously and inhomogeneously broadened case (thin solid line).

plane of the ring, the lowest (nondegenerate) exciton state does not carry oscillator strength. Except from a small contribution which comes from the upper band edge of the one-exciton manifold, most oscillator strength is concentrated in the first pair of degenerate states above the lower band edge. This situation changes upon inclusion of static disorder as can be seen from the thin solid curve in Fig. 8. Oscillator strength is distributed over several states at the upper and lower band edges (for a detailed discussion of the effect of static disorder on circular aggregates see [155]). The calculation further includes the effect of dynamic disorder at room temperature which adds to the total broadening of the individual exciton states according to Eq. (190). For the spectral density entering the dephasing rate, Eq. (132), we have used form (129) with $p = 2$ and $\mathcal{J}_0 = g^2/2\omega_c^3$ (cf. [64]). The correlation radius in Eq. (128) has been set to zero, i.e. $f(Z_{mn}) = \delta_{mn}$. Further, fluctuations of the dipole–dipole coupling have been neglected and the diagonal EVC was described by a single parameter g (In addition, a pure dephasing term like $c^{(\mathrm{II})}$ in Eq. (C.8) has been added (for details see Ref. [64]).). For the given parameter set ($\omega_c = 50\,\mathrm{cm}^{-1}$, $g\hbar\omega = 100\,\mathrm{cm}^{-1}$) the agreement with the experimental spectrum taken at room temperature (dashed line in Fig. 8) for the B850 band is rather good.

Having specified the one-exciton Hamiltonian one can characterize the one-exciton wave function using the concept of the inverse of the so-called participation ratio defined as

$$L(E) = \frac{1}{N D(E)} \left\langle \sum_{\alpha_1} \delta(E - E_{\alpha_1}) \left[\sum_n C^4_{n,\alpha_1} \right] \right\rangle_{\text{disorder}} \tag{205}$$

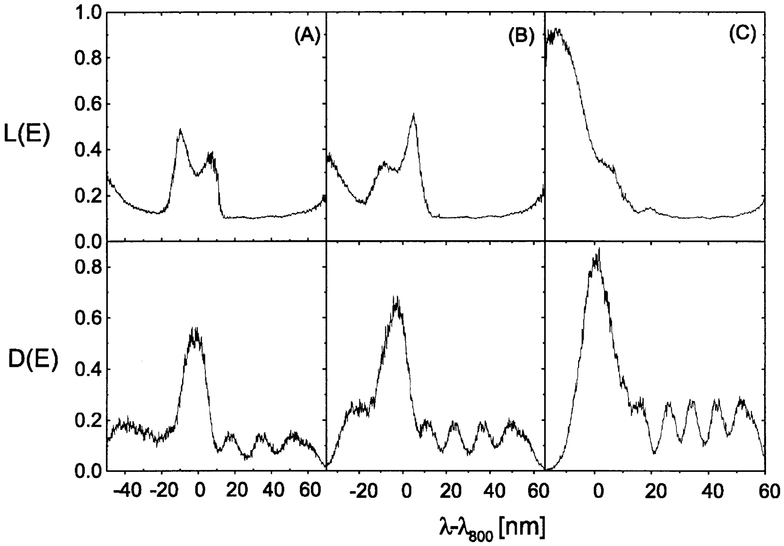

Fig. 9. Participation ratio Eq. (205) (upper panel) and density of states Eq. (206) (lower panel) for LH2. The scaling factor for dipole–dipole coupling is 1.0 (A), 0.75 (B), and 0.5 (C). (Note that the wavelength scale is different in the different panels.)

with the excitonic density of states given by

$$D(E) = \frac{1}{N}\left\langle \sum_{\alpha_1} \delta(E - E_{\alpha_1}) \right\rangle_{\text{disorder}} \tag{206}$$

and N is the number of pigments. We note in caution that $L(E)$ is a static quantity entirely specified by the solutions of the stationary Schrödinger equation. Since dynamic disorder is not taken into account, the coherence domain size $N_{\text{coh}} = L^{-1}(E)$ has to be viewed as an upper boundary to the "real" value (see below). In addition, one should keep in mind that $L(E)$ always resembles the symmetry of the system, i.e. for a linear aggregate, for instance, one has $N_{\text{coh}} = 2(N + 1)/3$ and not $N_{\text{coh}} = N$.

In Fig. 9 we explore the effect of a scaling of the dipole–dipole coupling matrix of Ref. [67] on the participation ratio and the density of states for the LH2. Let us discuss the density of states. First, we notice that the overall bandwidth depends on the maximum coupling strength, $\text{Max}|J_{mn}|$, an effect which is more pronounced for the B850 pigment pool. Decreasing the coupling strength from panel (A) to (C) leads to an increase of $D(E)$ at the blue edge of the LH2 absorption band due to the overlap between B800 and B850 states. In fact, both types of pigments are coupled and "tuning" the upper band edge of the B850 band into resonance with the B800 band has strong implications on the inter- and intraband transfer dynamics as we will see below. We further notice that $D(E)$ is quite structured in the region where only B850 excitations contribute to the spectrum. As noted before a consequence of the circular symmetry of the B850 system is that energy levels occur mostly in degenerate pairs (except the lowest and the highest one) which are split up due to the static disorder. The lowest exciton state can be identified as the weak shoulder on the red edge of the density of states in Fig. 9.

Next, we focus on the participation ratio $L(E)$ (upper panel in Fig. 9) which gives an estimate for the static coherence domain size of the one-exciton states. From Fig. 9 we see that exciton states located at the band edges tend to be more localized than states within the energy band. If we focus on case (C) in Fig. 9, for example, we calculate from $L(E)$, $N_{\mathrm{coh}} \approx 10$ sites around 850 nm and $N_{\mathrm{coh}} \approx 3$ sites around 800 nm. Note that the coherence domain size around 800 nm appears to be larger than for the B800 only pigment system where it is about 1.6 [63]. This is another consequence of the mixing between both types of pigments in this wavelength region.

7.2. Pump–probe spectroscopy

The presence of different ranges of coupling strengths in the LH2 system results in a rich dynamics taking place on a multitude of time scales. Let us consider the B800 pigment pool first which is weakly coupled because of the large separations between the pigments (cf. Fig. 7). The fastest time scale for intraband dynamics has been found to increase from 0.3 to 0.6 ps upon tuning the excitation wavelength in a one-colour pump–probe measurement from the blue to the red of the B800 band at 77 K [156]. Similar results were obtained in Ref. [157]. Two-colour experiments performed at 19 K gave a 0.4 ps rise time for the photobleaching/stimulated emission signal at 805 nm after excitation at 783 nm [158]. The most striking feature of the B800 intraband dynamics, however, is that it appears to be impossible to describe the two-colour pump–probe data and the hole-burning results simultaneously without introducing an additional decay channel for B800 excitations. Small and co-workers proposed in this respect a model in which exciton levels of the B850 band located at the upper band edge mediate the energy relaxation within the B800 band [158]. This type of upper excitonic state has been suggested by the excitonic calculations reported in Ref. [70]; it is clearly seen as a feature in the absorption profile of the B850 ring in Fig. 8. Recent measurements of the circular dichroism in B800-free mutants of *Rb. sphaeroides* provided clear indications for this upper excitonic feature which is located to the blue of the B800 band at around 780 nm [159]. Frequency-domain nonlinear optical spectroscopy of the same type of mutant, on the other hand, suggested the upper excitonic state to be at about 800 nm [160].

In Ref. [63] the B800 intraband and B800–B850 interband dynamics has been investigated using the set of density matrix equations (115) reduced to the one-exciton manifold. For the EVC a stochastic model had been chosen (cf. Section 4.2). In order to explore the influence of B850 pigments on the B800 dynamics, simulations with different coupling matrices were performed such that the position of the upper excitonic state was gradually tuned in resonance with the B800 absorption maximum (cf. Fig. 9). Further, explicit expressions for a quenching matrix entering the equations of motion and describing unidirectional energy flow according to the spectral overlaps were derived. Using this setup the following results were established: The fast intraband dynamics as observed by Hess et al. [156] could only be explained by including, besides the direct B800–B800 transfer, the "detour" via B850 pigments as shown in Fig. 10. At first glance this process seems to be rather improbable for it involves transfer over a large spatial distance. However, if the upper excitonic state (or the upper excitonic band in the case of static disorder) deriving from the B850 pool is in resonance with the B800 states it provides an efficient bridge (with rather delocalized states) for mediating this transfer. We note in passing that in the presence of off-diagonal dynamic disorder, i.e. a stochastic fluctuation of the coupling matrix J_{mn}, it is not necessary for the (bridge)

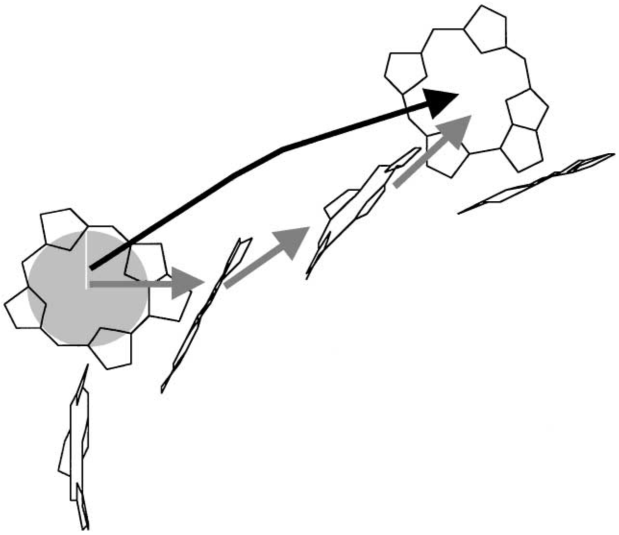

Fig. 10. Possible pathways of energy flow for B800 intraband transfer. As the consequence of the upper excitonic states, indirect transfer where the B850 pigment pool acts as an effective bridge becomes possible (light-gray arrows). The direct path between two B800 pigments is shown as a black arrow.

B850 exciton states to carry oscillator strength in order to participate in this process [161]. (The possibility of transfer to optically forbidden states has also been discussed in Refs. [82,145].) Of course, the position of the upper excitonic state as well as the possibility of dark state transfer has also a strong impact on the B800–B850 interband transfer. This process takes place on a time scale of 0.7 ps at room temperature [162] and slows down to about 1.5 ps at low temperatures [157,163]. Information on these time scales can be obtained already from the population dynamics. In Fig. 11 we show the wavelength-resolved populations across the B800–B850 absorption band after selective excitation of the B800 band for EVC parameters as in Fig. 8. A consistent fit of intra- and interband dynamics suggested a maximum dipole–dipole coupling strength between 200 and $300\,\mathrm{cm}^{-1}$. Thus, the upper exciton state is located between 780 and 800 nm. This is in good agreement with the results of hole burning [158], circular dichroism [159], and nonlinear absorption [160].

Next, we focus on the B850 intraband dynamics which, as a consequence of the strong dipole–dipole coupling, is more suitably described as energy relaxation within the delocalized one-exciton band [20,64]. Early two-colour pump–probe investigations on *Rb. sphaeroides* using 200 fs pulses by Savikhin et al. [164] indicated intraband transfer on a 80–100 fs time scale at room temperature which slowed down to 250–300 fs at 19 K. Room temperature measurements at higher time resolution resulted in relaxation time scales of about 100 fs and anisotropy decay times of about 30 fs [165]. Further, it was found that excitation at the blue side of the B850 absorption peak leads to a dynamic red shift and a decrease in amplitude of the signal. On the other hand, there are a number of experiments suggesting two sub-picosecond time scales at cryogenic temperatures [111,166,167]. Lowering the temperature to 7 K a small red shift was found even for excitation at 880 nm [166].

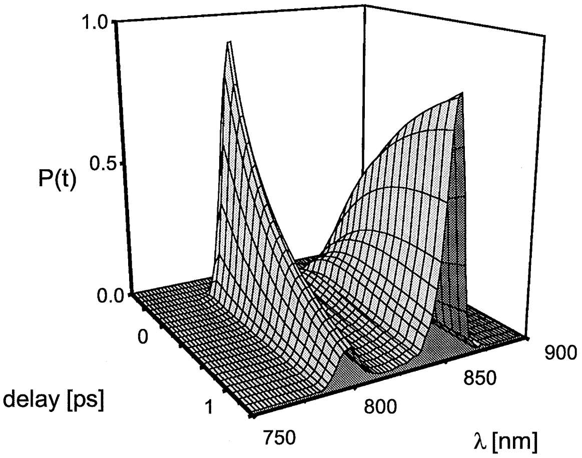

Fig. 11. Population dynamics within the LH2 like system after excitation in the B800 band (for parameters see text).

These observations are in general in accord with the picture of exciton relaxation. However, the details of the dynamics in the red edge of the B850 band appear to be quite complicated. Low-temperature hole-burning studies gave evidence for a so-called B870 exciton level being $200\,\mathrm{cm}^{-1}$ below the B850 band maximum of *Rps. acidophila* [168] (cf. also recent Stark hole burning data on various photosynthetic antennae in Ref. [169]). On the other hand, it has been demonstrated by Chachisvilis and co-workers [161] that at low temperature a new band splits off to the red the B850 band and continues to move on the time scale of some tens of picoseconds. As a possible explanation of this long-time feature polaron formation together with a transition to a charge transfer state has been suggested in Ref. [111]. On the other hand, exciton transfer between different B850 complexes has been proposed as a source of this spectral evolution in [167].

In Ref. [64] it was shown that the quasi-equilibrium state reached after about 2 ps in a transient absorption experiment [161] can be modelled using multilevel density matrix theory, i.e. the coupled set Eqs. (115) including up to two-exciton states. The EVC characteristics was chosen as in the case of the linear absorption, Section 7.1. In this case the stationary limit of Eq. (197) can be applied to give the room temperature signal shown in Fig. 12. (Note that we have restricted ourselves to an expansion of the set of equations (168) up to third order in the field.) The calculation includes energy-relaxation-related dephasing as well as pure dephasing (see Section 7.1). Two situations are considered in Fig. 12, weak (solid line) and strong (dashed line) pure dephasing. The energy-relaxation-related dephasing rate has been adjusted to fit the experimental data (for details see Ref. [64]). Apparently, the relative importance of these relaxation mechanisms cannot be inferred from the stationary data. The most important point of Fig. 12 is that in order to reproduce the positions and relative magnitudes of the photobelaching/stimulated emission and excited state absorption features (given separately in the inset) the variance of the static disorder has to be on the order of the dipole–dipole coupling [64]. In this case one finds the average separation between the two lowest exciton states to be about $190\,\mathrm{cm}^{-1}$ which is in good agreement with

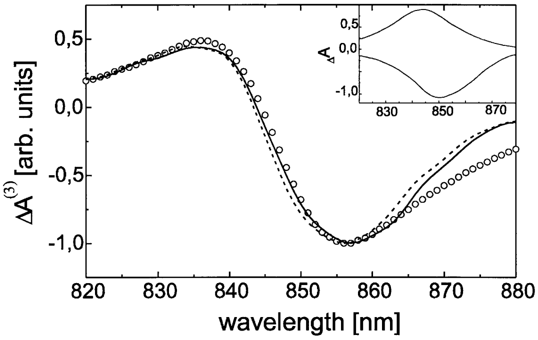

Fig. 12. Quasi-stationary room temperatures transient absorption signal for the B850 system considered in Fig. 8: solid – weak pure dephasing, dashed – strong pure dephasing, circles – experiment [161]. The inset shows the separate contribution from ground state bleaching plus stimulated emission and excited state absorption (for parameters see text).

the value estimated from low-temperature hole-burning [168]. Thus, Fig. 12 strongly supports the conjecture that the energy level structure of LH2 is subject to significant static fluctuations of the transition energies [20,64].

Finally, we note that the simulations of the quasi-stationary absorption spectra included a higher excited monomeric S_n state [64] (cf. Appendix A) with a detuning of 100 cm^{-1} and a ratio between the monomeric transition dipole moments of $d_{fe}^{(m)}/d_{eg}^{(m)} = 0.5$ [67]. Anisotropy measurements indicated that the dipoles for both transitions in monomeric BChl*a* are likely to be tilted by an angle $< 20^\circ$ with respect to each other [170]. This, however, does not have a considerable effect on the results shown in Fig. 12, i.e. parallel intramolecular dipoles can be used as long as $d_{fe}^{(m)}/d_{eg}^{(m)}$ is not much larger than unity. For $d_{fe}^{(m)}/d_{eg}^{(m)} > 1.5$, however, the mixing between molecular double excitations and collective double-excitations results in a dramatic modification of the two-exciton manifold [151]. However, in this case the ESA peak would gradually be shifted to the red contradicting the experimental data.

In Ref. [151] it was shown that frequency-domain pump–probe spectroscopy provides direct access to the two-exciton band and therefore might be amenable to address the question of the relative importance of intramolcular excited state absorption. In Ref. [151] the collective excitonic oscillator approach of Appendix D was used to calculate the two-photon absorption signal from the Green's function expression for the susceptibility given in Eq. (201) as $W_{\mathrm{TPA}} = \mathrm{Im}\,\chi^{(3)}(-\omega_2;\omega_1,-\omega_1,\omega_2)$. The structure of the two-exciton band is probed by fixing the pump frequency off-resonant to the one-exciton band and tuning the probe frequency through the two-exciton band.

7.3. Exciton relaxation and delocalization

The strong interaction between the pigments in the B850 band of LH2 or in LH1 suggests that the delocalization of the excitonic wave function plays a pivotal role for the understanding of the spectroscopy of these systems [67,154]. Strictly speaking, the collective behavior of the exciton dynamics, as manifested in the size of the exciton coherence domain, is no static property. An initially prepared coherent superposition of delocalized states, i.e., an excitonic wave packet, will dephase due to static and dynamic disorder and the exciton will be localized.

Nevertheless, this dynamic character is often neglected and the focus is put on the static properties of the exciton wave function. In this case by the participation ratio defined in Eq. (205) provides a means for addressing this problem. For example, in Ref. [171] the exciton coherence domain size for the B850 ring was estimated to be about 5. Recently, Novoderezhkin and co-workers presented a detailed study of this subject for the core light-harvesting antenna of *Rps. viridis* [155]. The definition of the participation ratio does not include the effect of dynamic disorder although there has been generalization of this concept for an infinite temperature model in Ref. [172]. (This approach has been applied in Ref. [173] to extract a delocalization length of about 3–4 pigments from three-pulse photon echo data.) On the other hand, the degree of delocalization can be accessed directly from spectroscopic data. For example, simulations of quasi-stationary absorption spectra using fragments of the B850 ring yielded $N_{\mathrm{coh}} = 4 \pm 2$ [67]. (For a discussion of the relation between pump–probe spectra and delocalization lengths see also Ref. [174].) In Ref. [175] the superradiance enhancement factor was analyzed to give emitting dipole strengths of 2.8 for LH2 at 4 K temperature. This value which is also almost independent of temperature could only be explained by assuming static disorder for the site energies. A similar analysis has been given in Ref. [165]. The theoretical formulation including the effect of dynamic disorder was provided in Ref. [79], where also the relation between the superradiance enhancement factor and an exciton coherence size defined in analogy to the participation ratio but using the density matrix in the site representation was given [80]. Another alternative for addressing the issue of the coherence length is provided by imaginary time path integral simulations which allow to take into account dynamic and static disorder nonperturbatively. Using this approach Makri and co-worker found a mean coherence length of 2–3 pigments for the B850 ring at room temperature [176].

In the context of extracting coherence lengths from experimental data it should be pointed out that different experimental setups are probing particular aspects of the system's evolution. Therefore, it is no surprise that different numbers for the size of the coherence domain of the same system have been suggested (cf. discussion in Ref. [154]). For example, difference absorption [67,161,177] and fluorescence [175] indicated the exciton to be localized on a few pigments only, but steady state nonlinear absorption experiments suggested a fully delocalized excitonic wave function [178,179]. As another alternative the measurement of anisotropy related to transitions between the one − exciton and intramolecular $S_1 - S_n$ states has been suggested in Ref. [180].

In Ref. [64] it has been proposed to use the information contained in the time-dependent one-exciton density matrix to estimate the dynamic size of the exciton coherence domain. This way, static disorder and dynamic relaxation phenomena are accounted for and a direct link to the nonlinear optical response is established. This goal is achieved by defining the function

$$C_n(t) = \sum_m |\langle \rho_{m,m+n}(t) \rangle_{\mathrm{disorder}}| \tag{207}$$

which contains the one-exciton density matrix in the site representation (cf. Eq. (133)). Note that the m summation averages ρ_{mn} with respect to the whole ring thus making $C_n(t)$ independent of the particular excitation condition in a member of the inhomogeneous ensemble.

In Fig. 13 $C_n(t)$ is plotted for the B850 pigment pool of LH2. The dynamic nature of exciton localization in real space is apparent. Initially, coherences are excited which extend over the whole

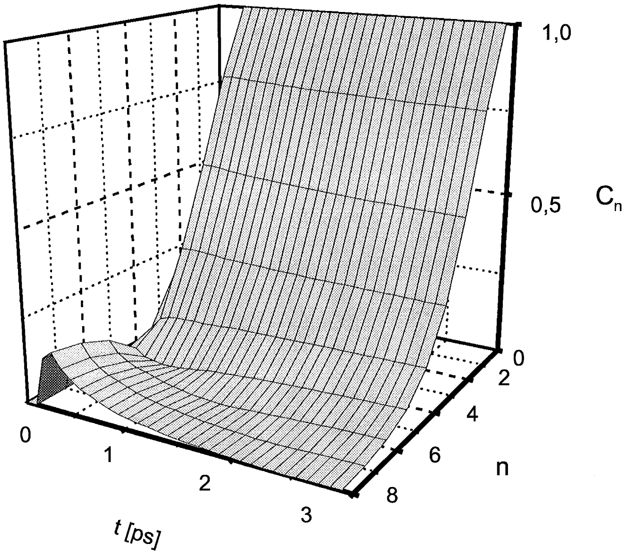

Fig. 13. Dynamics of the one-exciton coherences in a B850 system as expressed in the function $C_n(t)$ defined in Eq. (207).

ring; the shape of $C_n(t)$ reflects the behaviour of the states which contribute to the superposition state. Static and dynamic disorder then lead to a dephasing of the coherences. Notice that substantial coherences survive for about 1 ps. In the asymptotic regime an incoherent superposition of exciton eigenstates is formed:

$$C_n(\infty) \propto \sum_{m\alpha_1} C_{m,\alpha_1} C_{m+n,\alpha_1} \mathrm{e}^{-E_{\alpha_1}/k_B T} \,. \tag{208}$$

The shape of the final distribution in Fig. 13 resembles a Gaussian whose width (≈ 4) could be taken as a measure of the size of the exciton coherence domain. This width is determined by the interplay between static disorder and the Boltzmann-type population of the different exciton states. As a reference we notice that for an infinite nondisordered chain with nearest-neighbor interactions and periodic boundary condition one has the Gaussian form $C_n(\infty) \propto \exp\{-\kappa n^2 T\}$ with κ being some constant parameter [181]. In the present case, it was found [64] that the asymptotic width of $C_n(t)$ is determined mostly by the static disorder. The measure $C_n(t)$ has also been applied to the core antenna of *Rps. viridis* where the size of the coherence domain is also only a fraction of the full ring (4–9 sites) [155].

8. The FMO-complex of *Chlorobium tepidum*

The water soluble bacteriochlorophyll*a*-protein (Fenna–Mathew–Olson (FMO) complex), which forms the base plate in green sulphur bacteria *Prosthecochloris* (*Pc.*) *aestuarii* was the first pigment protein complex whose structure could be successfully analyzed by X-ray crystallography

[2] with a nominal resolution of 2.8 Å. Later Tronrud et al. [40] improved the resolution of the electron density map down to 1.8 Å. With this exceptionally high-resolution structure at hand the FMO-complex has always been considered as a key for the understanding of the microscopic processes in photosynthetic antennae.

The main light-harvesting antenna of green sulphur bacteria is formed by chlorosomes which in many respects differ from any other types of antenna systems. First, they contain the highest number of pigments. Up to 10 000 BChl*c* molecules, i.e. 95% of all the BChls in these bacteria, are bound in chlorosomes, which makes them adaptable to even extreme poor light conditions. The overall structure of chlorosomes is built from several cigar-shaped rod elements, 80 up to 200 nm long and about 10 nm in diameter. Although chlorosomes contain proteins it is not clear whether the pigments are bound to the proteins as in all other known antennae or if they form self-aggregated BChl*c* oligomers. Strong arguments in favor of a direct BChl*c*–BChl*c* bond (between central magnesium and C-9 keto carbonyl) have been provided by resonance Raman studies of Lutz et al. [182]. Besides BChl*c* chlorosomes also contain a small amount of BChl*a* which mediates the transfer of excitation energy to the base plate containing the FMO complex. The chlorosomal BChl*a* absorbs at high energies compared to the BChl*a* contained in the base plate. The funnelling of energy thus may be divided into several steps: chlorosomes (BChl*c*, 749 nm → BChl*a*, 794 nm) → base plate (FMO-complex, BChl*a*, 809 nm) → membrane (reaction center P840, BChl*a*, Fe–S). Although the FMO-complex situated in the base plate contains only a very small fraction of the pigments of the overall antenna system it acts as a bottleneck for excitation energy on its way from the outer chlorosome to the inner-membrane reaction center. The FMO-protein consists of three identical subunits arranged in three-fold symmetry. In each of the three subunits the protein backbone forms a pocket shape β-sheet with 17 strands enclosing a core of 7 BChl*a* pigments as it is shown in Fig. 14. The pigments are bound to the protein by ligation of their central magnesium atoms, and hydrogen bonding of special parts (ring I 2-acetyl group, ring V 9-keto group) of their pyrol rings. The local environments of the 7 BChls are different. Therefore the nonexcitonic shift of the pigment energies will be different.

Recently, the bacteriochlorophyll*a* antenna complex of another green bacteria *Chlorobium* (*Cb.*) *tepidum* could be resolved by Li et al. [183]. The structure very closely resembles the structure of *Pc. aestuarii*, i.e. the relative positions of the pigments are largely unchanged in the two species. Therefore, one should expect that the mutual Coulomb interactions between the pigments are not very different. However, a close examination of the tetrapyrols revealed differences in their planarity. For example the mean out-of-plane distance of the central magnesium atom of BChls in *Pc. aestuarii* is 0.48 Å whereas a much smaller value (0.09 Å) is observed in *Cb. tepidum*. There are also differences in hydrogen bonding (for a detailed comparison see [183]). Altogether these modifications in the pigment–protein interaction lead to a change in oscillator strengths of the pigment transitions as reflected in the linear absorption spectra [184,185].

The FMO-complex provides a testing ground for concepts of exciton transfer in PPCs. Its microscopic structure is well-known and its Q_y absorption band has a number of well-resolved features. Therefore, this PPC challenges level assignments and concepts for structure–function relationships. In the following we present results for the linear absorption and pump–probe spectroscopy of *Cb. tepidum* and provide evidence for an assignment of the structure in terms of a microscopic one-exciton Hamiltonian matrix according to Eq. (37).

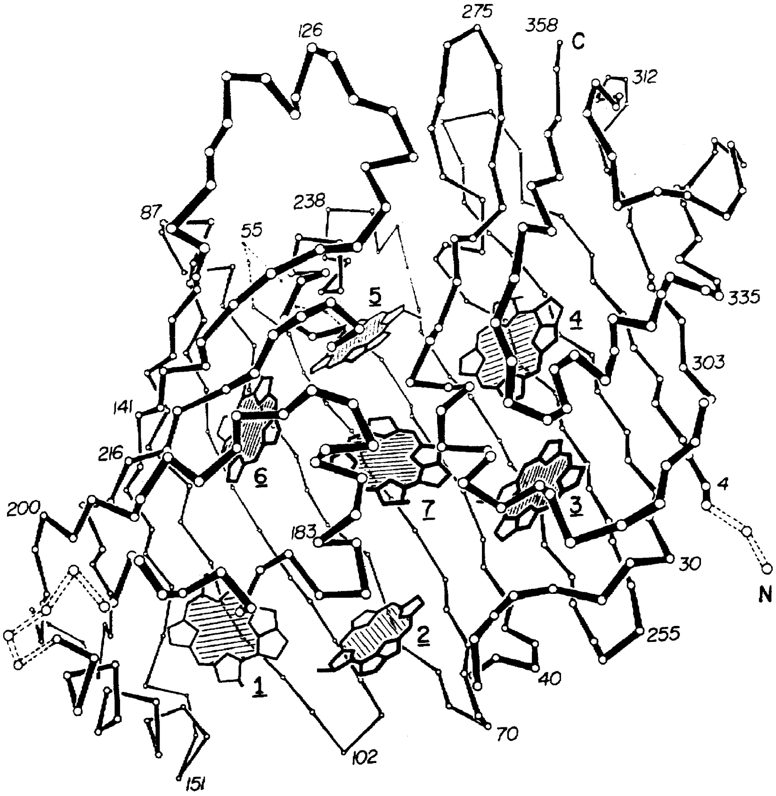

Fig. 14. FMO subunit from the base plate of *Prosthecochloris aestuarii*. The seven bacteriochlorophyll*a* molecules as well as the amino acid sequence of the protein are numbered (after [40]).

8.1. Linear spectroscopy and level assignment

The availability of highly resolved structural information and a host of spectroscopic data for the FMO-complex of *Pc. aestuarii* has triggered many efforts to establish an appropriate one-exciton Hamiltonian matrix, i.e., Coulomb interaction matrix elements and site energies entering Eq. (37) (for a discussion see [186]). From the work of Pearlstein and co-workers [187–189] it was appreciated that the different absorption bands are not solely due to Coulomb interactions but to a large extent a consequence of different site energies of BChl*a* in the protein environment. Based on a semiempirical analysis the strongest intramonomer dipole–dipole coupling was estimated to be about 190 cm^{-1}, while intermonomer interactions are as weak as 20 cm^{-1}. Using their assignment, Pearlstein et al. [188,189] were able to reproduce details of absorption and circular dichroism spectra obtained in Refs. [190,191]. Gülen proposed to assign the one-exciton Hamiltonian by fitting linear dichroism and triplet minus singlet absorption difference spectra. The resulting parameter set, however, was not suitable for reproducing circular dichroism data [192]. A reasonable fit to absorption, circular and linear dichroism, and triplet minus singlet spectra could be obtained by Louwe et al. [193] after scaling down of the dipole–dipole interaction matrix elements (strongest coupling $\sim 100\,\mathrm{cm}^{-1}$). This basically required to use an *effective* dipole strength of $28.7\,\mathrm{D}^2$ for BChl*a*.

Even though BChl*a* positions and orientations in *Pc. aestuarii* and *Cb. tepidum* are almost identical, there is only a 78% homology in the amino acid sequences [194]. As stated in Ref. [195] this may cause a different local environment for the BChl*a* molecules thus giving rise to the observed difference in the spectroscopy [195]. This effect has been accounted for in [195] in the assignment of *Cb. tepidum* by using the dipole–dipole couplings from Ref. [193] but keeping the site energies as free parameters. This way a good fit for the different spectra could be obtained at least for wavelengths above 800 nm [195] (see Table 1).

The essential feature of all theoretical assignments mentioned so far is that the EVC is only accounted for by "dressing" the excitonic stick spectra with a finite width due to the inhomogeneous and homogeneous broadening. In view of the theory presented in Section 6.4 this appears to be a strong simplification (cf. also Fig. 15 below). In Refs. [84,196] the effect of homogeneous broadening was taken into account according to Eq. (132) and on the basis of a microscopic model for the EVC as outlined in Section 5. For the spectral density the empirical form (129) has been used, with $p = -1$ and $\mathcal{J}_0 = 1/\omega_c^2$. Further only diagonal EVC was considered, i.e. $g_\xi(m,n) = \delta_{mn} g_\xi(m)$ (cf. Eq. (B.26)). For the fluctuation of the site energies a correlation radius Z_{corr} was introduced (see Eq. (128)). The 11 parameters, i.e., the seven site energies, the EVC strength which was comprised of a single parameter $gh\omega$, the cut-off frequency ω_c, the correlation radius Z_{corr}, and the inhomogeneous width of spectrum have been optimized to reproduce the linear absorption at the temperatures $T = 5$ and 107 K. Calculated and experimental spectra are compared in Fig. 15 (for parameters see Tables 1 and 2).

Having this rather good agreement it is possible to draw conclusions on the EVC. First, it has been pointed out in Ref. [84] that due to the heterogeneous energy spectrum of the FMO-complex the spectral density is "probed" at many different frequencies. In other words, linear absorption provides a sensitive test for the spectral density model. In this respect, we note that the cut-off frequency $\omega_c = 37\,\mathrm{cm}^{-1}$ is in rather good agreement with the mean frequency of the low-frequency protein vibrations ($30\,\mathrm{cm}^{-1}$) observed for *Pc. aestuarii* in Ref. [184]. The correlation radius for the EVC was found to be $Z_{\mathrm{corr}} = 21\,\mathrm{\mathring{A}}$. Since this is about the size of a FMO monomer we conclude

Table 1
Optimized site energies of the seven BChl*a*'s in the FMO monomers of *Cb. tepidum* as obtained in Refs. [84,195]. The values for *Pc. aestuarii* given in Ref. [193] are shown for comparison

BChl	$\varepsilon_m(eg)$ (eV)		
j	Ref. [84]	Ref. [195]	Ref. [193]
1	1.589	1.538	1.527
2	1.538	1.562	1.542
3	1.508	1.505	1.504
4	1.551	1.523	1.527
5	1.549	1.550	1.558
6	1.541	1.550	1.544
7	1.557	1.541	1.541

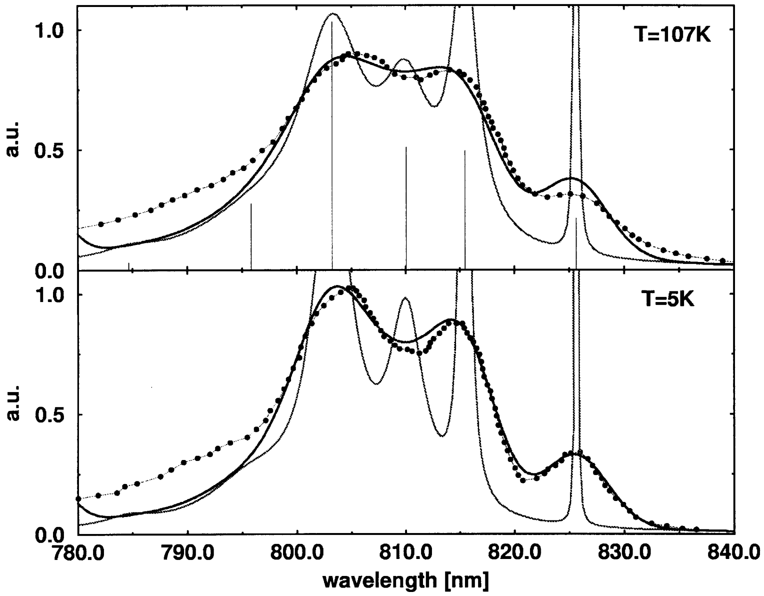

Fig. 15. Linear absorption of the FMO subunit at different temperatures. The calculated spectra for the optimized parameter set are drawn as thick lines. Thin lines show the calculated homogeneous spectra (i.e., before convoluting with a Gaussian distribution function). The points represent the experimental values measured by Freiberg et al. [185]. In the upper panel the excitonic stick spectrum is also shown (for parameters see, Tables 1 and 2).

Table 2
Single exciton energies E_{α_1}, dipole strength of the related transitions from the ground state in units of the Q_y dipole strengths of the BChls, and temperature-dependent homogeneous line widths Γ_{1N} ($T = 5\,\mathrm{K}, 107\,\mathrm{K}$) of the single-exciton levels. The parameters entering the relaxation rates density are $g\hbar\omega = 5\,\mathrm{meV}$, $\omega_c = 37\,\mathrm{cm}^{-1}$, $Z_{\mathrm{corr}} = 21\,\mathring{\mathrm{A}}$. The inhomogeneous width is obtained as $101\,\mathrm{cm}^{-1}$ (cf. Eq. (132))

N	E_{α_1} (eV (nm))	$\lvert d_{\alpha_1,0}\rvert^2$ (51 D^2)	$\Gamma_{\alpha_1}(T = 5\,\mathrm{K})$ (cm^{-1})	$\Gamma_{\alpha_1}(T = 107\,\mathrm{K})$ (cm^{-1})
1	1.502 (825.6)	0.53	0.59	1.58
2	1.520 (815.4)	1.23	5.23	20.42
3	1.531 (810.1)	1.27	29.47	43.11
4	1.544 (803.2)	2.57	32.66	56.05
5	1.558 (795.8)	0.69	75.58	98.93
6	1.580 (784.7)	0.08	42.72	46.72
7	1.598 (775.6)	0.62	0.92	0.97

that the coupled dynamics of electronic and nuclear degrees of freedom is highly correlated with respect to all BChl*a* sites in the complex.

In Table 1 we compare the site energies obtained with the present approach with the parameters of Ref. [195]. (Note that in [195] the dipole strength was chosen to be 28.7 D^2 as compared with

51 D^2 used here.) The differences are apparent and it was pointed out in Ref. [197] that the parameters of Ref. [84] do not correctly reproduce the linear dichroism spectra. On the other hand, we show that the two approaches for the calculation of linear absorption spectrum may give rather different results. These discrepancies merely demonstrate that a system as complicated as the FMO pigment–protein complex at present cannot be simulated by only a single parameter set, i.e., multiple solutions which give reasonable agreement for certain observables exist. The appropriateness of the assignment of Ref. [84] for modeling different experiments will be demonstrated in the following section.

8.2. Pump–probe spectroscopy

As a first test for the assignment established in the previous section we will simulate two-color pump–probe spectra. There has been a number of ultrafast optical experiments on the FMO-complex which invites a two-color pump–probe study where the pump pulses excite the complex in the blue of the absorption band and with the probe pulse one watches the excitation energy to sweep through the distinct bands at lower energy. According to the heterogeneous structure of the complex it is no surprise that a multitude of time scales has been observed (for a recent review see also Ref. [186]). For example, isotropic two-color measurements of *Cb. tepidum* at room temperature yielded kinetics with time scales ranging from 55–990 fs [198]. At cryogenic temperatures Buck and co-workers obtained as much as six lifetimes ranging from 170 fs to 840 ps. Similar results were reported by Freiberg et al. (see below) [185]. Interestingly, for the FMO-complex of *Pc. aestuarii* Vulto et al. found only four lifetimes (500 fs–30 ps) [199] even though both complexes are rather similar. From anisotropy measurements it was established that the early dynamics takes places in a single monomer of the trimeric FMO-complex [200]. Further, indications of excitonic quantum beats have been observed in the anisotropy data for the case that the bands at 815 and 825 nm are excited simultaneously [201].

In the following we will demonstrate that our set of parameters allows the simulation of pump–probe spectra for *Cb. tepidum* at different temperatures [84]. Our calculations will be compared with the experimental data of Ref. [185]. This requires to fix a further set of parameters which govern the monomeric excited state absorption. We use excited state transition frequencies shifted $100\,\mathrm{cm}^{-1}$ to the blue with respect to the $S_0 \rightarrow S_1$ transitions. The ratio of the transition dipole strength will be taken as a parameter.

In Fig. 16 simulations of the low-temperature two-colour (magic angle) pump–probe signals according to Eq. (197) are compared with the experimental results of Freiberg et al. [185]. In this setup the pump pulse is tuned to the absorption band at 803 nm whereas the dynamics is probed at 803, 815, and 826 nm. In order to elucidate the effect of the intramolecular S_n state curves are shown for different ratios between $S_0 \rightarrow S_1$ and $S_1 \rightarrow S_n$ transition dipole strengths $d_{fe}^{(m)}/d_{eg}^{(m)}$ (cf. Appendix A). First, we note that in contrast to the discussions in Refs. [186,197], it is obvious from Fig. 16 that intramolecular double excitations do play a role for understanding pump–probe spectra. Second, the transition dipole ratio of $d_{fe}^{(m)}/d_{eg}^{(m)} = 0.5$ appears to provide the best fit to the experimental data (note that the same value was suggested for LH2 in Ref. [67]).

The time evolution of the signal at different test wavelengths reflects the cascading of the excitation energy in the FMO-complex. For short delay times the one-color signal at 803 nm is due to pump-pulse-induced ground state bleaching and stimulated emission. The signal then partly

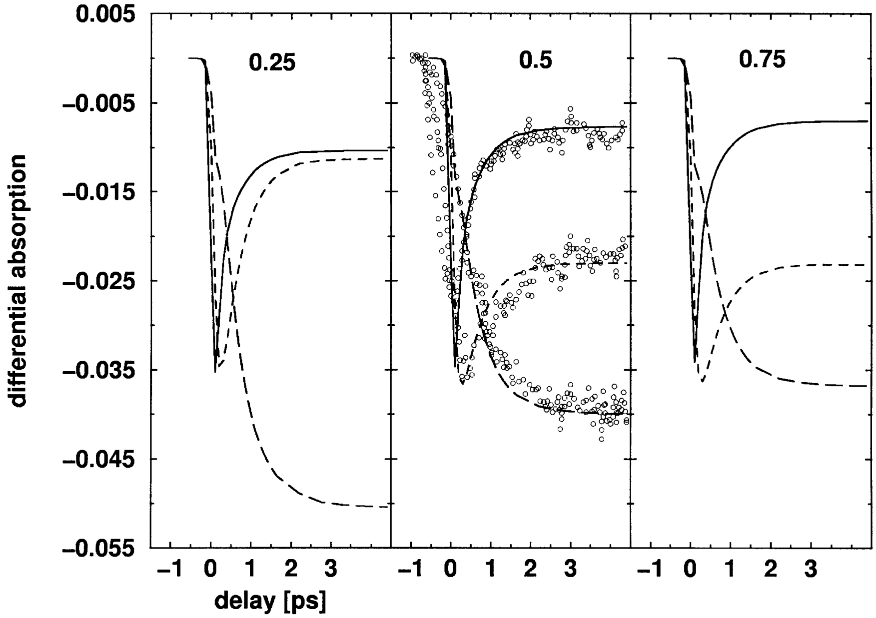

Fig. 16. Simulation of the 20 K two-color pump–probe experiments of Freiberg et al. [185] (curves with circles) at a pump wavelength of 803 nm and for different probe wavelengths. Solid curve: $\lambda_{\mathrm{pr}} = 803$ nm, dashed curve: $\lambda_{\mathrm{pr}} = 815$ nm, long dashed curve: $\lambda_{\mathrm{pr}} = 826$ nm. The three panels correspond to three different ratios of the intramolecular transition dipole moments. We have $d_{fe}^{(m)}/d_{eg}^{(m)} = 0.25$ (left), 0.5 (middle) and 0.75 (right).

decays on a 500 fs time scale. This is correlated to the population increase in the 815 nm band (increased stimulated emission). Subsequently, the 815 nm signal decays on a 2 ps time scale along with the 2 ps rise of the signal at 826 nm. The latter is due to the population of the lowest exciton state. In Fig. 17 we show the signal at 825 nm for different temperatures [196]. The good agreement with the observed behaviour [84] gives further justification for our assignment.

Next we focus on the anisotropy defined as

$$r(\tau) = \frac{\Delta\alpha_{\parallel} - \Delta\alpha_{\perp}}{\Delta\alpha_{\parallel} + 2\Delta\alpha_{\perp}} . \tag{209}$$

Here, $\Delta\alpha_{\parallel}$ ($\Delta\alpha_{\perp}$) is the differential absorption for parallel (perpendicular) polarized pump and probe pulses, and τ denotes the delay between the pulses. Of particular interest is the value of the anisotropy at zero delay, which takes the value 0.4 for randomly oriented isolated two-level systems [202]. In the case of a multi-level system this initial value of the anisotropy may become larger than 0.4. In the simplest case a multi-level system originates from the interaction between two-level systems as considered in [203], or it might represent a molecule having two optically allowed transitions with different polarizations [141,204]. Considering the FMO-complex one has a mixture of all the above-mentioned cases. There are several different transitions with different polarizations, between the ground state and the one-exciton manifold and between one- and two-exciton manifolds.

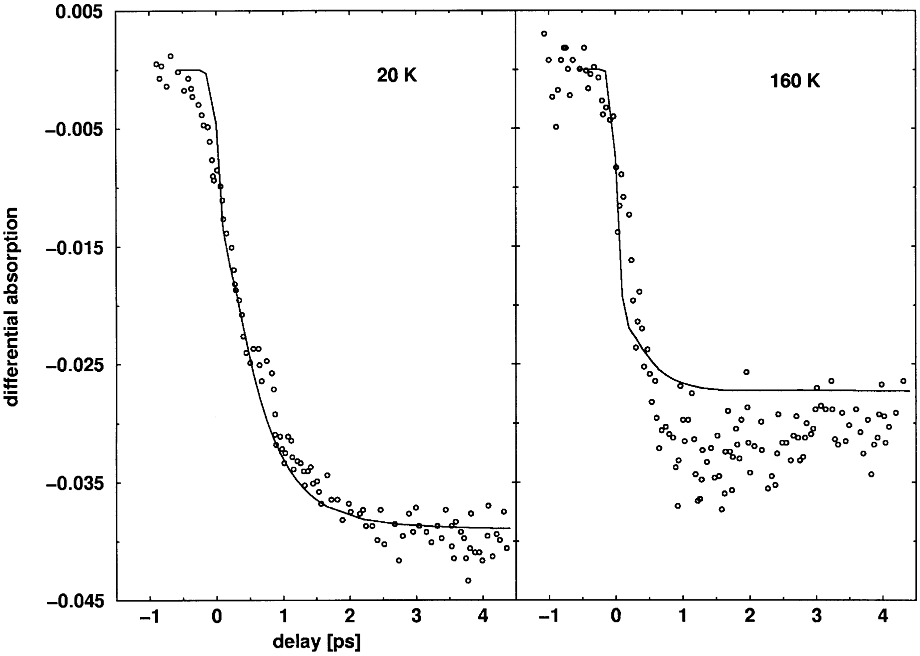

Fig. 17. Two-color pump–probe spectra at two different temperatures. Pump wavelength at 803 nm, probe wavelength at 825 nm. Experimental data of Freiberg et al. [185] are shown as circles.

In Fig. 18 we compare measured [200] and calculated [196] two-color polarized pump–probe signals as well as the related anisotropy decay. The agreement is rather good except for the anisotropy at short delay times. However, as pointed out in [141] coherent processes may lead to a strong modulation of the anisotropy when pump and probe pulse overlap. Having a closer look at the perpendicular signal in Fig. 18 for short delay times (<1 ps) one notices an oscillatory modulation. The oscillation period of 220 fs corresponds to the transition frequency between the 815 and the 826 nm one-exciton states which are simultaneously excited. Indeed, this quantum beating has been experimentally observed in Ref. [201].

To summarize, the present assignment provides a basis for simulating different nonlinear optical spectroscopies. Whether the alternative parameter set suggested by Vulto et al. [195] can give this almost quantitative agreement with the experiments remains to be shown. First simulations of prompt pump–probe spectra [205] produced reasonable results. However, the calculation of time-resolved signals using a master equation for the level populations could reproduce the experimental data at most qualitatively [166].

9. The LHC-II of green plants

A major breakthrough in the evolution of all higher organisms was the use of water as hydrogen source. The photochemical splitting of water for the evolution of oxygen made it necessary to built

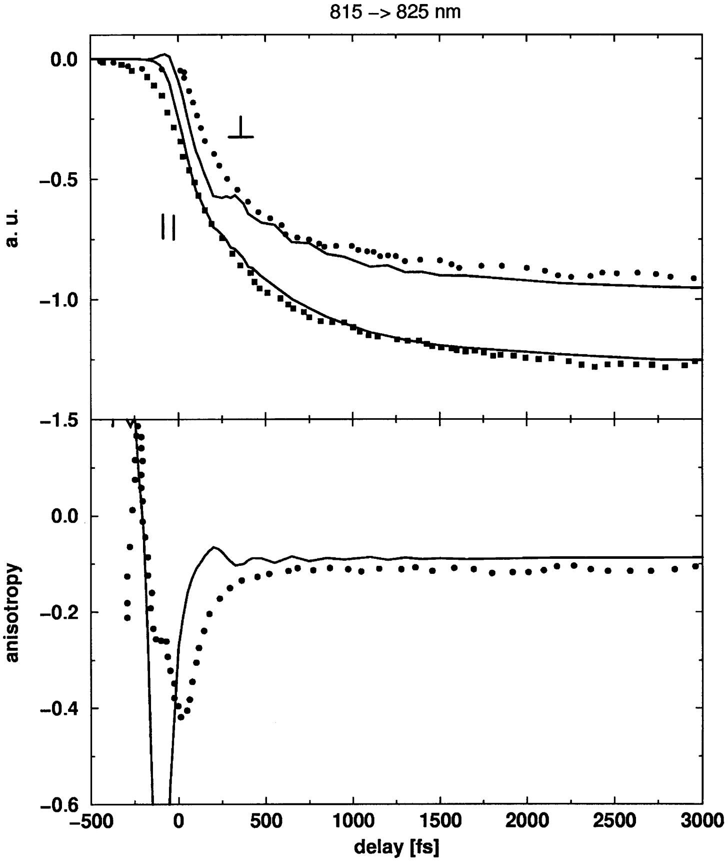

Fig. 18. Two-color anisotropy at 19 K, pump wavelength at 815 nm, probe wavelength at 825 nm. Top: Measured [200] pump–probe signals for parallel (squares) and perpendicular (circles) polarized pump and probe pulses in comparison to the theoretical curves (full lines). Bottom: Resulting anisotropy, experimental data [200]: circles, theory: full line.

up two different types of cooperating reaction centers referred to as photosystem I (PS I) and photosystem II (PS II). The two photosystems are supplied with energy by two different types of light-harvesting complexes, LHC-I and LHC-II, respectively. The LHC-II is the major photosynthetic antenna on earth. It contains roughly half of all photosynthetic active pigments of plants. It is fully incorporated in the photosynthetic membrane. Between the LHC-II and the PS-II reaction center smaller core antenna complexes are situated which mediate the transfer of excitation energy (for a recent review on PS II energy transfer see [206]). The core antennae only contain Chl*a*, whereas the LHC-II also incorporates Chl*b* which absorbs at slightly higher energies, thus increasing the absorption cross section of the reaction center. One important LHC-II function therefore is, besides a spatial transfer, also a spectral relaxation of high energetic excitations from Chl*b* to Chl*a* which is energetically close to the reaction center. A detailed understanding of this process, of course, requires the knowledge of the microscopic structure of the LHC-II. Since 1994 this structure is known with a resolution of 3.4 Å from electron diffraction experiments of Kühlbrandt et al. [3]. Similar to the FMO-complex also in the case of LHC-II a trimeric

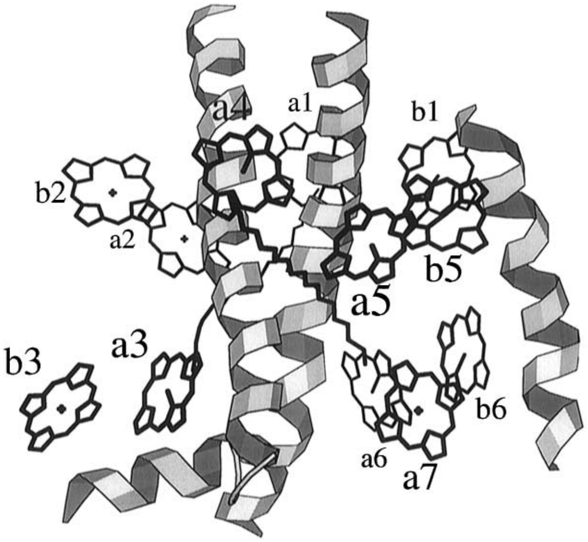

Fig. 19. LHC-II monomer according to Kühlbrandt et al. [3]. The membrane-spanning α helices hold seven pigments in the vicinity of two carotenoids (in the center) which were assigned to Chl*a*. The remaining pigments are likely to be Chl*b*.

arrangement of identical subunits has been found. Each monomer (compare Fig. 19) contains three membrane-spanning α helices, two carotenoids (xantophylls) and 12 Chls. Even though the obtained resolution did not allow for an identification of the different Chls, physiological arguments have been used to give a preliminary assignment for Chl*a* and Chl*b*. In the vicinity of seven Chls carotenoids were found which act as triplet-quenchers for the Chls to prevent the generation of singlet oxygen. Since energy transfer from Chl*b* to Chl*a* is very fast the intersystem crossing to the Chl-triplet states will take place at Chl*a*. Therefore, the above-mentioned seven Chls were assigned to Chl*a* (labeled a_1 to a_7 in Fig. 19). Based on this assignment minimal distances between nearest Chls as short as 8–10 Å were found within pairs of Chl*a* and Chl*b*. Recently (see [207] and references therein), it has been suggested that the original assignment of Chls must be changed slightly such that Chla_6 switches its identity with Chlb_5. Very recently a study on LHC-II mutants challenged this model [208]. It was concluded that the original assignment of the Chlb_5 as a Chl*b* was correct, but that the Chlb_3 is likely to be a Chl*a*.

In the remainder of this section we will first consider the linear absorption based on the exciton model with weak EVC (cf. Section 6.4.2). With respect to the Chl assignments the original Kühlbrandt model [3] and a model suggested by Gradinaru et al. [207] will be compared. Then we review results obtained for an effective vibrational mode dimer model in a pump–probe setup. Finally, we comment on two-photon two-exciton spectroscopy of this complex.

9.1. Level assignment and exciton–vibrational coupling

In Fig. 20 we show the linear absorption spectrum at different temperatures (upper panel) consisting of two main bands around 650 and 676 nm which are believed to originate from the Chl*b*

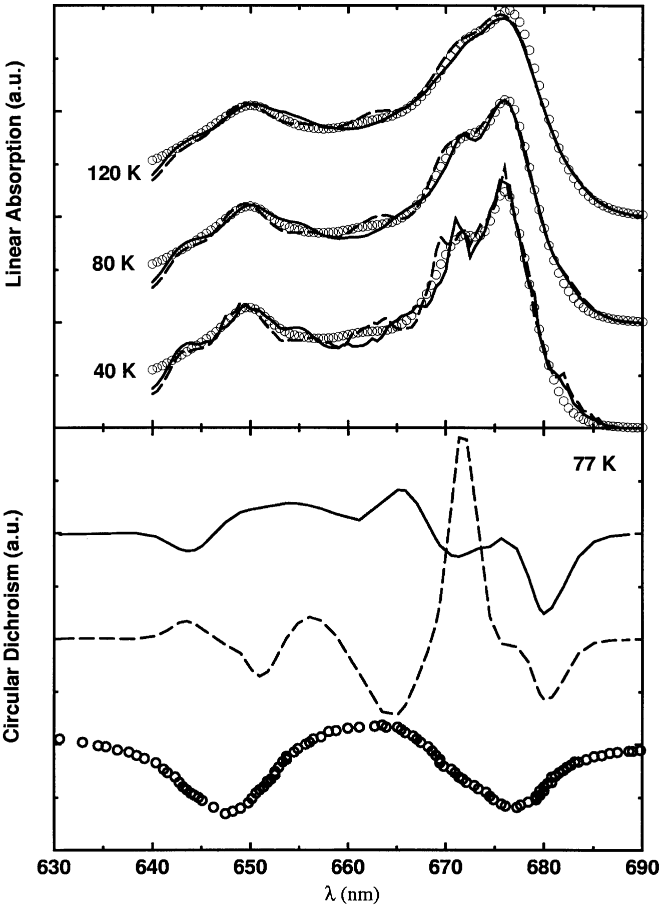

Fig. 20. Linear absorption (upper panel) and circular dichroism (lower panel) spectrum of LHC-II (after [85]). The linear absorption of the LHC-II is shown for three different temperatures and within two structural models. Dashed line: Kühlbrandt model [3]. Solid line: modified Kühlbrandt model (Chl$a_6 \leftrightarrow b_5$). The circles give the experimental values of Voigt and Schrötter [238]. The sharp features in the 40 K spectra are due to the finite ensemble size (1000) used for the statistical average. The 77 K circular dichroism spectra calculated within the two models is compared to experimental values of Nussberger [239] (circles).

and Chl*a* pigment pool, respectively. There have been several attempts to assign spectral features to chlorophyll $S_0 \rightarrow S_1$ transition energies. Linear and circular dichroism spectra (lower panel of Fig. 20) suggested the positions of nine chlorophyll transitions [209], placing the lowest transition at 676 nm. Recent nonphotochemical hole-burning studies refined this finding suggesting the lowest Chl*a* absorption to be at about 680 nm [42,210]. It should be noted that the position of this lowest state changes upon aggregation of the LHC-II trimers as suggested in [211]. The theoretical modeling of these findings is complicated due to the low resolution of the structural data. Several attempts have been made to assign monomeric transition energies, pigment–pigment coupling strengths, and orientations of the transition dipoles [85,86,207,212–214]. When interpreting optical experiments one is also faced by the general problem which lies in an appropriate inclusion of protein-induced dynamic and static disorder.

As in all photosynthetic antennae the coupling between electronic and vibrational degrees of freedom plays an important role in LHC-II. For the lowest state at about 680 nm early hole-burning studies suggested a Huang–Rhys factor (compare Eq. (105)) of $S = 0.4$ and a mean vibrational frequencies of $\omega_{\text{vib}} \sim 20\,\text{cm}^{-1}$ [210]. Recently, using higher resolution, values of $S = 0.8$ and $\omega_{\text{vib}} \sim 18\,\text{cm}^{-1}$ have been obtained which independently reproduced the Stokes shift $(= 2S\omega_{\text{vib}})$ of about $29\,\text{cm}^{-1}$ for the exciton lowest state at a temperature of 5 K [42]. In Ref. [42] it was also found that the Huang–Rhys factor is smaller than unity in between the interval from 640 to 682 nm. A value of $S = 0.6 \pm 0.1$ for the Huang–Rhys factor has been found in polarized site-selective fluorescence measurements at 4 K [41]. It was assigned to protein motions while as many as 48 distinct vibrational modes could be identified. On the other hand, analysis of the temperature-dependent fluorescence and absorption linewidth resulted in a mean vibrational frequency of $\omega_{\text{vib}} = 40\,\text{cm}^{-1}$ [215].

Recently, in [85] it could be demonstrated, how the above characteristics of exciton–vibrational coupling in the LHC-II can be used to describe linear absorption and circular dichroism spectra. Based on the fitting of linear absorption at different temperatures using the non-Markovian formulation of the absorption coefficient (Eq. (184)) two different structural models of Chl assignments were investigated. Within both models a satisfying fit could be obtained. However, the circular dichroism simulation clearly favored the model of Gradinaru et al. [207]. Experimental data and fits are shown together in Figs. 20 and 21. The respective level assignment is given in the upper part of Fig. 21. Static disorder was included by a Monte Carlo-type simulation using the mean site energies of the 12 Chls as fit parameters. To keep the number of fit parameters small the same strength of static disorder has been assumed for all pigments. The simulation gave a width of $140\,\text{cm}^{-1}$ (FWHM) for the Gaussian distribution of pigment transition energies. To relate this number to hole-burning experiments, motional narrowing [216] which leads to a smaller width of the distribution of exciton energies must be considered. From the comparison of the obtained widths for the exciton states with the width for the pigment transition energies the delocalization of the exciton in the different states could be estimated. The states in the Chl*a* region (except the lowest) showed a mean delocalization length of about four pigments whereas in the Chl*b* region this number is lower by a factor of two. Dynamic disorder has been neglected for this estimation. Therefore, the above delocalization numbers have to be understood as upper limits. The influence of dynamic disorder on the homogeneous line widths has been taken into account by assuming a single lineshape for the spectral density (estimated from the fluorescence side band at low temperatures [214]) and using the amplitude (integral over the spectral density, i.e. the Huang–Rhys factor) as a fit parameter. For Chl*a* a Huang–Rhys factor of 0.95 was obtained and for Chl*b* this value amounts 0.75. An equal Huang–Rhys factor for all Chl*a* and all Chl*b* was assumed. To relate these values to hole-burning experiments, excitonic PES were constructed and from these Huang–Rhys factors of the exciton states could be obtained.

We note that the above calculations used results from extensive exciton simulations of global features of polarized absorption [217] and energy transfer kinetics [218] which allowed to reduce the number of possible configurations of Chl transition dipole geometries. In the light of the recent experimental results on LHC-II mutants and the suggested new assignment of Chl [208] similiar

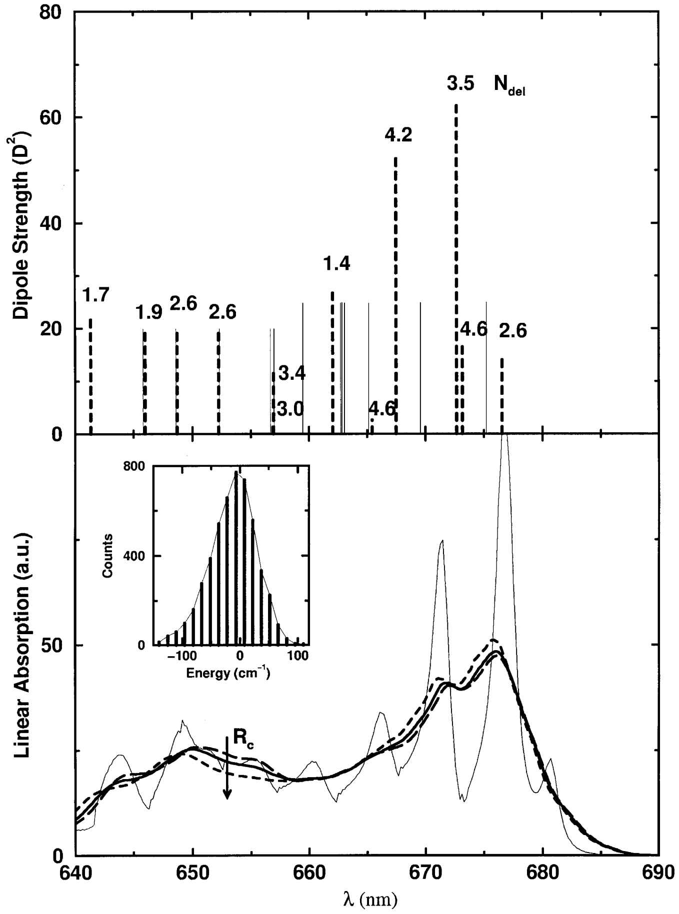

Fig. 21. Upper panel: Mean site energies of the Chl in the LHC-II monomer (thin solid lines, from left to right: Chl $b_6, b_2, b_3, b_5, b_1, a_7, a_1, a_3, a_5, a_6, a_2, a_4$). The dashed vertical lines give the exciton stick spectrum where the height of the lines corresponds to the respective dipole strength of the transition. (The mean delocalization number of the exciton states are drawn at the top of the lines, for more details see [85].) The optimization procedure gave for the pigment's dipole strength values of 20 D^2 (assumed equal for all Chl*b*) and 25 D^2 (assumed equal for all Chl*a*). Lower panel: Homogenous absorption (thin solid line) at 80 K for the mean site energies and inhomogeneous absorption for different values of the correlation radius of protein vibrations, $Z_{corr} = 20$ Å (solid line – same as in Fig. 20), $Z_{corr} = 2$ Å (long dashed line) and $Z_{corr} = 200$ Å (short dashed line). The inset shows the distribution of the lowest state exciton energy.

simulations could be very useful to reduce the number of possible dipole configurations. The model proposed in [85] could then be used to refine the local site energies of the pigments.

A crucial test for the suggested LHC-II pigment organizations would be the ability to reproduce nonlinear optical data on the energy transfer dynamics in the time domain. Early pump–probe investigations estimated the Chl*a*–Chl*b* transfer time to be about 6 ps [219]. However, with increasing time resolution this number decreased starting with the fluorescence up conversion experiments by Eads and co-workers [220] which resulted in a 500 fs time scale for this transfer step. Recent years witnessed a number of investigations of the LHC-II energy transfer dynamics revealing time scales for Chl*a*–Chl*b* transfer close to about 100 fs [135,209,221–226] (for an overview see also Ref. [225].) In particular, it became obvious that this structurally heterogeneous complex supports a multitude of transfer times ranging from some 100 fs to a few picoseconds for the Chl*a*–Chl*b* transfer up to some tenths of picoseconds for the intra-Chl*a* pool transfer [224,227]. Further, studying LHC-II monomers it was concluded that the ultrafast Chl*a*–Chl*b* transfer [226] as well as the slower spectral equilibration between the Chl*a* monomers [207] is of intramonomer nature.

9.2. The dimer model

The organization of the LHC-II complex in Chl*a*/*b* pairs which are responsible for the subpicosecond energy transfer dynamics lends itself to use a dimer model. Here the monomers correspond to Chl*a* and Chl*b* pigment molecules. Within this reduced description of the LHC-II it is possible to include explicitly the coupling to a few vibrational modes as outlined in Sections 4.4 and 5.2.1. In the present context, the incorporation of one *effective* vibrational mode per monomer is suggested by the fact that Chl*a* and Chl*b* are bound to different proteins [3]. The remaining vibrational degrees of freedom of the LHC-II are considered to form a heat bath for the two site, two mode model. The population dynamics within such a model dimer has been considered, for instance, in Refs. [100,202]. A Brownian oscillator description of the dimer spectroscopy was given in [228]. Further, it should be noted that the theory presented below is, of course, applicable to other photosynthetic dimer systems such as the C-phycocyanin trimers [229] and the B820 subunit of LH1.

The potential energy surfaces for the dimer model are shown in Fig. 22. Notice that each site has its own effective vibrational coordinate, i.e., as far as it concerns the vibrational states the problem is essentially two-dimensional. Further, we have included a higher excited intramonomer S_n state which becomes relevant when studying the effect of high pulse intensities (see below). From the structural data the relative orientations of the monomeric transition dipole moments $\boldsymbol{d}_{eg}^{(m)}$ could not be obtained. Pump–probe spectroscopy, however, provides a hint to the most probable mutual orientation as will be shown in the following section.

9.2.1. Evidence for the dipole transition geometry

In order to describe third-order nonlinear optical spectroscopy one- and two-exciton states have to be included in the description. The situation is sketched for the dimer model in Fig. 23 where we neglected the intramolecular S_n states. A pump pulse with wave vector $\boldsymbol{k}_{\mathrm{pu}}$ excites the sample. The evolution of this excitation is probed by a delayed weak probe pulse ($\tau_{\mathrm{d}} = \tau_0^{(\mathrm{pu})} - \tau_0^{(\mathrm{pr})}$). In order to figure out the relevant contribution of the nonlinear polarization the density matrix has to be propagated with both pulses as explained in Section 6.2. From the obtained amplitude $P_{n_{\mathrm{pu}}=0,n_{\mathrm{pr}}=0}$ of the polarization wave the time integrated detector signal $S_{\mathrm{tot}}(E_{\mathrm{pu}}, E_{\mathrm{pr}}, \tau_{\mathrm{d}})$ can be calculated which together with the linear absorption $S_{\mathrm{tot}}(E_{\mathrm{pu}} = 0, E_{\mathrm{pr}})$ determines the differential absorption according to Eq. (197). This quantity is measured in a pump–probe experiment in dependence on the delay time between the two pulses.

In Fig. 24 the pump–probe signal, Eq. (197), is shown for the pump pulse tuned in resonance with the Chl*b* transition and the probe pulse centered at Chl*a* transition. The signal is shown for three different orientations of the transition dipoles. The system–environment coupling was described by

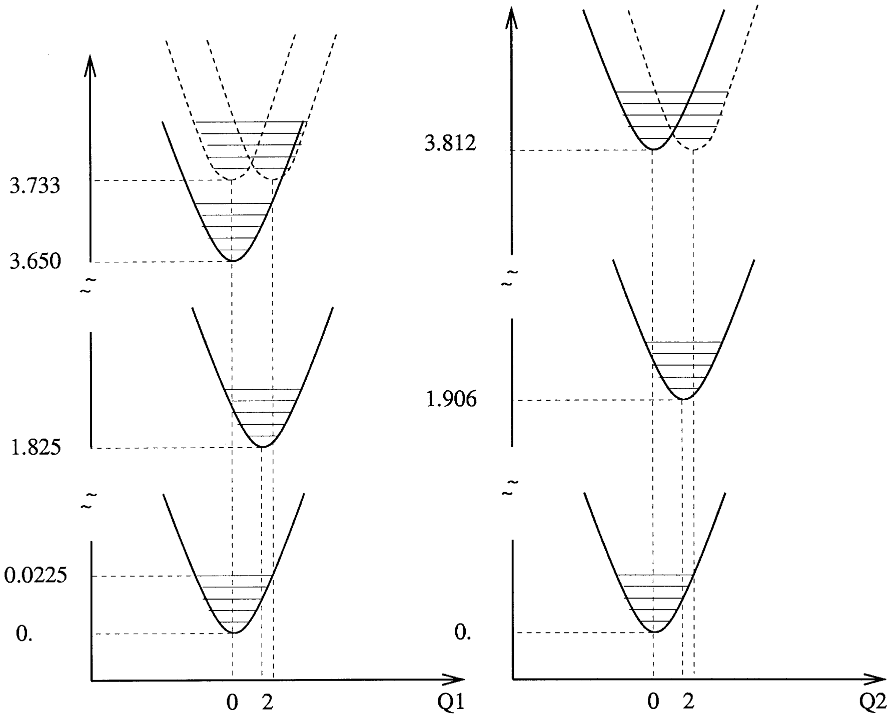

Fig. 22. Potential energy surfaces for the Chla/b dimer model of LHC-II. Each monomer is described by three electronic states and an individual vibrational coordinate. The displacement along the dimensionless normal mode coordinates corresponds to a Huang–Rhys factor of 0.6 (S_1 states) and 1.0 (S_n states); the effective vibrational frequency is $40\,\text{cm}^{-1}$ for both sites [215]. The dipole–dipole coupling strength is $J_{12} = 11\,\text{meV}$ ($89\,\text{cm}^{-1}$) for the sandwich [↑↑], 13 meV ($105\,\text{cm}^{-1}$) for the in-line [← ←], and 0 meV for the perpendicular [← ↑] dipole geometry (dielectric constant $\varepsilon = 2.0$, $|d_{eg}^{\text{Chl}a}|^2 = 20\,\text{D}^2$ and $|d_{eg}^{\text{Chl}b}|^2 = 15\,\text{D}^2$).

a flat spectral density including diagonal EVC and no correlations between the different sites. The coupling strength was taken as $g\hbar\omega = 0.8\,\text{meV}$.

The signal in Fig. 24 can be understood by considering the four possible electronic states only. The coupling to the vibrational states is reduced to the relaxation between the one-exciton eigenstates only for simplicity. Due to the large gap between Chl$a$ and Chl$b$ S_0–S_1 transitions, the difference between exciton eigenstates and monomer energies is rather small. However, as shown in Ref. [12] the wave functions and thus the transition dipole matrix elements are influenced by the Coulomb interaction. To quantify this effect we defined the ratio between two- and one-exciton transition dipoles at a certain wavelength $\lambda_\pm$ [12]

$$r_{2,\lambda_\pm} = \left|\frac{\mu_{\mp\to 2}}{g\to\pm}\right|^2 = \left(\frac{1 \mp \text{sgn}(J_{12})|D|}{1 \pm \text{sgn}(J_{12})|D|}\right)^2 . \tag{210}$$

If the monomers are uncoupled ($D = 0$) it results $r_{2,\lambda\pm} = 1$. This reflects the fact that without coupling an optical transition within one pigment is independent of the electronic state of the other pigment.

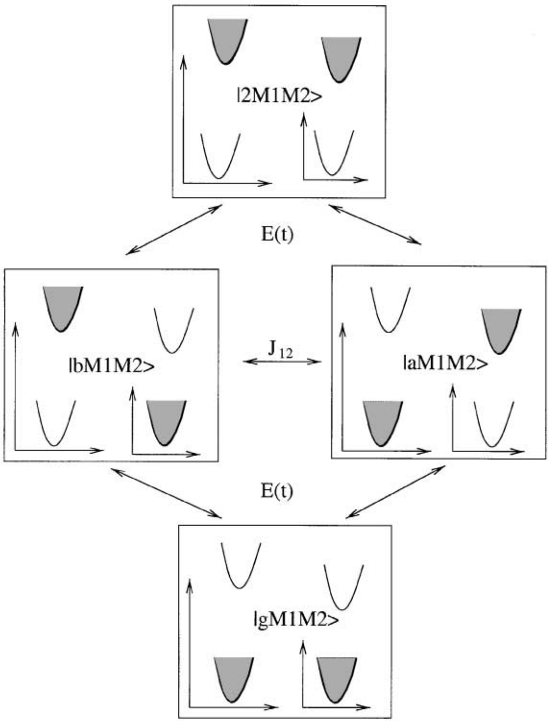

Fig. 23. Potential energy surfaces for the zero-, one- and two-exciton states of the dimer model (filled area indicates population of electron–vibrational state). Transitions between different exciton manifolds are due to the external field; the one-exciton states are coupled via the dipole–dipole interaction.

Using Eq. (210) the two-color spectra shown in Fig. 24 can be explained as follows. The pump pulse populates the upper one-exciton eigenstate $|+\rangle$ of the system according to the Franck–Condon overlap integrals. The probe pulse centered at the lower one-exciton transition energy E_- can either lead to a ground state absorption or to an excited state absorption. If the ratio $r_{2,\lambda_\pm} > 1$ at the probe pulse wavelength λ_- (*sandwich* geometry) the excited state absorption will over-compensate the ground state bleaching giving rise to a positive pump–probe signal. For $r_{2,\lambda_\pm} < 1$ (*in-line* geometry) the excited state absorption is weaker than the ground state bleaching and the signal will be negative. Since the signal observed in [135] is negative, we are in the position to conclude that the geometry of the dipoles of the Chl*a*/*b* dimers in the membrane is rather *in-line* [12,213]. An important point concerning the ultrafast component of the signal is that it is caused by the delocalization of the exciton wave function and *not* by a hopping like transfer of excitation energy. This is in agreement with the observation that the determination of the time scale of the ultrafast component was limited by the resolution of the experimental setup used in [135].

Next, the picosecond component of the calculated transfer dynamics in Fig. 24 will be discussed. The relaxation of the pump-pulse-induced population from the high-energetic to the low-energetic exciton state reduces the excited state absorption, because the probe pulse is off-resonant to the transition between the low-energetic one- and the two-exciton states. On the other hand, the probe

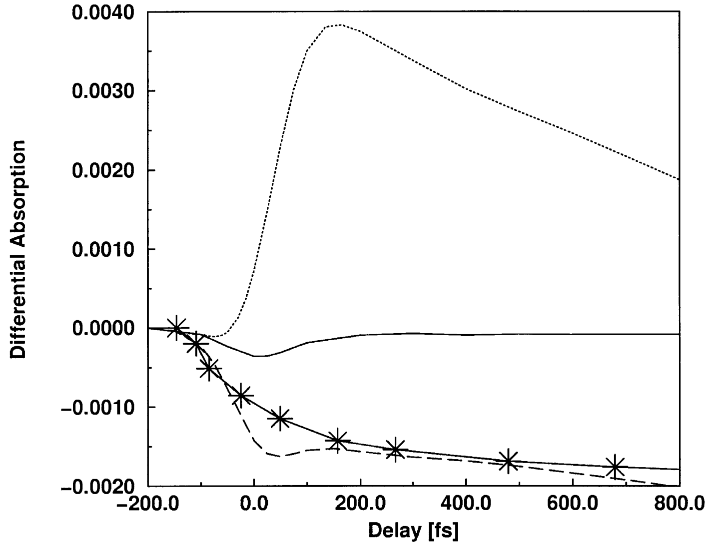

Fig. 24. Two-color pump–probe spectra for the pump wavelength of 650 nm (Chl*b*) and a probe wavelength of 680 nm (Chl*a*). Pulse parameter: $\tau_p = \tau_t = 100\,\mathrm{fs}$ (FWHM 120 fs). The spectrum was calculated for different orientations of the monomer dipoles, sandwich like (dotted line), in line (dashed line) and perpendicular orientation (full line). The experimental spectrum of Bittner et al. is shown with stars [135].

pulse can stimulate transitions of low-energetic excitons back to the ground state. Both effects increase the probe transmission resulting in a decay of the pump–probe signal with the relaxation time of the excitons.

9.2.2. Intensity dependence of two-color pump–probe signals

To understand the intensity dependence of the pump–probe signals requires the inclusion of the higher excited S_n-states. Thus, one has to consider the nine electronic state scheme shown in Fig. 25. The assignment of a single S_1–S_n transition energy for the different monomers is complicated by the fact that the spectra for excited state absorption of chlorophylls are rather broad. In order to explore the principal effect we will assume that $\varepsilon_{mf} - \varepsilon_{me} = \varepsilon_{me} - \varepsilon_{mg}$ for simplicity (cf. Appendix A). The ratio between the different intramolecular transition dipole moments, $d_{fe}^{(m)}/d_{eg}^{(m)}$, will be taken as a parameter.

In Fig. 26, we compare the calculated and the measured [135] two-color pump–probe signals for different intensities of the pump pulse. The agreement for the asymptotic signals is rather good and could be used to fix the relaxation and internal conversion parameters (see figure caption) as well as the ratio $d_{fe}^{(m)}/d_{eg}^{(m)}$ which was found to be 1.19 [14].

At long delay times the signal for high pump intensities is decaying while for lower intensities it is still rising. In order to trace the origin of this behavior we consider the occupation probabilities of the exciton eigenstates $|\alpha_N\rangle$ defined as

$$P_{\alpha_N}(Q_1, Q_2) = \sum_{ab} \left(C^*_{a\alpha_N}(Q_1, Q_2)\rho_{ab}(Q_1, Q_2)C_{b,\alpha_N}(Q_1, Q_2)\right) , \tag{211}$$

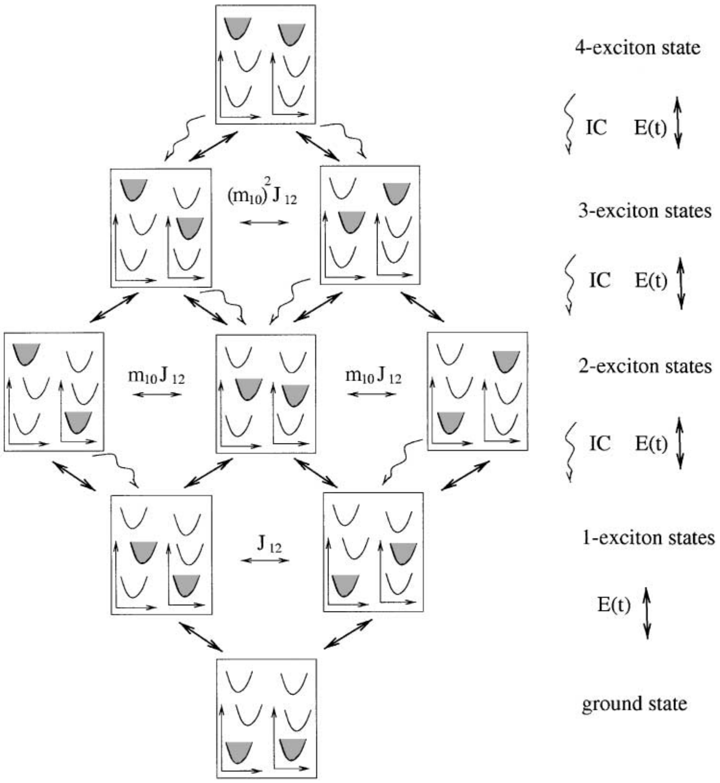

Fig. 25. Potential energy surfaces for the possible exciton states of the dimer model with intramolecular excited state absorption (filled area indicates population of electron–vibrational state). Transitions between different exciton manifolds are due to the external field or internal conversion (internal conversion between the one-exciton manifold and the ground state can be neglected); one- and two-exciton states are coupled via the dipole–dipole interaction (note the scaling of the dipole–dipole coupling with $m_{10} = |\mathbf{d}_{fe}|/|\mathbf{d}_{eg}|$ if the state φ_f is involved, cf. Section 3.5).

where α_N counts the eigenstate in the N-exciton manifold ($N = 0 \ldots 4$). $a = \{a_1, a_2\}$ and $b = \{b_1, b_2\}$ are the electronic quantum numbers of the dimer. The coefficients $C_{a\alpha_N}$ are obtained by diagonalizing the electronic part of the Hamiltonian including the dipole–dipole interaction for fixed values of the (classical) effective vibrational coordinates Q_1 and Q_2. As explained in [14,101] the Q_1/Q_2 dependence of Eq. (211) is rather weak and can be neglected.

In Fig. 27 the state occupation probabilities in the one- and two-exciton manifolds are shown for the two extreme intensities I_0 (full line) and $3.1 I_0$ (dashed line); the relevant relaxation channels and the excitation conditions are schematically plotted in Fig. 28.

The pump pulse populates mainly the upper one-exciton state $|1+\rangle$ and the highest two-exciton state $|2+\rangle$. Due to the interplay of the dipole–dipole coupling and the vibrational energy dissipation a relaxation between exciton states in the same manifold takes place (for example, the transition from $|1+\rangle$ to $|1-\rangle$). However, there is also IC-type relaxation between different exciton manifolds which becomes important at higher intensities where higher manifolds are populated. At low intensities the population of the one-exciton manifold determines the nonlinear optical

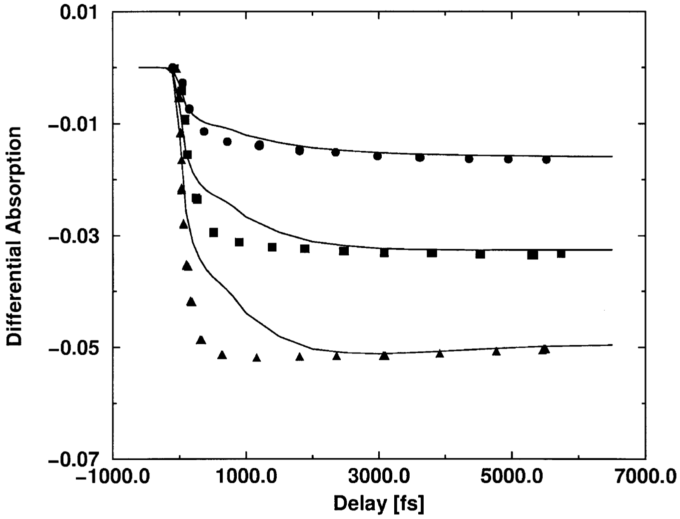

Fig. 26. Two-color pump–probe signals measured by Bittner et al. [135] versus delay time for three different peak intensities of the pump beam: $I_0 = 6\times10^{13}$ photons cm^{-2} pulse^{-1} (circles), $2.2I_0$ (squares), and $3.1I_0$ (triangles). The simulation was performed at 4.2 K including four vibrational states per potential energy surface. Pump and probe pulse were of Gaussian shape assuming a width of 100 fs. Off-diagonal fluctuations of the dipole–dipole coupling has been included what necessitated to change the coupling strength $g\hbar\omega$ to 0.5 meV as compared with Fig. 24. For the internal conversion rates we used $\hbar R^{(\mathrm{IC})}_{S_n\to S_1} = 0.3$ meV ($1/R^{(\mathrm{IC})}_{S_n\to S_1} = 2.2$ ps).

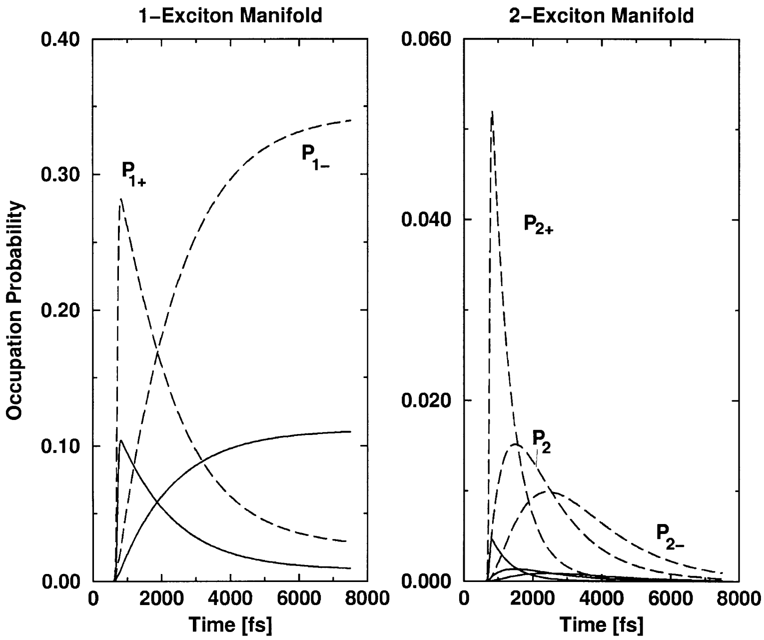

Fig. 27. Multi-exciton state population for the two extreme pump intensities $I_0 = 6\times10^{13}$ photons cm^{-2} pulse^{-1} (full line) and 3.1 I_0 (dashed line) versus time.

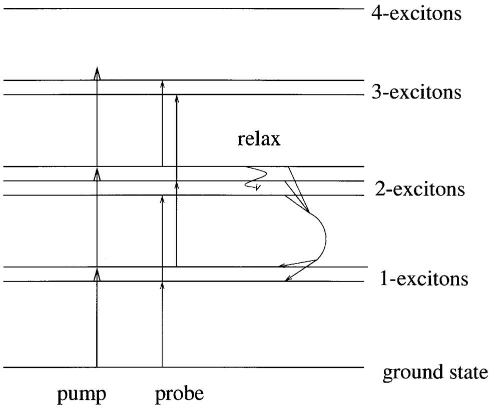

Fig. 28. Electronic eigenstates of the dimer. Arrows indicate the action of the external fields in the two-color pump–probe setup. Wavy lines show the relevant relaxation processes within and between the exciton manifolds.

response. Due to the relaxation $|1+\rangle \rightarrow |1-\rangle$ there is an increase of the probe-pulse transmission as a consequence of stimulated emission from the lower one-exciton state to the ground state. But, at higher intensities this effect is over-compensated by an increase of the probe-pulse absorption. This originates from the relaxation between the two- and the one-exciton manifold, which opens new channels for the probe pulse to be absorbed. Additionally, Fig. 27 displays that the ratio between the occupations of the two- and the one-exciton manifold becomes larger with increasing intensity. This causes the qualitative change of the differential absorption in the related pump–probe experiment.

9.2.3. Intramolecular excited state absorption

In the following it will be shown that one-color pump–probe spectroscopy can be used to draw conclusions on the nature of the intramolecular S_1–S_n transitions [101]. To this end we modeled the low-temperature data obtained by Visser et al. [224]. In order to provide optimum monomeric excited state absorption at both pigments, the S_1–S_n transition energies have been set equal to the Chl*a* value for which the probe pulse is resonant.

One prominent feature of the experimental data shown in Fig. 29 is the change of the sign around 2 ps delay. This indicates that upon one-exciton relaxation excited state absorption from the lower one-exciton state into the two-exciton manifold dominates [135,224]. As shown in Ref. [151] the dipole–dipole coupling between intramolecular double excitation states and delocalized two-exciton states leads to a redistribution of oscillator strength strength within the two-exciton manifold as well as to some energetic shift of the different states. The strength of this interaction is proportional to the ratio $d_{fe}^{(m)}/d_{eg}^{(m)}$. Thus changing $d_{fe}^{(m)}/d_{eg}^{(m)}$ for a given transition energy will modify the absorption out of the lower one-exciton state. This effect is clearly seen in Fig. 29 where we plotted the signal calculated for different $d_{fe}^{(m)}/d_{eg}^{(m)}$. The fact that the excited state absorption becomes weaker with increasing $d_{fe}^{(m)}/d_{eg}^{(m)}$ indicates that the relevant two-exciton eigenstate moves out of resonance with the probe pulse.

In order to determine the influence of the mutual displacements of the excited PES of the pigments in Fig. 30 the previous simulation is compared with the case for which the minimum of

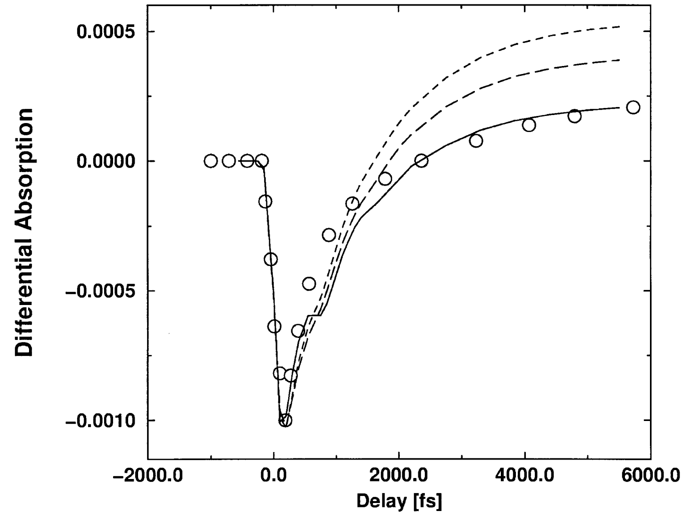

Fig. 29. Influence of intramolecular excited state absorption in the simulation of the 77 K one-color pump–probe experiment of [224] (Circles). Pumping and probing at wavelength 650 nm (Chl*b*), pulse widths 150 fs (FWHM 175 s) for an energy of the Chl*a* S_n-state at $\varepsilon_{1f} = 3.733\,\mathrm{eV}$, (i.e. strong intramolecular excited state absorption at the probe wavelength). Same coupling to the environment as in the simulation of two-color pump–probe signals (see Fig. 26). Simulation for different strengths of intramolecular excited state absorption, characterized by the ratio of transition dipole moments $m_{10} = |\boldsymbol{d}_{fe}|/|\boldsymbol{d}_{eg}|$ (cf. Section 3.5): $m_{10} = 0$, i.e. no intramolecular excited state absorption (long dashed line), $m_{10} = 0.5$ (dashed line), $m_{10} = 1.19$ (solid line).

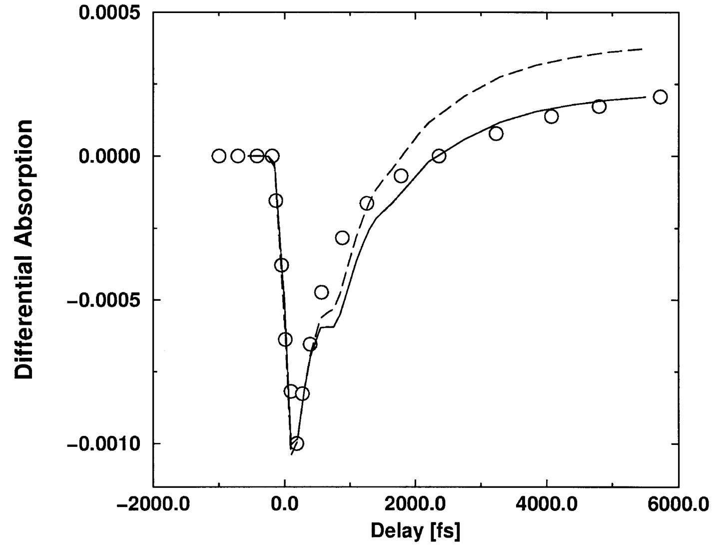

Fig. 30. Simulation of the 77 K one-color pump–probe experiment of Visser et al. [224] (Circles). Influence of the displacement of the S_n PES of the pigments. Solid line same as in Fig. 29: $Q^{(0)}_{j,S_n} - Q^{(0)}_{j,S_1} = -1.41$, dashed line $Q^{(0)}_{j,S_n} - Q^{(0)}_{j,S_1} = +1.41$. All the remaining parameters as for the solid line in Fig. 29.

the S_n PES of the pigments is shifted by the same value as the S_1 state PES but into the opposite direction. Since this shifts also the vertical Franck–Condon energy for excited state absorption, the long-time dynamics will be modified. In line with the above given arguments and Fig. 29 it is clear that in principle the original result could be recovered by increasing the ratio between the transition dipole moments, $d^{(m)}_{fe}/d^{(m)}_{eg}$. However, since large ratios $d^{(m)}_{fe}/d^{(m)}_{eg}$ are rather unlikely we conclude that an appreciable shift of the S_n state PES minimum position can be excluded.

Finally, we comment on the plateau which is discernible in Fig. 29 after about 800 fs. This time corresponds to the vibrational period of the motion in the different PES. Obviously, the wave packet motion in the Chl*b* S_1-state which is initiated by the electronic transition is monitored by the probe pulse. Note that because of the dissipative nature of the Chl*b*/*a* transfer no vibrational coherences were seen in the simulation of the two-color experiments (cf. Fig. 26). However, such a signature of coherent vibrational motion has not yet been observed in experiments on the LHC-II, even though it is documented for the bacterial light-harvesting complexes LH1 and LH2 [99]. One reason for the lack of indications for coherent vibrational motion in LHC-II may be the large heterogeneity of this complex, which causes a destructive interference of many vibrational frequencies.

9.2.4. Signatures of non-Markovian dynamics

So far it has been tacitly assumed that the nonperurbative inclusion of effective vibrational modes is essential for the simulation of the pump–probe signals. In view of the rather small Huang–Rhys factors [42,210], implying a weak EVC, one might wonder whether a simple exciton description where *all* vibrational degrees of freedom are comprised in the reservoir would not give the same result. In order to test this assertion we compare in Fig. 31 one-color pump–probe spectra with and without incorporation of an effective vibrational mode. In the simple excitonic model (thin dashed lines) and using the same flat spectral density it was only possible either to simulate the femtosecond part of the signal, or to get a good agreement for the long time behavior. As stated before the model which includes the effective vibrational mode gave a good fit to the global time evolution. This finding has been explained to originate from the retardation effects seen in the pump–probe signal due to the vibrational wave packet motion along the effective vibrational coordinate [14].

Alternatively, one can characterize this as the signature of non-*Markovian* memory effects present in the measured data. The presence of these memory effects has also been demonstrated for the intensity-dependent two-color pump–probe signals [14,101].

9.3. Two-exciton spectroscopy

In the previous section it was found that the presence of higher excited intramolecular S_n states may have an influence on the pump–probe spectra as a consequence of the mixing between these intramolecular double excitations with delocalized two-exciton states. As shown in Ref. [151] the strength of this coupling depends on the ratio between the intramolecular transition dipole moments as wells as on the intramolecular electronic anharmonicity. As a matter of fact the pump–probe signals with resonant excitation give only an indirect indication for the spectrum and oscillator strength distribution within the two-exciton manifold. In Ref. [138] it was shown that the

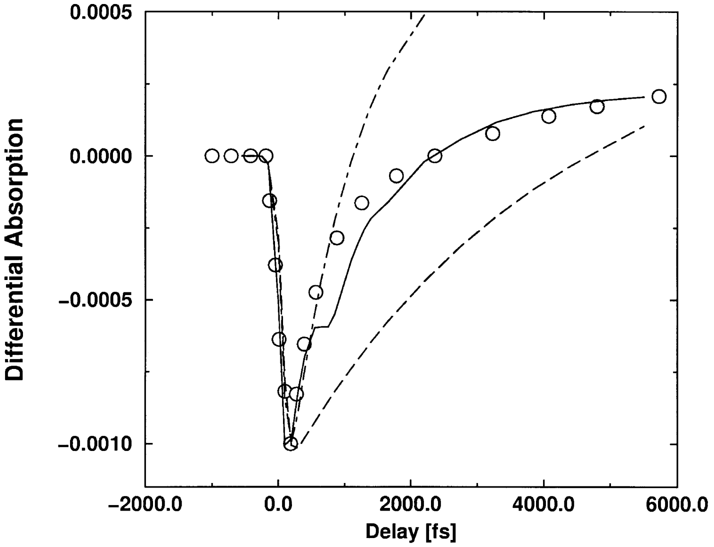

Fig. 31. Simulation of the 77 K one-color pump–probe experiment of Visser et al. [224] (circles) in different models, solid line: one effective vibrational mode per monomer, dashed lines: all vibrational degrees of freedom are treated as a heat bath modulating the dipole–dipole interaction. Higher excited state of Chl*a* at $\varepsilon_{1f} = 3.733\,\mathrm{eV}$, fluctuation of the monomer site energies as in Fig. 29, fluctuations of the dipole–dipole interaction correspond to an inverse rate constants of 0.6 ps (dashed dotted line), 2.3 ps (dashed line) and 2.7 ps (solid line).

so-called two-exciton photon echo spectroscopy [230] gives a more direct access to the two-exciton manifold. Here at time zero a first pulse tuned in resonance with the one-exciton band creates a coherence oscillating with the transition frequency $\Omega(\alpha_1,0)$. After a delay time τ pulses 2 and 3 act simultaneously both being off-resonance with the one-exciton band, but $\omega_2 + \omega_3$ lies within the two-exciton band. This transforms the system into a coherence between the one- and two-exciton bands oscillating with the frequency $\Omega(\alpha_1,\alpha_2)$. Provided the energy level structure is such that $\Omega(\alpha_1,0) \approx \Omega(\alpha_2,\alpha_1)$, i.e. the system is almost harmonic and that there is dephasing due to static energetic disorder, an echo signal can be expected at $t = 2\tau$ in direction $\boldsymbol{k}_s = \boldsymbol{k}_3 + \boldsymbol{k}_2 - \boldsymbol{k}_1$ [230]. In Ref. [231], it was found that the heterogeneous exciton-level structure of the LHC-II is amenable for observation of the two-exciton photon echo. The details of the signal are very sensitive with respect to the structure of the two-exciton band.

10. Conclusions

Being a field which crosses the borders of biology, chemistry, and physics the research on photosynthetic antenna systems and their pigment (chlorophyll) protein complexes attracted considerable attention over the years. The main task of these systems is to absorb light in the visible region, and consequently optical spectroscopy represents an adequate experimental technique to study the properties of antenna systems. The correct interpretation of the measured spectra asks, on the one hand side, for the formulation of microscopic models based on the detailed structures.

Furthermore, because of the complexity of these models it is necessary to utilize concepts of dissipative quantum dynamics. By means of these approaches one is able to simulate various properties of the antenna systems which have been determined in optical measurements carried out either in the frequency domain or in the ultrashort (femtosecond) time domain.

It has been underlined that the concept of the Frenkel exciton model (including some necessary extensions of its standard version) in combination with a coupling to the vibrational modes of the pigment protein complexes establishes an appropriate model system. Moreover, the reduced multi-exciton density matrix determined by the Quantum Master Equation has to be considered as the unique framework for the description of excitation energy dynamics. This theoretical concept together with its ability to simulate the dissipative exciton motion has to be considered as an important link which connects the known structures and the various experimental data and enables us to achieve a deeper understanding of the structure function relationship. The possible extension to the case of a strong exciton–vibrational coupling has been presented for a dimer model showing the importance of memory effects for the simulation of nonlinear optical spectra.

Primarily, the task of all physico–chemical research on photosynthetic antenna systems is to help biologists to unravel the mechanism of life. But there is a tendency to investigate pigment–protein complexes as a system of basic physical research. Since the pigment–protein complexes with a known structure represent one of the best characterized types of dye aggregates these biological macromolecules are also used to test new experimental techniques as well as microscopic theories. One point which attracts the interest of basic research is the large number of electronic levels which often are only masked by a weak or intermediate inhomogeneous broadening. And, using site-directed mutagenesis a given structure of a pigment–protein complex can be altered in a controllable manner.

Comparing pigment–protein complexes with systems traditionally investigated in molecular or chemical physics they really seem to be too complex for a theoretical description. But it has to be grasped as one main message here that this prejudice is not correct for the interpretation of the large number of optical experiments. This is due to the fact that the experiments mostly provide access to the electronic degrees of freedom of the pigments only. The protein enters the description in an approximate manner via different types of spectral densities (besides its static function to fix the spatial position of the pigments as well as their so-called site energies). Nevertheless, optical spectroscopy enables us to draw different conclusions on the functionality of pigment–protein complexes with emphasis on their ability to absorb light and to transfer excitation energy. The investigations reviewed in the foregoing sections underline the importance of the pigment geometry and of static disorder for the frequency range and strength of light absorption. Furthermore, it has been possible to achieve a detailed understanding of exciton relaxation which is of basic importance for the transfer of excitation energy from the antennae to the reaction center. Interestingly, the main complication of the theoretical approach related to the existence of higher exciton manifolds seems to be of no importance for the functionality under physiological conditions. On the contrary, higher exciton manifolds are essential for the understanding of nonlinear optical processes.

Meanwhile, the research arrived at a point where the chlorophyll absorption and exciton motion has been understood to a certain extent. Consequently, the different carotenoid species absorbing at shorter wavelength received a lot of interest. But photosynthetic antenna systems have also inspired people to develop (by chemical synthesis or mechanisms of self-organization) artificial antenna systems. An earlier approach has been based on the use of the Langmuir–Blodgett technique. Of current interest are macromolecules which show a structural self-similarity and which are known as dendrimers (see, for example, [232]).

Another point of possible intensive future research we would like to mention is the application of single molecule spectroscopic techniques to photosynthetic antenna systems. There are some first results (see, e.g., [233]) which show that the investigation of a single complex offers direct insight into the respective individual environment. Since the latter is formed by the carrier protein one would get access to the different types of protein conformations.

Have theoretical physics and theoretical chemistry reached a point where the main concepts and simulation techniques to describe dissipative exciton motion in photosynthetic antennae have been worked out? To a certain extent we would like to answer in an affirmative way. As it has been explained in the preceding sections there is a large number of experiments which can be understood in the existing framework of microscopic models and density matrix approaches. But in relation to this work there is still one open question. For all mentioned types of theories it would be of great importance to consequently calculate the microscopic parameters entering the computations. This includes, for example, the correct position of the electronic levels in the protein environment, the Coulomb interaction and the coupling to the protein vibrations. In doing so, the number of free parameters entering the theoretical description can be reduced. Additionally, it would be of interest to get the various protein spectral densities as the result of, for example, molecular dynamic simulations.

Concerning, however, stronger exciton–vibrational coupling there is a current need to improve the existing simulation techniques either on larger systems (what is necessary for the path integral approach) or to a description which fully accounts for the quantum nature of the vibrational motion (this has to be done, for example, if one uses the so-called surface hopping method). Probably, the Liouville space approach is a useful way to meet this goal. Since pigment–protein complexes represent an valuable system to test new attempts in the field of dissipative quantum dynamics there would be a fertilization by this biological-oriented research of some basic problems of theoretical chemical physics.

Acknowledgements

Financial support by the Studienstiftung des Deutschen Volkes (T. R.), the Alexander von Humboldt foundation (T. R.) and the Deutsche Forschungsgemeinschaft (V. M., project Ma1356/7-1, O. K., project Ku752/2-1) are gratefully acknowledged.

Appendix A. The chlorophyll three-level model

The three-level model has been introduced at the end of Section 3.2. It is characterized by three electronic states for each Chl molecule with energy ε_{mg}, ε_{me}, and ε_{mf}, corresponding to the ground, the first excited, and a higher excited singlet level, respectively. The higher excited level has to be chosen to fulfill the relation $\varepsilon_{mf} - \varepsilon_{mg} \approx \varepsilon_{me} - \varepsilon_{mg}$. The main reason for such a more involved model is to include an intramolecular channel for excited state absorption, namely the transition from the first excited to the higher excited state. Hence, we provide the existence of a transition dipole moment $\boldsymbol{d}_{fe}^{(m)} = \langle \varphi_{mf} | \hat{\mu}_m | \varphi_{me} \rangle$. Correspondingly, the complete single-Chl dipole operator reads

$$\hat{\mu}_m = \boldsymbol{d}_{eg}^{(m)} | \varphi_{me} \rangle \langle \varphi_{mg} | + \boldsymbol{d}_{fe}^{(m)} | \varphi_{mf} \rangle \langle \varphi_{me} | + \text{h.c.} \tag{A.1}$$

The electronic PPC Hamiltonian H_{el}, Eq. (15) follows as

$$\begin{aligned} H_{\text{el}} = & \sum_m (\varepsilon_{mg} | \varphi_{mg} \rangle \langle \varphi_{mg} | + \varepsilon_{me} | \varphi_{me} \rangle \langle \varphi_{me} | + \varepsilon_{mf} | \varphi_{mf} \rangle \langle \varphi_{mf} |) \\ & + \sum_{mn} (J_{mn}(e,g,e,g) | \varphi_{me} \rangle \langle \varphi_{mg} | \otimes | \varphi_{ng} \rangle \langle \varphi_{ne} | \\ & + J_{mn}(f,g,e,e) \{ | \varphi_{mf} \rangle \langle \varphi_{me} | \otimes | \varphi_{ng} \rangle \langle \varphi_{ne} | + \text{h.c.} \} \\ & + J_{mn}(f,e,f,e) | \varphi_{mf} \rangle \langle \varphi_{me} | \otimes | \varphi_{ne} \rangle \langle \varphi_{nf} |) \, . \end{aligned} \tag{A.2}$$

The first term of the interaction contribution describes transitions between the ground and the first excited state and has been already discussed within the two-level model, Section 3.3. The transition between the first excited and the higher excited S_n-level is encountered in the last term. The transition from a state with two S_1-excitations into a state with a single S_n-excitation is given by the second term whereas the reverse process is described by the hermitian conjugate contribution. To have a more compact notation we introduce excitation and de-excitation operators as in Section 3.3. Besides the operators Eqs. (19) and (20) one has to introduce operators allowing for a transition into the higher excited S_n-state. We use

$$D_m^+ = | \varphi_{mf} \rangle \langle \varphi_{me} | \tag{A.3}$$

and

$$D_m = | \varphi_{me} \rangle \langle \varphi_{mf} | \, . \tag{A.4}$$

Here, excitation and de-excitation from the state e to the state f are directly incorporated. Using the newly introduced operators Eqs. (A.3) and (A.4) the electronic Hamiltonian reads

$$\begin{aligned} H_{\text{el}} = & \sum_m (\varepsilon_{mg} B_m B_m^+ + \varepsilon_{me} B_m^+ B_m + \varepsilon_{mf} D_m^+ D_m) \\ & + \sum_{m,n} (J_{mn}(e,g,e,g) B_m^+ B_n + J_{mn}(f,e,f,e) D_m^+ D_n + \{ J_{mn}(f,g,e,e) D_m^+ B_n + \text{h.c.} \}) \, . \end{aligned} \tag{A.5}$$

The inclusion of a higher intramolecular excitations (into the S_n-state) has been done such that a degeneracy of this state exists with a state where two S_1-excitations are present at two different Chl. It is obvious that the state $|0\rangle$ and $|m\rangle$, introduced in Eqs. (27) and (28), respectively, does not change. But the two-excitation state $|m,n\rangle$ Eq. (29) has to be supplemented by a state with a single intramolecular excitation present in the state $|\varphi_f\rangle$:

$$|mf\rangle = | \varphi_{mf} \rangle \prod_{m \neq n} | \varphi_{ng} \rangle \, . \tag{A.6}$$

In a similar manner, the three-excitation state $|m_1, m_2, m_3\rangle$ must be completed by a state with a single excitation in state $|\varphi_e\rangle$ and a single excitation in state $|\varphi_f\rangle$. Generally, we expect a particular (quasi-) degeneracy of different types of excited states. On the one-hand, we have the PPC-states with M Chl molecules in the first excited state and N Chls in the higher excited state.

These state are degenerate with those states with $M + 2j$ Chl in state $|\varphi_e\rangle$ and with $N - j$ Chl in state $|\varphi_f\rangle$. The number $2j$ runs between $-M$ and $2N$. All possible excited states are comprised in the expression

$$|\{me\}_M;\{nf\}_N\rangle = \prod_{k=m_1}^{m_M} B_k^+ \prod_{l=n_1}^{n_N} D_l^+ B_l^+ \; |0\rangle \; , \tag{A.7}$$

where all excitations are present at different molecules and where $M + N \le N_{\text{Chl}}$ must be fulfilled. Clearly, if it is necessary to discuss highly excited states further excited intra-Chl states have to be incorporated.

The multi-excitation expansion of H_{el}, Eq. (A.2) or (A.5) becomes more involved as in the case of a two-level model for the single pigments. Since the interaction part of Hamiltonian, Eq. (A.5), mixes states with different numbers of Chl in the states $|\varphi_e\rangle$ and $|\varphi_f\rangle$ we introduce a new ordering of the unit operator $\mathbf{1}_{\text{PPC}}$ with respect to the number $\mathcal{N} = 2M + N$. This number is defined as the number of excitations with energy $\varepsilon_{me} - \varepsilon_{mg}$. We can write

$$\mathbf{1}_{\text{PPC}} = \sum_{\mathcal{N}=0}^{2N_{\text{Chl}}} \hat{P}_{\mathcal{N}} \; . \tag{A.8}$$

The projector on the $\mathcal{N}$-excitation state reads

$$\hat{P}_{\mathcal{N}} = \sum_{M=0}^{\mathcal{N}} \; \sum_{N=0}^{\mathcal{N}/2,(\mathcal{N}-1)/2} \delta_{\mathcal{N},M+2N} \sum_{\{me\}_M} \sum_{\{nf\}_N} |\{me\}_M;\{nf\}_N\rangle\langle\{me\}_M;\{nf\}_N| \; . \tag{A.9}$$

The appearance of $\mathcal{N}/2$ and $(\mathcal{N} - 1)/2$ in the summation with respect to N means that one has to take $\mathcal{N}/2$ as the upper limit if $\mathcal{N}$ is even and otherwise $(\mathcal{N} - 1)/2$.

The $\mathcal{N}$-excitation expansion of Hamiltonian, Eq. (A.5), can be written similar to Eqs. (33) and (35). We obtain

$$H_{\text{el}} = \sum_{\mathcal{N}=0}^{2N_{\text{Chl}}} (E_0 + \Delta\mathscr{H}_{\text{el}}^{(\mathcal{N})})\hat{P}_{\mathcal{N}} \; . \tag{A.10}$$

The electronic ground state energy of the PPC has been already introduced in Eq. (24). The remaining Hamiltonian reads ($\varepsilon_m(fg) = \varepsilon_{mf} - \varepsilon_{mg}$)

$$\begin{aligned} \mathscr{H}_{\text{el}}^{(\mathcal{N})} = \sum_{M=0}^{\mathcal{N}} \; \sum_{N=0}^{\mathcal{N}/2,(\mathcal{N}-1)/2} & \delta_{\mathcal{N},M+2N} \sum_{\{me\}_M} \sum_{\{nf\}_N} \\ & \times \Bigg(\sum_{k\in\{me\}_M} \varepsilon_k(eg) + \sum_{k\in\{nf\}_N} \varepsilon_k(fg) + \sum_{k\notin(\{me\}_M,\{nf\}_N)} \; \sum_{l\in\{me\}_M} J_{kl}(e,g,e,g) B_k^+ B_l \\ & + \sum_{k\in\{me\}_M} \; \sum_{l\in\{me\}_M} J_{kl}(f,g,e,e) D_k^+ B_l \end{aligned}$$

$$+ \sum_{k\notin(\{me\}_M,\{nf\}_N)} \sum_{l\in\{nf\}_N} J_{kl}(e,e,f,g)B_k^+ D_l$$

$$\left. + \sum_{k\in\{me\}_M} \sum_{l\in\{nf\}_N} J_{kl}(f,e,f,e)D_k^+ D_l \right) |\{me\}_M;\{nf\}_N\rangle\langle\{me\}_M;\{nf\}_N| \,. \tag{A.11}$$

Considering the second excited state the Hamiltonian is specified to

$$\mathcal{H}_{\mathrm{el}}^{(2)} = \sum_{k\neq l} (\varepsilon_k(eg) + \varepsilon_l(eg))\,|ke,le\rangle\langle ke,le| + \sum_k \varepsilon_k(fg)|kf\rangle\langle kf|$$

$$+ \sum_{k\neq l} \sum_{m\neq k,l} (J_{mk}(e,g,e,g)|me,le\rangle\langle ke,le| + J_{ml}(e,g,e,g)|ke,me\rangle\langle ke,le|)$$

$$+ 2\sum_{k\neq l} (J_{kl}(f,g,e,e)|kf\rangle\langle ke,le| + \mathrm{h.c.}) \,. \tag{A.12}$$

In the considered case of the three-level model for the single Chl the multi-exciton state is obtained as

$$|\mathcal{N}\alpha\rangle = \sum_{M=0}^{\mathcal{N}} \sum_{N=0}^{\mathcal{N}/2,(\mathcal{N}-1)/2} \delta_{\mathcal{N},M+2N} \sum_{\{me\}_M} \sum_{\{nf\}_N} C_\alpha(\{me\}_M;\{nf\}_N)\,|\{me\}_M;\{nf\}_N\rangle \,. \tag{A.13}$$

The expansion includes the proper combination of states with single-excited and doubly excited Chl. We give the two-exciton equation which splits up into separate equations

$$(E_{\alpha_2} - \varepsilon_m(eg) - \varepsilon_n(eg))C_\alpha(me,ne) = J_{mn}(f,g,e,e)C_\alpha(mf)$$

$$+ \sum_{k\neq m,n} (J_{mk}(e,g,e,g)C_\alpha(ke,ne) + J_{kn}(e,g,e,g)C_\alpha(me,ke)) \tag{A.14}$$

and

$$(E_{\alpha_2} - \varepsilon_m(fg))C_\alpha(mf) = 2\sum_n J_{mn}(f,g,e,e)C_\alpha(me,ne) \,. \tag{A.15}$$

The transition dipole operator into this two-exciton state reads

$$\hat{\mu}_{2,1} = \sum_{m,n} \boldsymbol{d}_{eg}^{(m)}|me,ne\rangle\langle ne| + \sum_m \boldsymbol{d}_{fe}^{(m)}|mf\rangle\langle me| \,. \tag{A.16}$$

To derive the EVC for the electronic three-level Chl-model we use the projection operator $\hat{P}_{\mathcal{N}}$ projecting on the $\mathcal{N}$-excited state and obtain the complete PPC-Hamiltonian as

$$H_{\mathrm{PPC}} = \sum_{\mathcal{N}} H_{\mathrm{PPC}}^{(\mathcal{N})}\hat{P}_{\mathcal{N}} \,. \tag{A.17}$$

$\mathcal{N}$ counts the number of excitations with energy $\varepsilon_m(eg)$, and again we get an equation of the type given in Eq. (60) but with $\mathcal{N}$ instead of N. The related excitation Hamiltonian $\mathcal{H}_{\mathrm{el}}^{(N)}$ is given in Eq. (A.11). Presenting $H_{\mathrm{PPC}}^{(\mathcal{N})}$ as the three-level extension of $H_{\mathrm{PPC}}^{(N)}$, Eq. (63) we avoid here to repeat the complete interaction terms (compare (A.11)). We only give the related PES which read

$$U(\{me\}_M\{nf\}_N;R) = U_0(R) + \sum_{k\in\{me\}_M} \varepsilon_k(eg;R) + \sum_{k\in\{nf\}_N} \varepsilon_k(fg;R)\ . \tag{A.18}$$

This expression may serve as the starting point for various approximations resulting in the respective multi-exciton–vibrational coupling as discussed for the two-level Chl model in Section 3.6 and in Appendix B.

Appendix B. Normal mode analysis of PPC vibrations

The following considerations are devoted to obtain the multi-exciton vibrational Hamiltonian, Eq. (72), based on the introduction of normal mode oscillators. We will explain the microscopic foundation of the EVC and demonstrate that all parameters appearing in this approach can be calculated, at least in principle. But it is the great advantage of these microscopically founded models that one can also use them to determine the parameters by fitting of experimental data. To meet the different notations used in literature we present formulas using mass-weighted normal mode oscillators and a notation where dimensionless normal mode coordinates are introduced. These coordinates can be directly related to oscillator annihilation and creation operators.

If the PES introduced in Eq. (64) have a well-defined minimum and if only small deviations of the nuclear coordinates from their equilibrium value are important one can carry out a normal mode analysis (see, e.g., [53]). We start with the most general case of the set $\{q_\xi\}$ of mass-weighted normal mode coordinates with mode index ξ and frequency ω_ξ valid for all types of PPC nuclear DOF. This model results in the following type of ground state PES:

$$U_0(R) = U_0^{(0)} + \sum_\xi \frac{\omega_\xi^2}{2} q_\xi^2\ . \tag{B.1}$$

The minimum value of the potential energy is denoted by $U_0(R^{(0)}) \equiv U_0^{(0)}$, where $R^{(0)} \equiv \{R_j^{(0)}\}$ is the equilibrium configuration of all types R_j of nuclear coordinates. Next, we introduce normal mode coordinates. In a first step, the PES $U_0(R)$ is expanded (up to the first nonvanishing order) with respect to the deviations $\Delta R_j = R_j - R_j^{(0)}$. In a second step, one diagonalizes the related Hamilton function which is bilinear with respect to the Cartesian nuclear coordinates and momenta. It results in a PES of type Eq. (B.1). The normal mode coordinates are related to the Cartesian coordinates via a linear transformation. For the present purpose we write

$$\Delta R_j = \sum_\xi M_j^{-1/2} A_{j\xi} q_\xi\ . \tag{B.2}$$

Since the nuclear degrees of freedom have been mapped onto a set of uncoupled harmonic oscillators one can also introduce an alternative notation of Eq. (B.1). Here creation and annihilation operators C_ξ^+, and C_ξ, respectively, of the normal mode quanta $\hbar\omega_\xi$ are used and the PES reads

$$U_0(R) = U_0^{(0)} + \sum_\xi \frac{\hbar\omega_\xi}{4} Q_\xi^2 \tag{B.3}$$

with the dimensionless normal mode coordinate

$$Q_\xi = C_\xi + C_\xi^+ \ . \tag{B.4}$$

Note that we have

$$q_\xi = \sqrt{\hbar/2\omega_\xi} Q_\xi \ . \tag{B.5}$$

The related PPC ground state Hamiltonian simply reads

$$H_{\mathrm{PPC}}^{(0)} = U_0^{(0)} + H_{\mathrm{vib}} \tag{B.6}$$

with the multi-mode harmonic oscillator Hamiltonian

$$H_{\mathrm{vib}} = \sum_\xi \hbar\omega_\xi C_\xi^+ C_\xi \ . \tag{B.7}$$

Note that the zero-point energy $\sum_\xi \hbar\omega_\xi/2$ has been included into the definition of $U_0^{(0)}$.

Clearly, for the present case of many Chl molecules embedded in a protein matrix this diagonalization represents a difficult task. In particular, the force constant matrix given by the second derivatives of the PES $U_0(R)$ is hardly available. Nevertheless, the relations enable one to introduce into the theory parameters which are based on correct microscopic expressions.

In a next step, we construct the normal mode representation of the excited state PES. General expressions are easily derived after writing Eq. (64) as

$$U(\{k\}_N; R) = U_0(R) + \Delta U(\{k\}_N; R) \tag{B.8}$$

with

$$\Delta U(\{k\}_N; R) = \sum_{m \in \{k\}_N} \varepsilon_m(eg; R) \ , \tag{B.9}$$

i.e. the sum of the isolated Chl excitation energies. Since the PES $U(\{k\}_N; R)$ ($\Delta U(\{k\}_N; R)$) correspond to excited electronic configurations of the PPC they do not posses a minimum at the nuclear configuration $R^{(0)}$. The expansion up to the first order with respect to the ΔR_j reads

$$\Delta U(\{k\}_N; R) \approx \Delta U(\{k\}_N; R^{(0)}) + \sum_j \left. \frac{\partial \Delta U(\{k\}_N; R)}{\partial R_j} \right|_{R=R^{(0)}} \Delta R_j \ . \tag{B.10}$$

Inserting the transformation Eq. (B.2) and renaming the terms finally gives

$$\Delta U(\{k\}_N; R) \approx \Delta U(\{k\}_N; R^{(0)}) - \sum_\xi \omega_\xi^2 q_\xi(\{k\}_N) q_\xi \ . \tag{B.11}$$

The constant coordinate $q_\xi(\{k\}_N)$ can be identified as

$$\begin{aligned} q_\xi(\{k\}_N) &= -\frac{1}{\omega_\xi^2} \sum_j \left. \frac{\partial \Delta U(\{k\}_N; R)}{\partial R_j} \right|_{R=R^{(0)}} M_j^{-1/2} A_{j\xi} \\ &\equiv -\frac{1}{\omega_\xi^2} \sum_{m \in \{k\}_N} \sum_j \left. \frac{\partial \varepsilon_m(eg; R)}{\partial R_j} \right|_{R=R^{(0)}} M_j^{-1/2} A_{j\xi} \ . \end{aligned} \tag{B.12}$$

For a singly excited PPC state it follows that (excitation at Chl*k*)

$$q_\xi(k) = -\frac{1}{\omega_\xi^2}\sum_j \left.\frac{\partial \varepsilon_k(eg;R)}{\partial R_j}\right|_{R=R^{(0)}} M_j^{-1/2} A_{j\xi} \ . \tag{B.13}$$

This set of quantities defines the shift of those PES relevant for vibrational motion in higher-excited PPC states. For example, because of Eq. (B.12) we have

$$q_\xi(k,l) = q_\xi(k) + q_\xi(l) \tag{B.14}$$

and

$$q_\xi(k,l,m) = q_\xi(k) + q_\xi(l) + q_\xi(m) \tag{B.15}$$

and so on.

Expression (B.11) enables one to introduce excited PPC-state PES as shifted parabola governing the motion of the normal mode vibrations

$$U(\{k\}_N;q) = U(\{k\}_N;R^{(0)}) - \sum_\xi \frac{\omega_\xi^2}{2} q_\xi^2(\{k\}_N) + \sum_\xi \frac{\omega_\xi^2}{2}(q_\xi - q_\xi(\{k\}_N))^2 \ . \tag{B.16}$$

Here, as a direct consequence of the restriction to the linear expansion, Eq. (B.10) it is assumed that the normal-mode frequencies do not change when the Chl are excited. The quantity $U(\{k\}_N;R^{(0)})$ can be considered as an effective Franck–Condon transition energy to the excited PPC-state $|\{k\}_N\rangle$ at fixed nuclear configuration. This energy is corrected by the second term on the right-hand side of Eq. (B.16) (polaron shift or reorganization energy). An alternative notation is obtained if the dimensionless normal mode coordinates, Eq. (B.4), are introduced:

$$U(\{k\}_N;Q) = U(\{k\}_N;R^{(0)}) + \sum_\xi \frac{\hbar\omega_\xi}{4} Q_\xi^2 + \sum_\xi \hbar\omega_\xi g_\xi(\{k\}_N) Q_\xi \ . \tag{B.17}$$

The dimensionless coupling constant reads

$$g_\xi(\{k\}_N) = -\sqrt{\frac{\omega_\xi}{2\hbar}}\, q_\xi(\{k\}_N) = \sum_{m\in\{k\}_N} g_\xi(m) \ , \tag{B.18}$$

where the second part of this equation directly follows from Eq. (B.12).

In addition to the formation of excited PPC-state PES (which are shifted with respect to the normal mode coordinate axis) we expect a modulation of the Chl–Chl coupling by the vibrational DOF. Using the general dipole–dipole coupling function, Eq. (17) we get the expansion

$$\begin{aligned} J_{mn}(R) &\approx J_{mn}(R^{(0)}) + \sum_j \left.\frac{\partial J_{mn}(R)}{\partial R_j}\right|_{R=R^{(0)}} \Delta R_j \\ &= J_{mn}(R^{(0)}) + \sum_\xi \tilde{\kappa}_{mn}(\xi) q_\xi \ . \end{aligned} \tag{B.19}$$

The new coupling constants are defined as

$$\tilde{\kappa}_{mn}(\xi) = \sum_j \left.\frac{\partial J_{mn}(R)}{\partial R_j}\right|_{R=R^{(0)}} M_j^{-1/2} A_{j\xi} \ . \tag{B.20}$$

Using dimensionless normal mode coordinates Q_ξ we may write

$$J_{mn}(R) \approx J_{mn}(R^{(0)}) + \sum_\xi \hbar\omega_\xi \tilde{g}_\xi(m,n) Q_\xi \tag{B.21}$$

with

$$\tilde{g}_\xi(m,n) = \frac{1}{\sqrt{2\hbar\omega_\xi^3}} \sum_j \left. \frac{\partial J_{mn}(R)}{\partial R_j} \right|_{R=R^{(0)}} M_j^{-1/2} A_{j\xi} \; . \tag{B.22}$$

The derived expressions are used to present the complete multi-excitation expansion of the PPC-Hamiltonian. Collecting the different contributions entering the Hamiltonian we write

$$H^{(N)}_{\mathrm{PPC}} = H^{(N)}_{\mathrm{el}}(R_0) + H^{(N)}_{\mathrm{ex\text{-}vib}} + H_{\mathrm{vib}} \; . \tag{B.23}$$

The first part is the electronic Hamiltonian for the Nth excited state, Eq. (34), but for the PPC electronic ground state nuclear configuration R_0. The second term on the right-hand side of Eq. (B.23) describes the coupling of vibrational modes to the various electronic PPC excitations

$$\begin{aligned} H^{(N)}_{\mathrm{ex\text{-}vib}} = \Bigg(& \sum_{\{k\}_N} \sum_\xi \hbar\omega_\xi g_\xi(\{k\}_N) Q_\xi \\ & + \sum_{m \notin \{k\}_N} \sum_{n \in \{k\}_N} \sum_\xi \hbar\omega_\xi \tilde{g}_\xi(m,n) Q_\xi B_m^+ B_n \Bigg) |\{k\}_N\rangle\langle\{k\}_N| \; . \end{aligned} \tag{B.24}$$

The multi-mode harmonic oscillator Hamiltonian H_{vib} (third part on the right-hand side of Eq. (B.23)) has been already introduced in Eq. (B.7).

As an example, we present $H^{(N)}_{\mathrm{PPC}}$ for the manifold of singly excited states and the doubly excited ones. The respective electronic Hamiltonians $H^{(N=1,2)}_{\mathrm{el}}(R_0)$ have already been presented in the Eqs. (37) and (38). The coupling of the single-excited state to the vibrational DOF can be written in the following compact form:

$$H^{(1)}_{\mathrm{ex\text{-}vib}} = \sum_{m,n} \sum_\xi \hbar\omega_\xi g_\xi(m,n) Q_\xi |m\rangle\langle n| \; , \tag{B.25}$$

where the coupling constant comprises diagonal and off-diagonal contributions, i.e.,

$$g_\xi(m,n) = \delta_{mn} g_\xi(m) + (1-\delta_{mn}) \tilde{g}_\xi(m,n) \; . \tag{B.26}$$

The two-excitation part reads

$$\begin{aligned} H^{(2)}_{\mathrm{ex\text{-}vib}} = & \sum_{m \neq n} \sum_\xi \hbar\omega_\xi g_\xi(m,n) Q_\xi |m,n\rangle\langle m,n| \\ & + \sum_{k \neq m, k \neq n} \sum_\xi \hbar\omega_\xi (\tilde{g}_\xi(k,m)|k,n\rangle\langle m,n| + \tilde{g}_\xi(k,n)|m,k\rangle\langle m,n|) Q_\xi \; . \end{aligned} \tag{B.27}$$

The notation presented so far has been introduced to derive a multi-exciton–vibrational coupling and to achieve a correct description of multi-exciton energy dissipation. If one bypasses the multi-excitation ordering scheme and the introduction of related PES one can use the notation of

Eq. (26) for H_{el} and simply obtain the complete PPC Hamiltonian as [9,57,73,74]

$$H_{\mathrm{PPC}} = E_0 + H_{\mathrm{vib}} + \sum_{m,n} \left(\delta_{mn} \varepsilon_m(eg; R_0) + (1 - \delta_{mn}) J_{mn} + \sum_{\xi} \hbar\omega_\xi g_\xi(m,n) Q_\xi \right) B_m^+ B_n \ . \tag{B.28}$$

Here, the EVC constant $g_\xi^{(1)}(m,n)$ introduced in Eq. (B.26) is valid for all excitations.

Appendix C. Nonlinear exciton–vibrational coupling

Nonlinear EVC contributions like the expression introduced in Eq. (81) can be systematically derived if one continues the Taylor expansion, Eq. (B.10), of $\Delta U(\{k\}_N; R)$, and Eq. (B.19) of $J_{mn}(R)$ to higher orders [20,83]. For instance, the respective second-order contributions can be written as

$$\frac{1}{2} \sum_{j,\bar{j}} \left. \frac{\partial^2 \Delta U(\{k\}_N; R)}{\partial R_j \partial R_{\bar{j}}} \right|_{R = R^{(0)}} \Delta R_j \Delta R_{\bar{j}} = \sum_{\xi,\bar{\xi}} \hbar \sqrt{\omega_\xi \omega_{\bar{\xi}}}\, g^{(2)}_{\xi,\bar{\xi}}(\{k\}_N) Q_\xi Q_{\bar{\xi}} \ . \tag{C.1}$$

For the expansion of the dipole–dipole coupling we have

$$\frac{1}{2} \sum_{j} \left. \frac{\partial^2 J_{mn}(R)}{\partial R_j \partial R_{\bar{j}}} \right|_{R = R^{(0)}} \Delta R_j \Delta R_{\bar{j}} = \sum_{\xi,\bar{\xi}} \hbar \sqrt{\omega_\xi \omega_{\bar{\xi}}}\, \tilde{g}^{(2)}_{\xi,\bar{\xi}}(m,n) Q_\xi Q_{\bar{\xi}} \ . \tag{C.2}$$

The new second-order coupling constants read

$$g^{(2)}_{\xi,\bar{\xi}}(\{k\}_N) = \sum_{j,\bar{j}} \frac{1}{4\omega_\xi \omega_{\bar{\xi}}} \left. \frac{\partial^2 \Delta U(\{k\}_N; R)}{\partial R_j \partial R_{\bar{j}}} \right|_{R = R^{(0)}} \frac{A_{j\xi} A_{\bar{j}\bar{\xi}}}{\sqrt{M_j M_{\bar{j}}}} \tag{C.3}$$

and

$$\tilde{g}^{(2)}_{\xi,\bar{\xi}}(m,n) = \sum_{j,\bar{j}} \frac{1}{4\omega_\xi \omega_{\bar{\xi}}} \left. \frac{\partial^2 J_{mn}(R)}{\partial R_j \partial R_{\bar{j}}} \right|_{R = R^{(0)}} \frac{A_{j\xi} A_{\bar{j}\bar{\xi}}}{\sqrt{M_j M_{\bar{j}}}} \ . \tag{C.4}$$

These expressions can be used to derive respective correlation functions, Eq. (98), governing multi-exciton energy dissipation via a quadratic EVC. To do this we have to change to the multi-exciton representation and, in similarity to Eq. (74), have to combine both coupling constants to the common quantity denoted here as $g_\xi^{(2)}(\alpha_N, \beta_N)$. The correlation function originating from the linear EVC has been introduced in Eq. (118). For the sake of completeness, we combine here the linear ($C^{(\mathrm{I})}$) and the quadratic contribution ($C^{(\mathrm{II})}$) of the coupling to the vibrational DOF, Eq. (81). Consequently, the correlation function splits up into two parts (a mixed part vanishes since it is of odd order in Q_ξ)

$$C(\alpha_N, \beta_N; \gamma_M, \delta_M; \omega) = C^{(\mathrm{I})}(\alpha_N, \beta_N; \gamma_M, \delta_M; \omega) + C^{(\mathrm{II})}(\alpha_N, \beta_N; \gamma_M, \delta_M; \omega) \ . \tag{C.5}$$

The first contribution can be expressed via a spectral density according to Eq. (118). The second type of correlation function is obtained as

$$\begin{aligned} C^{(\mathrm{II})}(\alpha_N, \beta_N; \gamma_M, \delta_M; \omega) &= \delta(\omega) c^{(\mathrm{II})}(\alpha_N, \beta_N; \gamma_M, \delta_M) \\ &+ \pi\omega^2 (1 + n(\omega/2))^2 (\mathscr{J}^{(\mathrm{II})}(\alpha_N, \beta_N; \gamma_M, \delta_M; \omega) + \mathscr{J}^{(\mathrm{II})}(\alpha_N, \beta_N; \gamma_M, \delta_M; -\omega)) \ . \end{aligned} \tag{C.6}$$

Note that it has been necessary here to use the so-called correlated part of $C^{(\mathrm{II})}$ (i.e. the full expression minus excpectation values of Q_ξ^2, cf. [53]). For the spectral density we have

$$\mathscr{J}^{(\mathrm{II})}(\alpha_N,\beta_N;\gamma_M,\delta_M;\omega)=\sum_\xi g_\xi^{(2)}(\alpha_N,\beta_N)g_\xi^{(2)}(\gamma_M,\delta_M)\delta(\omega-2\omega_\xi)\ . \tag{C.7}$$

Resulting from the quadratic coupling, $C^{(\mathrm{II})}$ describes electronic energy dissipation via the excitation (or de-excitation) of two quanta of normal mode vibrations. The part $c^{(\mathrm{II})}$ of the correlation function which is proportional to $\delta(\omega)$ is given by

$$c^{(\mathrm{II})}(\alpha_N,\beta_N;\gamma_M,\delta_M)=8\pi\int_0^\infty d\omega\ \omega^2 n(\omega/2)(1+n(\omega/2))\mathscr{J}^{(\mathrm{II})}(\alpha_N,\beta_N;\gamma_M,\delta_M;\omega)\ . \tag{C.8}$$

With the help of Eq. (116) this expression can be used to define a rate which is responsible for *pure dephasing* of excitonic coherences (see, e.g., Ref. [64]).

Appendix D. The anharmonic oscillator model of exciton dynamics

Having discussed the electronic PPC states based on a two-level model of the Chls in Section 3.3 and for a three-level model in Appendix A we present in the following a description which is valid for any number of intra-Chl electronic levels [80,138,151,234]. But in contrast to the Hamiltonian, Eq. (15), a different notation is used. It is based on the structure of the transition dipole operator which exclusively induces transitions between neighboring multi-excitation (multi-exciton) manifolds N and $N\pm1$. Assuming all dipole matrix elements $\boldsymbol{d}_{ab}^{(m)}$ to have the same orientation, one can write $\boldsymbol{d}_{ab}^{(m)}=\boldsymbol{e}_m d_{ab}^{(m)}$ with $\boldsymbol{e}^{(m)}$ being the respective unity vector. This enables one to introduce the dipole operator, Eq. (11), as a basic quantity (instead of $a=S_0,S_1,\dots$ we will write $a=0,1,\dots$)

$$\hat{\mu}_m=\boldsymbol{e}_m d_{10}^{(m)}(X_m+X_m^+)\ . \tag{D.1}$$

The new type of operators read

$$X_m^+=\sum_{a=0}^{L-1}\frac{d_{a+1,a}^{(m)}}{d_{10}^{(m)}}|\varphi_{ma+1}\rangle\langle\varphi_{ma}|\ , \tag{D.2}$$

where the number of relevant Chl levels has been denoted by L. With the X_m-operators the dipole–dipole coupling, Eq. (9), is easily rewritten to give (neglecting nonresonant contributions)

$$\hat{J}_{mn}=\frac{(\boldsymbol{e}_m\boldsymbol{e}_n)-3(\boldsymbol{e}_m\boldsymbol{n}_{mn})(\boldsymbol{e}_n\boldsymbol{n}_{mn})}{|\boldsymbol{z}_m-\boldsymbol{z}_n|^3}X_m^+X_n\equiv J_{mn}X_m^+X_n\ . \tag{D.3}$$

The single Chl contribution to the electronic PPC Hamiltonian, Eq. (15), reads

$$\sum_a \varepsilon_{ma}|\varphi_{ma}\rangle\langle\varphi_{ma}|=\sum_{a=0}^{L}\frac{1}{a!}\hbar\omega_{ma}X_m^{+a}X_m^a\ . \tag{D.4}$$

Here, the multiple application of X_m^+ and X_m builds up the projector $|\varphi_{ma}\rangle\langle\varphi_{ma}|$. The X-operators obey the following commutation relation:

$$[X_m,X_n^+]_-=\delta_{mn}\left(1-\sum_{a=0}^{L-1}q_{ma}X_m^{+a}X_m^a\right)\ . \tag{D.5}$$

The unknown quantities ω_{ma} and q_{ma} can be determined via recursion relations [151]. For the three-level scheme introduced in Appendix A one gets $\hbar\omega_{m1} = \varepsilon_{me}$, and $\hbar\omega_{m2} = 2(d_{eg}^{(m)}/d_{fe}^{(m)})^2\varepsilon_{mf} - 2\varepsilon_{me}$. The complete electronic PPC Hamiltonian, Eq. (15), in this collective oscillator representation reads

$$H_{\rm el} = \sum_m \sum_{a=0}^{L} \frac{1}{a!}\,\hbar\omega_{ma} X_m^{+a} X_m^{a} + \sum_{m,n} J_{mn} X_m^{+} X_n \,. \tag{D.6}$$

Within this notation all relevant excited Chl states are comprised in the single operator X_m^+, Eq. (D.2). This gives a compact notation in terms of anharmonic oscillators which represent the whole set of electronic levels. But the approach is less straightforward if a detailed description of relaxation processes via the multi-exciton levels becomes necessary. Therefore, the anharmonic oscillator representation of the Frenkel exciton Hamiltonian is well-suited for those cases where approximate description of EVC is valid.

To describe exciton dynamics within the present approach of an anharmonic oscillator representation it is advantageously to derive Heisenberg equations of motion for different types of products of the operators X_m^+ and X_n. If one takes the expectation value of these equations of motion respective equations for different types of observables are obtained. This anharmonic oscillator representation as well as the use of the excitation and deexcitation operators introduced in Eqs. (19) and (20), respectively have been extensively used in literature (see, e.g. [57,73,74,80, 138,151,234–236]). Since there is no direct translation of the expectation values of products of X_m^+ and X_n to observables like populations of the different exciton manifolds (cf. also [15]) we explain the equation of motion approach by using excitation and de-excitation operators, B_m^+ and B_n, Eqs. (19) and (20). The following considerations will be based on the Hamiltonian Eq. (B.28), and the equations of motion for the operators B_m read [57,73,74]

$$\begin{aligned} {\rm i}\hbar\frac{\partial}{\partial t}\langle B_m\rangle &= \sum_n h_{mn}\langle B_n\rangle + \sum_n \int_0^\infty {\rm d}t'\,\mathscr{K}_{mn}(t')\langle B_n\rangle(t-t') \\ &\quad + 2\sum_{n\neq n} J_{mn}\langle B_m^{\dagger} B_m B_n\rangle + \boldsymbol{d}_{eg}^{(m)}\boldsymbol{E}(t)[1-2\langle B_m^{+}B_m\rangle]\,, \end{aligned} \tag{D.7}$$

where the averaging is with respect to the vibrational DOF and we have introduced $h_{mn} = \delta_{mn}\varepsilon_m(eg) + (1-\delta_{mn})J_{mn}$. First, we notice that the dynamics of the operator B_m, which represents a S_0–S_1 coherence at site m, is coupled to the S_1 state population $B_m^+B_m$, as well as to a nonlocal operator $B_m^+B_mB_n$. In principle, this generates an infinite hierarchy of coupled equations for different operator products. In practice, it has been shown that upon restriction to a certain order in the external field this hierarchy can be truncated since the ordered operator product $(B^+)^p(B)^q$ is a least of order $p+q$ in the field [57].

The effect of the EVC is contained in the kernel $\mathscr{K}_{mn}(t)$ in Eq. (D.7). According to the form of the interaction Hamiltonian, Eq. (B.28), on the right-hand side of the equation for B_m a term $\sum_{n,\xi} g_\xi^{(1)}(m,n) B_n(C_\xi^+ + C_\xi)$ appears. $B_n(C_\xi^+ + C_\xi)$ can be considered as a new operator – a so-called vibrational-assisted operator – whose equations of motion have to be solved. Neglecting cross-terms which contain the interaction with the field and the EVC one finds the time-dependence of this operator from

$$[B_n(C_\xi^+ + C_\xi)](t) = -\frac{\mathrm{i}}{\hbar}\int_{-\infty}^{t} \mathrm{d}\bar{t} \sum_{kl}\sum_{\bar{\xi}} G_{mk}(t-\bar{t})g_{\bar{\xi}}^{(1)}(k,l) \times [\mathrm{e}^{\mathrm{i}\omega_{\bar{\xi}}(t-\bar{t})}[B_l C_\xi^+ C_{\bar{\xi}}](\bar{t}) + \mathrm{e}^{-\mathrm{i}\omega_{\bar{\xi}}(t-\bar{t})}[B_l C_\xi C_{\bar{\xi}}^+](\bar{t})] \,. \tag{D.8}$$

Here, $G_{mn}(t) = \Theta(t)[\exp\{-\mathrm{i}ht\}]_{mn}$ is the one-exciton Green's function. Apparently, this procedure gives a hierarchy of equations of motion for the vibrational-assisted operators as well which corresponds to a summation of the respective perturbations series. To lowest order in the EVC we can set (correlations between different vibrational modes does not appear)

$$\langle B_m C_\xi^+ C_{\bar{\xi}} \rangle \approx \delta_{\xi\bar{\xi}} n(\omega_\xi) \langle B_m \rangle \tag{D.9}$$

with $n(\omega_\xi)$ being the Bose–Einstein distribution for the vibrational modes. This allows us to identify the kernel in Eq. (D.7) with the second-order expression

$$\mathscr{K}_{mn}(t) = -\frac{\mathrm{i}}{\hbar}\sum_{kl}\sum_{\xi} g_\xi^{(1)}(mn)g_\xi^{(1)}(kl)\; G_{mk}(t)[\mathrm{e}^{\mathrm{i}\omega_\xi t}n(\omega_\xi) + \mathrm{e}^{-\mathrm{i}\omega_\xi t}(1+n(\omega_\xi))] \,. \tag{D.10}$$

Note that the respective contributions to the equation of motion for the exciton operator products in Eq. (D.7) will be different (see [235]). In Ref. [235] it has been shown that the equation of motion concept can be extended at least in principle to the nonperturbative regime using the method of generating functions.

In order to arrive at a Markovian approximation to the dissipative contribution to (D.7) we set $\langle B_n \rangle (t-\bar{t}) \approx \exp\{\mathrm{i}\varepsilon_m(eq)\bar{t}/\hbar\}\langle B_n \rangle(t)$. The remaining time-integral of $\mathscr{K}_{mn}(\bar{t})$ can be further simplified by introducing the frequency domain one-exciton Green's function

$$G_{mn}(\omega) = -\frac{\mathrm{i}}{\hbar}\int_0^\infty \mathrm{d}t\, \mathrm{e}^{\mathrm{i}\omega t}G_{mn}(t) = \sum_\alpha \frac{C_{\alpha_1}(m)C_{\alpha_1}^*(n)}{\hbar\omega - E_{\alpha_1} + \mathrm{i}\varepsilon} \,. \tag{D.11}$$

In the second part, we made use of the one-exciton eigenstates. Thus, the dissipative contribution to Eq. (D.7) becomes $\sum_n \mathscr{K}_{mn}(\omega_n)\langle B_n \rangle$ with

$$\mathscr{K}_{mn}(\omega) = \sum_{kl}\sum_{\xi} g_\xi^{(1)}(m,n)g_\xi^{(1)}(k,l)[G_{mk}(\omega+\omega_\xi)n(\omega_\xi) + G_{mk}(\omega-\omega_\xi)(1+n(\omega_\xi))] \,. \tag{D.12}$$

It should be noted that $\langle B_m \rangle = \langle |0\rangle\langle m| \rangle = \rho_{0m}$, i.e. the dissipative contribution to Eq. (D.7) is identical to the one which is obtained from the QME for $\rho_{0m}(t)$ (see, also [118]). The main advantage provided by the equation of motion approach can be appreciated, however, if one wants to keep track of the order in which the external field appears in the theory. Moreover, it allows to develop factorization schemes for expectation values of operator product as explained in [57]. Finally, this approach is well suited to develop a Green's function formulation of the nonlinear optical response as shown in [137] and Section 6.5.4.

At the end of this section we underline that the outlined treatment of the coupling to vibrational DOF is, of course, equivalent to that given by the QME in Section 5.1.1. For example, we can identify

$$\langle B_m \rangle = \mathrm{tr}_{\mathrm{el}}\{\hat{\rho}(t)B_m\} \,. \tag{D.13}$$

Here, $\hat{\rho}(t)$ is the density operator reduced to the electronic (excitonic) DOF and $\mathrm{tr}_{\mathrm{el}}\{\dots\}$ denotes the trace to the electronic DOF. The respective equation of motion is easily generated from the

QME, Eq. (101), by virtue of

$$\frac{\partial}{\partial t}\langle B_m\rangle = \mathrm{tr}_{\mathrm{el}}\left\{\left(\frac{\partial}{\partial t}\hat{\rho}(t)\right)B_m\right\} = \mathrm{tr}_{\mathrm{el}}\left\{\hat{\rho}(t)\frac{\mathrm{i}}{\hbar}(H_{\mathrm{S}}, B_m)_- - (\mathscr{R}[\hat{\rho}](t))B_m\right\} . \tag{D.14}$$

Inserting respective expressions for H_{S} and $\mathscr{R}$ Eq. (D.7) is reproduced.

Appendix E. Static disorder

An important factor influencing any optical measurement on PPC is static disorder [216]. All quantities entering the PPC Hamiltonian can be subject to fluctuations caused by structural and energetic disorder. For example, a change of the energy level structure from PPC to PPC leads to an additional broadening of the absorption which is measured on a sample containing a large number of PPC. Let us characterize such fluctuations by a set of parameters $y \equiv \{y_j\}$ which enter the Hamiltonian and describe a specific energetic and structural situation in the PPC. For the present type of systems we expect that the set y is closely related to the actual conformational substrate state the protein occupies (see [237] for the description of electron transfer reactions in proteins). To indicate the structure variation of the PPC the parameter set y will be additionally labeled by P counting all PPC contained in the sample volume V.

If we want to simulate a certain observable $A(t)$ measured in the experiment we have to note that every PPC will have its own $A_P(t)$ and the measured value follows as a ensemble (configuration) average (n_{PPC} is the volume density of the PPC in the probe)

$$\langle A(t)\rangle_{\mathrm{disorder}} = \frac{1}{V n_{\mathrm{PPC}}}\sum_{P\in V} A(t; y_P) . \tag{E.1}$$

If there exists a large number of different realizations one can change from the summation to the integration with respect to the set of parameters y:

$$\langle A(t)\rangle_{\mathrm{disorder}} = \int \mathrm{d}y\ \mathscr{F}(y)A(t; y) \tag{E.2}$$

with the distribution function

$$\mathscr{F}(y) = \frac{1}{V n_{\mathrm{PPC}}}\sum_{P\in V}\prod_j \delta(y_j - y_{Pj}) . \tag{E.3}$$

For specific applications $\mathscr{F}(y)$ is taken to be a continuous function of the parameters y_j.

Although the introduction of the distribution $\mathscr{F}(y)$ enables one to proceed with analytical calculations (see, for example [137,174,237]) in most of the cases the complex PPC structure asks for a numerical disorder averaging. This is usually done by generating via a Monte Carlo algorithm a parameter set $\{y_j\}$ and identifying this as belonging to a PPC from the probe volume. The disorder mean of $A(t)$ is calculated according to Eq. (E.1) by repeating the choice of $\{y_j\}$ as often as necessary (see, e.g. [63,64,84,138,236]).

The standard quantity one determines in this manner is the inhomogeneously broadened absorption coefficient [84,236]. Introducing the absorption cross section $\sigma = \sigma(\omega; y_P)$ of a single

PPC the measured absorption can be determined via

$$\alpha_{\text{inh}}(\omega) = \frac{1}{\Delta V} \sum_{P \in \Delta V} \sigma(\omega; y_P) \; . \tag{E.4}$$

Here, ΔV denotes the volume from which the PPC have been take to compute α_{inh}. To characterize the disorder influence on the single-exciton state one can introduce the exciton coherence length as discussed in Section 7.

Appendix F. Orientational average

In many types of optical experiments, PPC are isolated from the membrane and dissolved in a particular solvent thus showing random distribution of the different transition dipoles involved in the optical transitions of a, for example, pump–probe experiment. Consequently, the calculation of pump–probe spectra should include an averaging over the random orientations of the PPC in the sample. Taking the orientational average of the probe pulse signal leads to

$$\begin{aligned}\langle S^{(\text{pr})}(t)\rangle_{\text{orient}} = 2\omega_{\text{pr}} \sum_N \sum_{\alpha,\beta} \; &\text{Im}\; E^*_{\text{pr}}(t) \\ &\times \langle (\boldsymbol{e}_{\text{pr}} \boldsymbol{d}^*(N+1\alpha, N\beta)) \; \rho^{(n_{\text{pu}}=0, n_{\text{pr}}=1)}(N+1\alpha, N\beta; t)\rangle_{\text{orient}} \; .\end{aligned} \tag{F.1}$$

The orientational average on the r.h.s. cannot be further simplified, since the density matrix coefficients depend also on scalar products of the transition dipoles and the external pump and probe fields. One way to proceed would be a perturbational treatment of the interaction with the external field. In a scheme leading to a nonlinear susceptibility of third order (see Section 6.5.1) one has to average an expression containing four times the dipole operator.

A second possible approach is based on the derivation of equations of motion for the above given combined types of orientational averages including scalar products of the type $\boldsymbol{e}_{\text{pr}} \boldsymbol{d}^*(N+1\alpha, N\beta)$ and RDM expansion coefficients. In this manner a infinite hierarchy of orientational averages with increasing complexity is generated. A third way is given by a numerical calculation of the orientational average [84].

For this reason the vector $\boldsymbol{e}_{\text{PPC}}$ representing the spatial orientation of the PPC is introduced. As usual it may be characterized by the two angles θ and φ. For each particular orientation of $\boldsymbol{e}_{\text{PPC}}$ the time-integrated signal $S_{\text{tot}} = \int \mathrm{d}t \, S^{(\text{pr})}(t)$ is calculated. Then, the orientationally averaged signal is obtained as

$$\langle S_{\text{tot}} \rangle_{\text{orient}} = \frac{1}{4\pi} \int_0^{\pi} \mathrm{d}\theta \sin\theta \int_0^{2\pi} \mathrm{d}\varphi \; S_{\text{tot}}(\boldsymbol{e}_{\text{PPC}}(\theta, \varphi)) \; . \tag{F.2}$$

If one has a closed expression for $S_{\text{tot}}(\boldsymbol{e}_{\text{PPC}}(\theta,\varphi))$ the averaging can be carried out analytically (e.g. [165]). If $S_{\text{tot}}(\boldsymbol{e}_{\text{PPC}}(\theta,\varphi))$ is obtained via the numerical solution of a set of coupled differential equations the averaging has to be carried out numerically [196]. In Ref. [196] it could be demonstrated that convergence of the average can be obtained if a mesh with 12 points is used for the discretization of the unit sphere. Since the FMO complex with seven Chl forming the PPC has been investigated in [84] one deals with a system of seven coupled pigments, and the number of RDM equations that has to be solved are in the order of 10^3 at low pump-intensities. Even if these equations are solved 12 times to incorporate the orientational average, the computing time is about three times less than solving 3×10^4 equations at once. The latter computation would be necessary if the hierarchy of orientational averaged quantities are truncated in the simplest way. This difference of course increases rapidly at higher pump-pulse intensities where higher exciton manifolds have to be included in the simulation.

References

[1] R. Bassi, Photochem. Photobiol. 52 (1990) 1187.
[2] R.E. Fenna, B.W. Matthews, Nature 258 (1975) 573 ***.
[3] W. Kühlbrandt, D.N. Wang, Y. Fujiyoshi, Nature 367 (1994) 614 ***.
[4] G. McDermott, S.M. Prince, A.A. Freer, A.M. Hawthornthwaite-Lawless, M.Z. Papiz, R.J. Cogdell, N.W. Isaacs, Nature 374 (1995) 517 ***.
[5] A.S. Davydov, Theory of Molecular Excitons, Plenum, New York, 1962.
[6] M. Kasha, in: W.A. Glass, M.N. Varma (Eds.), Physical and Chemical Mechanisms in Molecular Radiation Biology, Plenum Press, New York, 1991, pp. 231.
[7] R.M. Pearlstein, in: E.I. Rashba, M.D. Sturge (Eds.), Excitons, North-Holland, Amsterdam, 1982, p. 735.
[8] V.M. Kenkre, P. Reineker, in: G. Höhler (Ed.), Springer Tracts Modern Physics, Vol. 94, Springer, Berlin, 1982 **.
[9] V.M. Agranovich, M.D. Galanin, in: V.M. Agranovich, A.A. Maradudin (Eds.), Modern Problems in Condensed Matter Sciences, North-Holland, Amsterdam, 1982.
[10] F.C. Spano, J. Knoester, in: T. Kobayashi (Ed.), J-Aggregates, World Scientific, Singapore, 1997, p. 117.
[11] H. Fidder, J. Knoester, D.A. Wiersma, J. Chem. Phys. 98 (1993) 6564.
[12] T. Renger, J. Voigt, V. May, O. Kühn, J. Phys. Chem. 100 (1996) 15 654.
[13] J. Knoester, F.C. Spano, Phys. Rev. Lett. 74 (1995) 2780.
[14] T. Renger, V. May, Phys. Rev. Lett. 78 (1997) 3406 *.
[15] T. Renger, V. May, V. Sundström, O. Kühn, J. Chin. Chem. Soc. 47 (2000).
[16] G.R. Fleming, R. van Grondelle, Phys. Today (February 1994) 48.
[17] R. van Grondelle, J.P. Dekker, T. Gillbro, V. Sundström, Biochim. Biophys. Acta 1187 (1994) 1 **.
[18] V. Sundström, R. van Grondelle, in: M.T. Madigan, C.E. Bauer (Eds.), Anoxygenic Purple Bacteria, Kluwer Academic, Dordrecht, 1995, p. 349.
[19] V. Sundström, T. Pullerits, R. van Grondelle, J. Phys. Chem. B 103 (1999) 2327.
[20] O. Kühn, T. Renger, V. May, J. Voigt, T. Pullerits, V. Sundström, Trends Photochem. Photobiol. 4 (1997) 213 **.
[21] R. Emerson, W. Arnold, J. Gen. Physiol. 16 (1932) 191.
[22] H. Gaffron, K. Wohl, Naturwissenschaften 24 (1936) 81.
[23] L.N.M. Duysens, Ph.D. Thesis, State University, Utrecht, 1953.
[24] K.R. Miller, Nature 300 (1982) 53.
[25] Y. Koyama, M. Kuki, P.O. Andersson, T. Gillbro, Photochem. Photobiol. 63 (1996) 243.
[26] H.A. Frank, R.J. Cogdell, Photochem. Photobiol. 63 (1996) 257.
[27] J.L. Herek, T. Polivka, T. Pullerits, G.J.S. Fowler, C.N. Hunter, V. Sundström, Biochemistry 37 (1998) 7057.
[28] L.K. Hanson, in: H. Scheer (Ed.), Molecular Orbital Theory of Monomer Pigments, CRC Press, Baton Rouge, 1991, p. 993.
[29] M. Gouterman, J. Mol. Spectrosc. 6 (1961) 138 ***.
[30] R.G. Alden, E. Johnson, V. Nagarajan, W.W. Parson, C.J. Law, R.J. Cogdell, J. Phys. Chem. B 101 (1997) 4667.
[31] K. Sauer, J.R.L. Smith, A.J. Schultz, J. Am. Chem. Soc. 88 (1966) 2681.
[32] J.H.C. Smith, A. Benitez, in: M. Tracy, K. Peach (Eds.), Modern Methods of Plant Analysis, Vol. 4, Springer, Berlin, 1955.
[33] J.F.G.M. Wintermans, A.D. Mots, Biochim. Biophys. Acta 109 (1965) 448.
[34] E. Bellacchio, K. Sauer, J. Phys. Chem. B 103 (1999).
[35] D. Leupold, S. Mory, R. König, P. Hoffmann, B. Hieke, Chem. Phys. Lett. 45 (1977) 567.
[36] J.F. Shepanski, R.W. Anderson, Chem. Phys. Lett. 78 (1981) 165.

[37] J.A.I. Oksanen, P. Martinsson, E. Åkesson, P.H. Hynninen, V. Sundström, J. Phys. Chem. A 102 (1998) 4328.
[38] H. Scheer (Ed.), Chlorophylls, CRC Press, London, 1991.
[39] M. Lutz, A.J. Hoff, L. Brehamet, Biochim. Biophys. Acta 679 (1982) 331.
[40] D.E. Tronrud, M.F. Schmid, B.W. Matthews, J. Mol. Biol. 188 (1986) 443.
[41] E.J.G. Peterman, T. Pullerits, R. van Grondelle, H. van Amerongen, J. Phys. Chem. B 1997 (4448).
[42] J. Pieper, M. Rätsep, R. Jankowiak, K.D. Irrgang, J. Voigt, G. Renger, G.J. Small, J. Phys. Chem. A 103 (1999) 2412.
[43] D.T. Leeson, O. Berg, D.A. Wiersma, J. Phys. Chem. 98 (1994) 3913.
[44] D.T. Leeson, D.A. Wiersma, K. Fritsch, J. Friedrich, J. Phys. Chem. B 101 (1997) 6331.
[45] R.M. Levy, D. Perahia, M. Karplus, Proc. Natl. Acad. Sci. USA 79 (1982) 1346.
[46] S. Hayward, N. Go, Ann. Rev. Phys. Chem. 46 (1995) 223.
[47] M.H. Vos, F. Rappaport, J.C. Lambry, J. Breton, J.L. Martin, Nature 363 (1993) 320.
[48] M.H. Vos, M.R. Jones, C.N. Hunter, J. Breton, J.L. Martin, Proc. Natl. Acad. Sci. USA 91 (1994) 12 701.
[49] M. Chachisvilis, H. Fidder, T. Pullerits, V. Sundström, J. Raman Spectrosc. 26 (1995) 513 ∗.
[50] R. Monshouwer, A. Baltuska, F. van Mourik, R. van Grondelle, J. Phys. Chem. A 102 (1998) 4360.
[51] T. Förster, Ann. Phys. (Leipzig) 6 (1948) 55 ∗∗.
[52] D.L. Dexter, J. Chem. Phys. 21 (1953) 836 ∗∗.
[53] V. May, O. Kühn, Charge and Energy Transfer Dynamics in Molecular Systems, Wiley-VCH, Berlin, 2000 ∗∗.
[54] G. Kehrberg, V. May, J. Voigt, Colloq. Plant Physiol. 10 (1986) 37.
[55] G. Juzeliunas, Z. Phys. D 8 (1988) 379.
[56] O. Dubrovsky, S. Mukamel, J. Chem. Phys. 95 (1991) 7828.
[57] S. Mukamel, Principles of Nonlinear Optical Spectroscopy, Oxford University Press, New York, 1995 ∗∗.
[58] J.C. Chang, J. Chem. Phys. 67 (77) 3901.
[59] R.G. Alden, E. Johnson, V. Nagarajan, W.W. Parson, C.J. Law, R.G. Cogdell, J. Phys. Chem. B 101 (1997) 4667.
[60] M.G. Cory, M.C. Zerner, X. Hu, K. Schulten, J. Phys. Chem. B 102 (1998) 7640.
[61] G.D. Scholes, I.R. Gould, R.J. Cogdell, G.R. Fleming, J. Phys. Chem. B 103 (1999) 2534.
[62] B.P. Krueger, G.D. Scholes, G.R. Fleming, J. Phys. Chem. B 102 (1998) 2284 ∗.
[63] O. Kühn, V. Sundström, J. Phys. Chem. B 101 (1997) 3432 ∗.
[64] O. Kühn, V. Sundström, J. Chem. Phys. 107 (1997) 4154 ∗.
[65] X. Hu, T. Ritz, A. Damjanovic, K. Schulten, J. Phys. Chem. B 101 (1997) 3854 ∗∗.
[66] X. Hu, D. Xu, K. Hamer, K. Schulten, J. Koepke, H. Michel, Protein Sci. 4 (1995) 1670.
[67] T. Pullerits, M. Chachisvilis, V. Sundström, J. Phys. Chem. 100 (1996) 10 787 ∗.
[68] J. Sturgis, B. Robert, Photosynth. Res. 50 (1996) 5.
[69] T.V. Dracheva, V.I. Novoderezhkin, A. Razjivin, FEBS Lett. 387 (1996) 81.
[70] K. Sauer, R.J. Cogdell, S.M. Prince, A.A. Freer, N.W. Isaacs, H. Scheer, Photochem. Photobiol. 64 (1996) 564.
[71] J. Linnanto, J.E.I. Korppi-Tommola, V.M. Helenius, J. Phys. Chem. B 103 (1999) 8739 ∗.
[72] G.D. Scholes, R.D. Harcourt, G.R. Fleming, J. Phys. Chem. B 101 (1997) 7302 ∗.
[73] O. Dubovsky, S. Mukamel, J. Chem. Phys. 95 (1991) 7828.
[74] F.C. Spano, Phys. Rev. Lett. 67 (1991) 3424.
[75] F.C. Spano, Phys. Rev. B 46 (1992) 13 017.
[76] T. Meier, V. Chernyak, S. Mukamel, J. Chem. Phys. 107 (1997) 8759 ∗.
[77] O. Kühn, T. Renger, V. May, J. Voigt, T. Pullerits, V. Sundström, Trends Photochem. Photobiol. 4 (1997) 213.
[78] O. Kühn, V. Rupasov, S. Mukamel, J. Chem. Phys. 104 (1996) 5821.
[79] T. Meier, Y. Zhao, V. Chernyak, S. Mukamel, J. Chem. Phys. 107 (1997) 3876 ∗.
[80] T. Meier, V. Chernyak, S. Mukamel, J. Phys. Chem. B 101 (1997) 7332.
[81] W.M. Zhang, T. Meier, V. Chernyak, S. Mukamel, J. Chem. Phys. 108 (1998) 7763.
[82] H. Sumi, J. Phys. Chem. B 103 (1999) 252.
[83] T. Renger, V. May, Photochem. Photobiol. 66 (1997) 618.
[84] T. Renger, V. May, J. Phys. Chem. A 102 (1998) 4381 ∗.
[85] T. Renger, V. May, Phys. Rev. Lett. 84 (2000) 5228.
[86] T. Renger, V. May, to be published.

[87] V. Daggett, M. Levitt, Ann. Rev. Biophys. Biomol. Struct. 22 (1993) 353.
[88] J.A. McCammon, Rep. Prog. Phys. 47 (1) (1984) 1 **.
[89] A. Warshel, W.W. Parson, Ann. Rev. Phys. Chem. 42 (1991) 279 **.
[90] M. Marchi, J.N. Gehlen, D. Chandler, M. Newton, J. Am. Chem. Soc. 115 (1993) 4178 *.
[91] H. Haken, P. Reineker, Z. Phys. 249 (1972) 253 *.
[92] H. Haken, G. Strobl, Z. Phys. 262 (1973).
[93] P. Reineker, C. Warns, T. Neidlinger, I. Barvik, Chem. Phys. 177 (1993) 715.
[94] E.G. Petrov, I.A. Goychuk, V. May, in: M. Schreiber (Ed.), Excitonic Processes in Condensed Matter, Dresden University Press, 1996, p. 327.
[95] L.D. Bakalis, M. Coca, J. Knoester, J. Chem. Phys. 110 (1999) 2208.
[96] C. Warns, I. Barvik, P. Reineker, T. Neidlinger, Chem. Phys. 194 (1995) 117.
[97] A.S. Davydov, Phys. Scripta 20 (1979) 387.
[98] Y. Zhao, T. Meier, W.M. Zhang, V. Chernyak, S. Mukamel, J. Phys. Chem. B 103 (1999) 3954.
[99] M. Chachisvilis, T. Pullerits, M.R. Jones, C.N. Hunter, V. Sundström, Chem. Phys. Lett. 224 (1994) 345 *.
[100] O. Kühn, T. Renger, V. May, Chem. Phys. 204 (1996) 99.
[101] T. Renger, V. May, J. Phys. Chem. B 101 (1997) 7232.
[102] R. Kubo, M. Toda, N. Hashitsume, Statistical Physics II: Nonequilibrium Statistical Mechanics, Springer, Berlin, 1985.
[103] K. Blum, Density Matrix Theory and Applications, Plenum Press, New York, 1996.
[104] M. Grover, R. Silbey, J. Chem. Phys. 54 (1971) 4843.
[105] R. Silbey, R.W. Munn, J. Chem. Phys. 72 (1980) 2763.
[106] V. Capek, I. Barvik, J. Phys. C 18 (1985) 6149.
[107] V. Capek, V. Szöcs, Phys. Stat. Sol. B 131 (1985) 667.
[108] E. Fick, G. Sauermann, The Quantum Statistics of Dynamic Processes, Springer, New York, 1990.
[109] T. Joo, Y. Jia, J.-Y. Yu, D.M. Jonas, G.R. Fleming, J. Phys. Chem. 100 (1996) 2399 *.
[110] A. Warshel, W.W. Parson, Annu. Rev. Phys. Chem. 42 (1991) 279.
[111] T. Polívka, T. Pullerits, J.L. Herek, V. Sundström, J. Phys. Chem. B 104 (2000) 1088.
[112] J.M. Jean, G.R. Fleming, J. Chem. Phys. 103 (1995) 2092.
[113] V. Chernyak, S. Mukamel, J. Chem. Phys. 105 (1996) 4565.
[114] M. Sparpaglione, S. Mukamel, J. Chem. Phys. 88 (1988) 3263 **.
[115] Y. Hu, S. Mukamel, J. Chem. Phys. 91 (1989) 6973.
[116] V. May, M. Schreiber, Chem. Phys. Lett. 181 (1991) 267.
[117] J.M. Jean, R.A. Friesner, G.R. Fleming, J. Chem. Phys. 96 (1992) 5827.
[118] V. May, O. Kühn, M. Schreiber, J. Phys. Chem. 97 (1993) 12 591.
[119] A. Suna, Phys. Rev. B 1 (1970) 1716.
[120] V.M. Kenkre, Phys. Rev. B 22 (1980) 2089.
[121] V.M. Kenkre, in: G. Höhler (Ed.), Springer Tracts Modern Physics, Vol. 94, Springer, Berlin, 1982, p. 1.
[122] V. Sundström, T. Gillbro, R.A. Gadonas, A. Piskarkas, J. Chem. Phys. 89 (1988) 2754.
[123] H. Stiel, S. Daehne, K. Teuchner, J. Lumin. 39 (1988) 351.
[124] S. Özcelik, D.L. Akins, J. Phys. Chem. B 101 (1997) 3021.
[125] V.A. Malyshev, H. Glaeske, K.H. Feller, Chem. Phys. Lett. 305 (1999) 117.
[126] G. Paillotin, C.E. Swenberg, J. Breton, N.E. Geacintov, Biophys. J. 25 (1979) 513.
[127] W.T.F.D. Hollander, J.G.C. Bakker, R. van Grondelle, Biochem. Biophys. Acta 725 (1983) 492.
[128] R. van Grondelle, Biochim. Biophys. Acta 811 (1985) 147 *.
[129] O.J.G. Somsen, F. van Mourik, R. van Grondelle, L. Valkunas, Biophys. J. 66 (1994) 1580.
[130] L. Valkunas, G. Trinkunas, V. Liuolia, R. van Grondelle, Biophys. J. 69 (1995) 1117.
[131] L. Valkunas, E. Ȧkesson, T. Pullerits, V. Sundström, Biophys. J. 70 (1996) 2373.
[132] L. Valkunas, V. Cervinskas, F. van Mourik, J. Phys. Chem. B 101 (1997) 7327.
[133] V. Gulbinas, L. Valkunas, D. Kuciauskas, E. Katilius, V. Lioulia, W. Zhou, R.E. Blankenship, J. Phys. Chem. B 100 (1996) 17 950.
[134] Y.-Z. Ma, R.J. Cogdell, T. Gillbro, J. Phys. Chem. B 101 (1997) 1087.

[135] T. Bittner, K.D. Irrgang, G. Renger, M.R. Wasielewski, J. Phys. Chem. 98 (1994) 11 821 *.
[136] N. Blombergen, Nonlinear optics, in: W.A. Benjamin (Ed.), Frontier in Physics, Vol. 21, Reading, MA, 1965.
[137] V. Chernyak, N. Wang, S. Mukamel, Phys. Rep. 263 (1995) 213 *.
[138] O. Kühn, S. Mukamel, J. Phys. Chem. B 101 (1997) 809 *.
[139] J.Y. Bigot, B. Höhnerlage, Phys. Stat. Sol. B 121 (1984) 649.
[140] V.M. Axt, K. Victor, A. Stahl, Phys. Rev. B 53 (1996) 7244.
[141] M. Chachisvilis, V. Sundström, J. Chem. Phys. 104 (1996) 5734.
[142] L. Seidner, G. Stock, W. Domcke, J. Chem. Phys. 103 (1995) 3998 *.
[143] R.P. Hemenger, J. Chem. Phys. 67 (1977) 262.
[144] R. Friesner, R. Silbey, J. Chem. Phys. 75 (1981) 5630.
[145] K. Mukai, S. Abe, H. Sumi, J. Phys. Chem. B 103 (1999) 6069.
[146] M. Cho, J.-Y. Yu, T. Joo, Y. Nagasawa, S.A. Passino, G.R. Fleming, J. Phys. Chem. 100 (1996) 11 944.
[147] J.-Y. Yu, Y. Nagasawa, R. van Grondelle, G.R. Fleming, Chem. Phys. Lett. 280 (1997) 404.
[148] M.L. Groot, J.-Y. Yu, R. Agarwal, J.R. Norris, G.R. Fleming, J. Phys. Chem. B 102 (1998) 5923.
[149] M. Yang, G.R. Fleming, J. Chem. Phys. 111 (1999) 27.
[150] R. Agarwal, B.P. Krueger, G.D. Scholes, M. Yang, J. Yom, L. Mets, G.R. Fleming, J. Phys. Chem. B 104 (2000) 2908.
[151] O. Kühn, V. Chernyak, S. Mukamel, J. Chem. Phys. 105 (1996) 8586.
[152] J. Koepke, X. Hu, C. Muenke, K. Schulten, H. Michel, Structure 4 (1996) 581.
[153] T. Pullerits, V. Sundström, Acc. Chem. Res. 29 (1996) 381 *.
[154] V. Sundström, T. Pullerits, R. van Grondelle, in: V. Sundström (Ed.), Femtochemistry and Femtobiology, World Scientific, Singapore, 1997.
[155] V. Novoderezhkin, R. Monshouwer, R. van Grondelle, Biophys. J. 77 (1999) 666.
[156] S. Hess, E. Åkesson, R.J. Cogdell, T. Pullerits, V. Sundström, Biophys. J. 69 (1995) 2211.
[157] R. Monshouwer, I.O.D. Zarate, F. van Mourik, R.V. Grondelle, Chem. Phys. Lett. 246 (1995) 341.
[158] H.M. Wu, S. Savikhin, N.R.S. Reddy, R. Jankowiak, R.J. Cogdell, W.S. Struve, G.J. Small, J. Phys. Chem. 100 (1996) 12 022 *.
[159] M.H.C. Koolhaas, R.N. Frese, G.J.S. Fowler, T.S. Bibby, S. Georgakopoulou, G. van der Zwan, C.N. Hunter, R. van Grondelle, Biochemistry 37 (1998) 4693.
[160] D. Leupold, H. Stiel, J. Ehlert, F. Nowak, K. Teuchner, B. Voigt, M. Bandilla, B. Ücker, H. Scheer, Chem. Phys. Lett. 301 (1999) 537.
[161] M. Chachisvilis, O. Kühn, T. Pullerits, V. Sundström, J. Phys. Chem. B 101 (1997) 7275 *.
[162] S. Hess, M. Chachisvilis, K. Timpmann, M.R. Jones, G.J.S. Fowler, C.N. Hunter, V. Sundström, Proc. Natl. Acad. Sci. USA 92 (1995) 12 333.
[163] T. Pullerits, S. Hess, J.L. Herek, V. Sundström, J. Phys. Chem. B 101 (1997) 10 560 *.
[164] S. Savikhin, W.S. Struve, Chem. Phys. 210 (1996) 91.
[165] V. Nagarajan, E.T. Johnson, J.C. Williams, W.W. Parson, J. Phys. Chem. B 103 (1999) 2297 *.
[166] S.I.E. Vulto, J.T.M. Kennis, A.M. Streltsov, J. Amesz, T.J. Aartsma, J. Phys. Chem. B 103 (1999) 878.
[167] A. Freiberg, J.A. Jackson, S. Lin, N.W. Woodbury, J. Phys. Chem. A 102 (1998) 4372.
[168] H.M. Wu, N.R.S. Reddy, G.J. Small, J. Phys. Chem. B 101 (1997) 651.
[169] M. Rätsep, H.M. Wu, J.M. Hayes, R.E. Blankenship, R.J. Cogdell, G.J. Small, J. Phys. Chem. B 102 (1998) 4035.
[170] S. Savikhin, W.S. Struve, Biophys. J. 67 (1994) 2002.
[171] R. Jimenez, S.N. Dikshit, S.E. Bradforth, G.R. Fleming, J. Phys. Chem. 100 (1996) 6825.
[172] J.A. Leegwater, J. Phys. Chem. 100 (1996) 14 403.
[173] R. Jimenez, F. van Mourik, J.Y. Yu, G.R. Fleming, J. Phys. Chem. B 101 (1997) 7350.
[174] L.D. Bakalis, J. Knoester, J. Phys. Chem. B 103 (1999) 6620.
[175] R. Monshouwer, M. Abrahamsson, F. van Mourik, R. van Grondelle, J. Phys. Chem. B 101 (1997) 7241.
[176] J. Ray, N. Makri, J. Phys. Chem. A 103 (1999) 9417.
[177] V. Novoderezhkin, R. Monshouwer, R. van Grondelle, J. Phys. Chem. B 103 (1999) 10 540.
[178] D. Leupold, H. Stiel, K. Teuchner, F. Nowak, W. Sandner, B. Ücker, H. Scheer, Phys. Rev. Lett. 77 (1996) 4675 *.
[179] H. Stiel, D. Leupold, K. Teuchner, F. Nowak, H. Scheer, R.J. Cogdell, Chem. Phys. Lett. 276 (1997) 62.

[180] R. Kumble, R.M. Hochstrasser, J. Chem. Phys. 109 (1998) 855.

[181] Y.B. Gaididei, A.A. Serikov, Teor. Mat. Fiz. 27 (1976) 242.

[182] M. Lutz, G. van Brakel, in: J.M. Olson, J.G. Ormerod, J. Amesz, E. Stackebrandt, H.G. Trüper (Eds.), Green Photosynthetic Bacteria, Plenum Press, New York, 1988.

[183] Y.F. Li, W. Zhou, R.E. Blankenship, J.P. Allen, J. Mol. Biol. 271 (1997) 456.

[184] S.G. Johnson, G.J. Small, J. Phys. Chem. 95 (1991) 471.

[185] A. Freiberg, S. Lin, K. Timpmann, R.E. Blankenship, J. Phys. Chem. B 101 (1997) 7211 **.

[186] S. Savikhin, D.R. Buck, W.S. Struve, J. Phys. Chem. B 102 (1998) 5556.

[187] R.M. Pearlstein, R.P. Hemenger, Proc. Natl. Acad. Sci. USA 75 (1978) 4920.

[188] R. M. Pearlstein, Photosynth. Res. 31 (1992) 213.

[189] X. Lu, R.M. Pearlstein, Photochem. Photobiol. 57 (1993) 86.

[190] K.D. Philipson, K. Sauer, Biochemistry 11 (1972) 1880.

[191] J.M. Olson, B. Ke, K.H. Thompson, Biochim. Biophys. Acta 430 (1976) 524.

[192] D. Gülen, J. Phys. Chem. 100 (1996) 17 683.

[193] R.J.W. Louwe, J. Vrieze, A.J. Hoff, T.J. Aartsma, J. Phys. Chem. B 101 (1997) 11 280.

[194] S. Dracheva, J.C. Williams, R.E. Blankenship, in: N. Murata (Ed.), Research in Photosynthesis, Vol. 1, Kluwer, Dordrecht, 1992, p. 53.

[195] S.I.E. Vulto, M.A. de Baat, R.J. Louwe, H.P. Permentier, T. Neef, M. Miller, H. van Amerongen, T.J. Aartsma, J. Phys. Chem. B 102 (1998) 9577.

[196] T. Renger, Ph.D. Thesis, Humboldt University, Berlin, 1998, www.ub.hu-berlin.de/cdrom/disspub.html.

[197] S.I.E. Vulto, M.A. de Baat, S. Neerken, F.R. Nowak, H. van Amerongen, J. Amesz, T.J. Aartsma, J. Phys. Chem. B 103 (1999) 8153 *.

[198] S. Savikhin, W.S. Struve, Biochemistry 33 (1994) 11 200.

[199] S.I.E. Vulto, A.M. Streltsov, T.J. Aartsma, J. Phys. Chem. B 101 (1997) 4845.

[200] S. Savikhin, D.R. Buck, W.S. Struve, Biophys. J. 73 (1997) 2090.

[201] S. Savikhin, D.R. Buck, W.S. Struve, Chem. Phys. 223 (1997) 303.

[202] A. Matro, J.A. Cina, J. Phys. Chem. 99 (1995) 2568.

[203] R.S. Knox, D. Gülen, Photochem. Photobiol. 57 (1993) 40.

[204] K. Wynne, R.M. Hochstrasser, Chem. Phys. 171 (1993) 179.

[205] S.I.E. Vulto, S. Neerken, R.J.W. Louwe, M.A. Baat, J. Amesz, T.J. Aartsma, J. Phys. Chem. B 102 (1998) 10 630.

[206] G. Renger, Topics in Photosynthesis, Vol. 11, Elsevier, Amsterdam, 1992, p. 45.

[207] C.C. Gradinaru, S. Özdemir, D. Gülen, I.H.M. van Stokkum, R. van Grondelle, H. van Amerongen, Biophys. J. 75 (1998) 3064.

[208] H. Rogl, W. Kühlbrandt, Biochemistry 38 (1999) 16 214.

[209] P.W. Hemelrijk, S.L.S. Kwa, R. van Grondelle, J.P. Dekker, Biochim. Biophys. Acta 1098 (1992) 159.

[210] N.R.S. Reddy, H. van Amerongen, S.L.S. Kwa, R. van Grondelle, G.J. Small, J. Phys. Chem. 98 (1994) 4729.

[211] J. Pieper, K.D. Irrgang, M. Rätsep, R. Jankowiak, T. Shrötter, J. Voigt, G.J. Small, G. Renger, J. Phys. Chem. A 103 (1999) 2422.

[212] D. Gülen, R. van Grondelle, H. van Amerongen, in: P. Mathis (Ed.), Photosynthesis: From light to biosphere, Vol. 1, Kluwer Academic Publishers, Dordrecht, 1995, p. 335.

[213] T. Renger, Master's Thesis, Humboldt University, Berlin, 1995.

[214] J. Voigt, T. Renger, R. Schödel, J. Pieper, H. Redlin, Phys. Stat. Sol. B 194 (1996) 333.

[215] J. Voigt, K. Maciy, T. Schrötter, Photosynthetica 30 (1995) 576.

[216] E.W. Knapp, Chem. Phys. 85 (1984) 73.

[217] D. Gülen, R. van Grondelle, H. van Amerongen, J. Phys. Chem. 101 (1997) 7256.

[218] C.C. Gradinaru, S. Özdemir, D. Gülen, I.H.M. van Stokkum, R. van Grondelle, H. van Amerongen, Biophys. J. 75 (1998) 3064.

[219] T. Gillbro, V. Sundström, A. Sandström, M. Spangfort, B. Andersson, FEBS Lett. 193 (1985) 267.

[220] D.D. Eads, E.W. Castner, R.S. Alberte, L. Mets, G.R. Fleming, J. Phys. Chem. 93 (1989) 8271.

[221] M. Du, X. Xie, L. Mets, G.R. Fleming, J. Phys. Chem. 98 (1994) 4736 *.

[222] L.O. Pålsson, M.D. Spangfort, V. Gulbinas, T. Gillbro, FEBS Lett. 339 (1994) 134.

[223] T. Bittner, G.P. Wiederrecht, K.D. Irrgang, G. Renger, M.R. Wasielewski, Chem. Phys. 194 (1995) 311.
[224] H.M. Visser, F.J. Kleima, I.H.M. van Stokkum, R. van Grondelle, H. van Amerongen, Chem. Phys. 210 (1996) 297.
[225] J.P. Conelly, M.G. Müller, M. Hucke, G. Gatzen, C.W. Mullineaux, A.V. Ruban, P. Horton, A.R. Holzwarth, J. Phys. Chem. B 101 (1997) 1902.
[226] F.J. Kleima, C.C. Gradinaru, F. Calkoan, I.H.M. van Stokkum, R. van Grondelle, H. can Amerongen, Biochem. 36 (1997) 15 262.
[227] S. Savikhin, H. van Amerongen, S.L.S. Kwa, R. van Grondelle, W.S. Struve, Biophys. J. 66 (1994) 1597.
[228] Y. Tanimura, S. Mukamel, J. Chem. Phys. 103 (1985) 1983.
[229] R.E. Riter, M.D. Edington, W.F. Beck, J. Phys. Chem. B 101 (1997) 2366.
[230] V. Chernyak, S. Mukamel, Phys. Rev. Lett. 74 (1995) 4895.
[231] O. Kühn, S. Mukamel, J. Phys. Chem. B 101 (1997) 809.
[232] M.R. Shortreed, S.F. Swallen, Z.-Y. Shi, W. Tan, Z. Xu, C. Devadoss, J.S. Moore, R. Kopelman, J. Phys. Chem. B 101 (1997) 6318.
[233] C. Tietz, O. Chekhlov, A. Dräbenstedt, J. Schuster, J. Wrachtrup, J. Phys. Chem. B 103 (1999) 6328.
[234] W.M. Zhang, V. Chernyak, S. Mukamel, J. Chem. Phys. 110 (1999) 5011.
[235] V.M. Axt, S. Mukamel, in: J. Maloney (Ed.), IMA Volumes in Mathematics and its Applications, Vol. 101, Springer, Berlin, 1997, p. 1.
[236] H. Fidder, J. Knoester, D.A. Wiersma, J. Chem. Phys. 95 (1991) 7881.
[237] V.S. Pande, J. Onuchic, Phys. Rev. Lett. 78 (1997) 146.
[238] J. Voigt, T. Schrötter, Z. Phys. Chem. Part 2 211 (1999) 181.
[239] S. Nussberger, Biochemistry 33 (1994) 14 775.